Light hadron phenomenology with overlap fermions and an improved gauge action.

David Galletly

Doctor of Philosophy

The University of Edinburgh

2005

For my Parents

Abstract

In this thesis we study light hadron phenomenology using lattice QCD. In particular we measure hadron masses, meson decay constants, and nucleon structure functions.

We perform the lattice simulation using overlap fermions. This formulation preserves chiral symmetry at finite lattice spacing and so is well suited to simulations close to the chiral limit. It is however very computationally expensive and so we are forced to work in the quenched approximation.

After a review of the relevant continuum phenomenology and lattice gauge theory, we detail the necessary lattice technology required to extract physical results from the simulations. We then present the results. We use an improved gauge action and investigate how this affects the locality and condition number of the overlap Dirac operator. We present measurements of masses for some low lying hadron states, and in order to make contact with continuum physics, we calculate some lattice renormalization constants.

After providing measurements of vector and pseudoscalar meson decay constants, we present results on nucleon structure functions. While these structure functions cannot be measured directly on the lattice, we can relate measurable QCD matrix elements to moments of structure functions through the operator product expansion. Here we provide results for several low moments of both polarized and unpolarized nucleon structure functions. We conclude with a discussion of the results.

Acknowledgements

I would firstly like to thank my supervisors, Roger Horsley and Brian Pendleton. I consider myself very fortunate to have received such excellent supervision. Both have been generous with their time and knowledge, and have followed my progress closely. I have learned a great deal from both of them and am very grateful. I would also like to thank Bálint Joó, who spent a great deal of time on code development for this project, and was always willing to help when I ran into problems. I would also like to thank Tony Kennedy, who first prompted me to study chiral fermions and helped get me started on this project. I would like to thank Gerrit Schierholz for time on the HLRN system in Berlin, and Ron Horgan for use of the computing facilities at the CCHPCF. In addition, I would like to thank all of the members of the PPT group for making my stay here an enjoyable one. Without exception, I have found the members of this group to be friendly and helpful, and have found it a very supportive environment to study in.

Most importantly, I wish to thank my family. My parents and brothers have always provided me with unwavering love, support and encouragement, without which I could never have got this far. I love you all.

Contents

Chapter 1

Introduction

The aim of particle physics is to describe the fundamental constituents of matter and how they interact with each other. The present level of understanding can be condensed into what is known as the "Standard model" of particle interactions. It combines the strong and electro-weak interactions into one consistent quantum field theory described by a Lagrangian possessing an $SU(3)_c \times SU(2)_L \times U(1)_Y$ gauge symmetry. It describes fundamental spin $\frac{1}{2}$ quarks and leptons whose interactions are mediated by spin 1 gauge bosons. It also includes a spin 0 Higgs particle, however this has not yet been detected experimentally.

The strong interactions are described by the part of the standard model known as Quantum Chromodynamics or QCD. In QCD the fundamental particles are quarks which carry a "colour charge" and interact through gluon exchange, much like in QED where charged particles interact through photon exchange. However in contrast to QED where the photons carry no charge, gluons also carry a colour charge and interact with each other. This

self interaction means that the strong interactions must be described by a non-Abelian gauge theory and hence possess the property of asymptotic freedom [1, 2]. This ensures that at high enough energies the gauge coupling will be small and perturbation theory will be valid. In this high energy regime, QCD has successfully managed to predict particle phenomena. However in the low energy regime the gauge coupling becomes large and perturbation theory is no longer valid. Hence in order to study low energy phenomena such as the hadron mass spectrum and hadronic matrix elements we must resort to non-perturbative methods.

The next section contains a brief survey of the QCD phenomenology relevant to this thesis. It describes the form of the QCD Lagrangian and gives an indication of how approximate flavour symmetries can give a qualitative description of the hadron mass spectrum within the quark model. However the main topic of this thesis will be the structure of the nucleon. Experimentally measured cross sections from deep inelastic scattering (DIS) and hard scattering nucleon processes can be parameterized in terms of unknown structure functions. The various structure functions and the processes which are measured in order to extract them experimentally are discussed. A physical interpretation of these functions can be derived using the parton model. Finally, it is shown how moments of these structure functions can be related to QCD matrix elements via the operator product expansion.

Nucleon matrix elements must be determined non-perturbatively. Lattice QCD provides a technique for measuring QCD matrix elements as well as other low energy phenomena. Chapter 3 provides a brief introduction to the main features of Lattice QCD. Previous calculations of nucleon structure

functions have been carried out using either Wilson fermions (or variants thereof) or staggered fermions. Both of these explicitly break the chiral symmetry of the fermion action in continuum QCD. Recent theoretical improvements, combined with increased computing power, have now made it possible to run simulations which retain chiral symmetry. Using the Ginsparg-Wilson formalism [3] and the overlap solution of Neuberger [4], we can now simulate fermions which possess an on-shell chiral symmetry at fixed lattice spacing. These fermions should be more "continuum-like" and provide more accurate determinations of physical quantities in the chiral regime. However while simulations of chiral fermions are now possible, they are still hugely costly in terms of computer time (even compared to other lattice simulations) and so fully dynamical simulations have only very recently become possible. As such, all of the simulations in this thesis are carried out in the quenched approximation. This approximation is described as well as the action chosen to simulate the background gauge fields.

Hadron masses and decay constants are measured from two point correlation functions while matrix elements are measured from ratios of three point and two point correlation functions. Chapters 4 and 5 cover the lattice technology required to construct these correlation functions and how they can used to extract physical information. The various operator insertions and how they relate to desired structure functions are explained, as are the various lattice techniques for improving the overlap of these operators with physical states, and for minimizing lattice artifacts.

The matrix elements calculated from the lattice simulations are bare quantities and must be renormalized in order to be compared with exper-

iment. Renormalization and the process of renormalizing lattice matrix elements is discussed in Chapter 6. While some of the renormalization constants can be determined non-perturbatively from conserved currents and lattice identities, others have to be obtained by alternative methods such as tadpole-improved lattice perturbation theory.

Chapter 7 is an investigation of the locality and condition number of the overlap-Dirac operator and its dependence on the auxiliary mass parameter and the underlying gauge fields. The effect of eigenvalue projection on the condition number is also considered.

In Chapter 8 the results of the simulations are presented and discussed. Results are given for low lying hadron masses, meson decay constants, non-perturbative renormalization constants, and nucleon matrix elements related to low moments of nucleon structure functions.

Finally, Chapter 9 is a summary of the results and conclusions of the thesis. Outstanding issues are discussed along with suggestions for extensions and future work.

Chapter 2

QCD Phenomenology

Quantum Chromodynamics or QCD is the theory which describes the strong interactions. It contains two fundamental types of particles : quarks and gluons. The quarks are spin $\frac{1}{2}$ fermions which interact via a "colour" charge. These interactions are mediated by gluons which are spin 1 bosons. However the gluons also carry a colour charge and hence interact with each other. As such QCD is a non-Abelian gauge theory. The quarks come in three colours, while the gluons come in 8 different colours. The action is invariant under $SU(3)_c$ gauge transformations. The QCD Lagrangian is given by

$$\mathcal{L}_{QCD} = -\frac{1}{4}F_a^{\mu\nu}F_{\mu\nu}^a + i\sum_f \bar{\psi}_i^f \gamma^\mu (D_\mu)_{ij}\psi_j^f - \sum_f m_f \bar{\psi}_k^f \psi_k^f, \qquad (2.1)$$

where f is a quark flavour index (u, d, s, c, b, t), μ and ν are Lorentz indices, while a and i, j, k are colour indices. D_μ is a gauge covariant derivative

$$(D_\mu)_{ij} = \partial_\mu \delta_{ij} + ig\sum_a \frac{\lambda_{ij}^a}{2} A_\mu^a. \qquad (2.2)$$

The λ^a are the eight Gell-mann matrices which provide a representation of the $su(3)$ Lie algebra, and g is the gauge coupling. The field strength tensor

$F_{\mu\nu}$ can be defined in the usual way as the commutator of the covariant derivative

$$[D_\mu, D_\nu] = gF_{\mu\nu}, \tag{2.3}$$

but due to the commutation rules of the λ^as this includes a term which is bilinear in the gauge fields. Its components are then given by

$$F^a_{\mu\nu} = \partial_\mu A^a_\nu - \partial_\nu A^a_\mu - g f_{abc} A^b_\mu A^c_\nu. \tag{2.4}$$

The f_{abc} are the structure constants of su(3) defined by

$$\left[\frac{\lambda^a}{2}, \frac{\lambda^b}{2}\right] = i f_{abc} \frac{\lambda^c}{2}. \tag{2.5}$$

The Lagrangian (2.1) determines the dynamics of quarks and gluons, however neither of these two types of particles have been observed on their own. They are always hidden in bound states as hadrons. Asymptotic freedom and the subsequent increasing value of the effective gauge coupling with distance give some indication as to why quarks and gluons form bound states, however this is not sufficient to fully explain the absence of free quarks and gluons . Even in high energy processes where the coupling is small, no free quarks or gluons are observed. Their presence is inferred from hadron jets. In fact no state bound or otherwise has been observed which has colour. The only physically observed states are bound states which are colour singlets.

This colour confinement places restrictions on the quark content of observed hadrons. If the only hadrons that can be formed are those which are colour singlets, then their wavefunctions must transform trivially under $SU_c(3)$. Singlet wavefunctions can be built out of tensor products of quark operators q_i (where q_i is contracted notation for ψ^q_i), antiquark operators $\bar{q}^i$,

and the $SU(3)$ isotropic tensors ϵ_{ijk}, ϵ^{ijk}, and δ^i_j. The only simple[1] singlet operators are then

$$\delta^i_j q_i \bar{q}^j \qquad \epsilon^{ijk} q_i q_j q_k \qquad \epsilon_{ijk} \bar{q}^i \bar{q}^j \bar{q}^k. \tag{2.6}$$

So we have that colour confinement leads directly to mesons, baryons, and anti-baryons.

2.1 Mass spectrum

The quark model of hadrons discussed above can be used to give a qualitative explanation of the hadron spectrum. While there are 6 flavours of quarks we can split them into the light quarks (u, d, s) which have masses in the MeV range and the much heavier quarks (c, b, t) with masses in the GeV range. As the light quark masses and mass splittings are much less than typical hadronic scales such as Λ_{QCD} and the nucleon mass, we can then make the approximation that the light quarks are roughly mass degenerate and so the hadron mass spectrum should be invariant under exchange of light quark flavours. This symmetry of the mass spectrum implies that the light hadrons should fit into degenerate multiplets corresponding to irreducible representations of the symmetry group $SU(3)_f$. The light quarks q have 3 flavour degrees of freedom and so must transform in the fundamental representation of $SU(3)$ which we denote by 3. The antiquarks $\bar{q}$ will then transform in the $\bar{3}$ representation. This then determines the transformation properties of the bound states of quarks and antiquarks as they will simply transform as

[1]For reviews of searches for more exotic states see [5, 6].

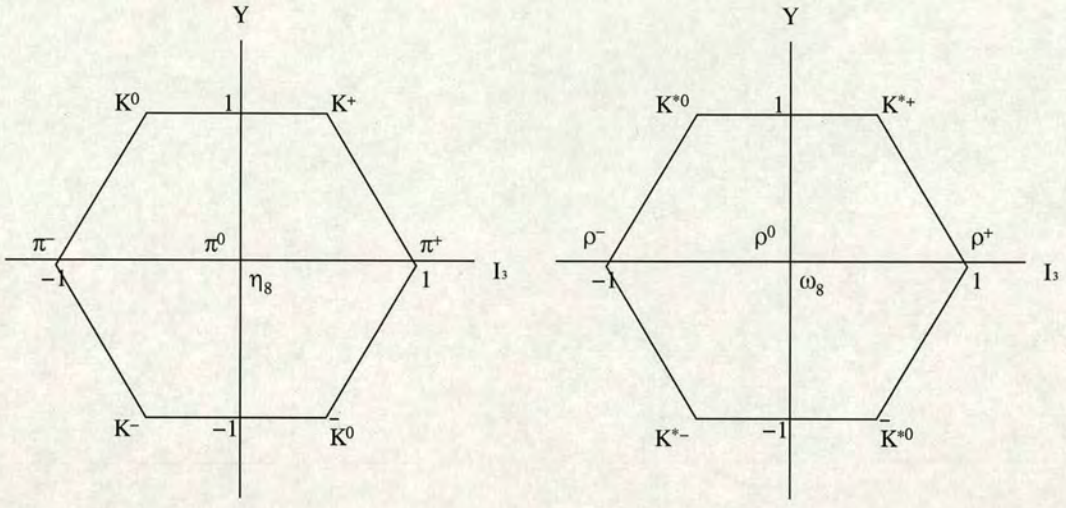

Figure 2.1: Weight diagrams for the 0^{-+} and 1^{--} meson octets.

tensor products of their constituents. We can decompose these tensor products into direct sums of their irreducible representations which will tell us the dimension of the corresponding degenerate multiplets. Since all of the members of a particular multiplet only differ by their quark content, their spatial and spin quantum numbers are identical and so each multiplet can be labeled by the J^{PC} of its members. For $q\bar{q}$ states we have a decomposition

$$3 \otimes \bar{3} \rightarrow 8 \oplus 1, \tag{2.7}$$

while for qqq (and $\bar{q}\bar{q}\bar{q}$ [2]) we have

$$3 \otimes 3 \otimes 3 \rightarrow 10 \oplus 8 \oplus 8 \oplus 1. \tag{2.8}$$

Hence we expect mesons to form singlets and octets, while baryons form singlets, octets, and decuplets. The weight diagrams for the 0^{-+} pseudoscalar

[2] for $\bar{q}\bar{q}\bar{q}$ simply exchange all representations for their "barred" counterparts.

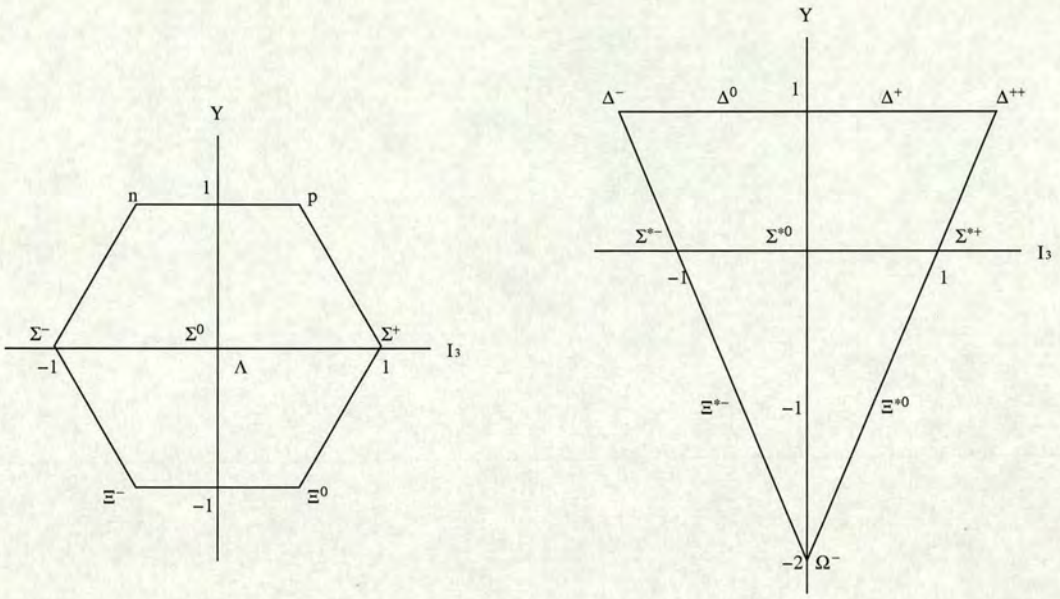

Figure 2.2: Weight diagrams for the baryon $\frac{1}{2}^+$ octet and $\frac{3}{2}^+$ decuplet.

meson octet and the 1^{--} vector meson octet are shown in Figure 2.1. Each state is labeled by its hypercharge Y and third component of isospin ${I_3}^3$. In the pseudoscalar octet, the quark model state η_8 has similar quantum numbers to the singlet state η_1 and hence the two can mix to form the physical states η and η'. Similarly for the vector meson octet, the equivalent states ω_8 and ω_1 will mix to give the physical states ω and ϕ. The groundstate ($L = 0$) baryon multiplets are given in Figure 2.2. Note there is no ground state baryon singlet since for $L = 0$, the wavefunction is symmetric under exchange of spatial indices. As it is both a colour and flavour singlet it must be totally antisymmetric under colour and flavour. Hence in order to satisfy the Pauli Exclusion principle the wavefunction must be totally antisymmetric

[3]For definitions of these quantum numbers see for example [7].

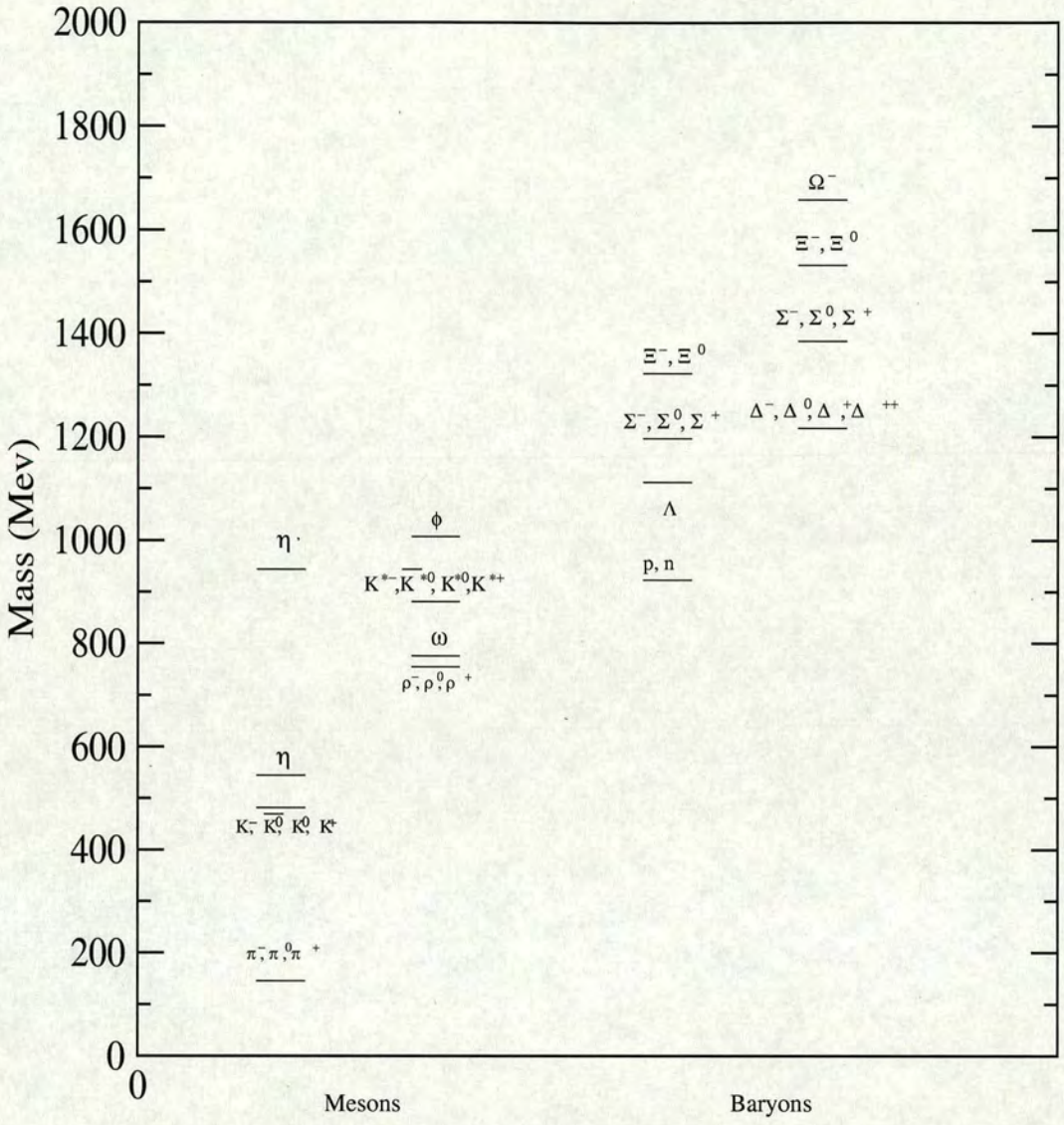

Figure 2.3: Observed hadron mass spectrum for the 0^{-+}, 1^{--} meson octets, and the $\frac{1}{2}^+$, $\frac{3}{2}^+$ baryon octet and decuplet.

under spin exchange which is not possible for a three quark state.

These multiplets explain the observed light hadron spectrum quite well,

although there are mass splittings due mainly to the fact that the mass degeneracy of the quarks is only approximate. The observed hadron masses and their quark model interpretations are shown in Figure 2.3.

2.2 Decay constants

In semi-leptonic meson decays, the scattering matrix can be factorized into a leptonic piece and a hadronic matrix element. For example, the primary decay channel for the π^+ is $\pi^+ \to \mu^+\nu_\mu$ via W^+ exchange (see Figure 2.4) which has the scattering matrix[4]

$$\mathcal{M} = (-ig_w)^2 V_{ud}\bar{u}_\nu(\vec{k}_1)\gamma_\lambda(1-\gamma_5)v_\mu(\vec{k}_2)\frac{i}{m_w^2}\langle 0|J^\lambda(0)|\pi^+(\vec{p})\rangle, \tag{2.9}$$

where g_w is the Electro-weak coupling constant, V_{ud} is the CKM mixing element and J^λ is the weak current given by

$$J^\lambda = \bar{d}\gamma^\lambda(1-\gamma_5)u. \tag{2.10}$$

We can split this current into its vector and axial parts and then use Lorentz invariance to parameterize the corresponding matrix elements. Since the pion is a pseudoscalar the matrix element of the vector part will transform like an axial vector and hence must vanish. The matrix element of the axial part will transform like a vector and hence be proportional to the pion momenta p^λ (since it is the only 4-vector associated with this matrix element). Hence the QCD matrix element in the scattering matrix can be parameterized as

$$\langle 0|\bar{u}\gamma^\lambda\gamma_5 d|\pi^+(\vec{p})\rangle = -i\sqrt{2}f_\pi p^\lambda, \tag{2.11}$$

[4]We have assumed here that the momentum transfer is small and so the W propagator is simply $\frac{ig^{\mu\nu}}{m_W^2}$.

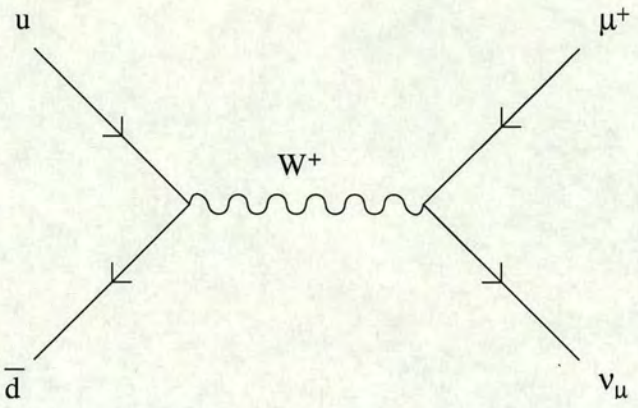

Figure 2.4: $\pi^+ \to \mu^+ \nu_\mu$ via annihilation into W^+.

where f_π is the pion decay constant.

For vector mesons like the ρ^+ we have an extra polarization vector $\epsilon^\mu(\vec{p}, \lambda)$ associated with the state. Here only the vector part of the weak current survives and we can again parameterize

$$\langle 0|\bar{u}\gamma^\mu d|\rho^+(\vec{p}), \lambda\rangle = -i\epsilon^\mu(\vec{p}, \lambda)\frac{m_\rho^2}{f_\rho}, \tag{2.12}$$

where the decay constant f_ρ is historically taken to be dimensionless.

2.3 Structure functions

2.3.1 Elastic scattering

In lepton-hadron scattering we can again factorize the leptonic and hadronic parts of the scattering matrix. In elastic scattering processes the hadronic matrix element can be parameterized in terms of generally unknown form factors which depend only on the momentum transfer. In purely electromag-

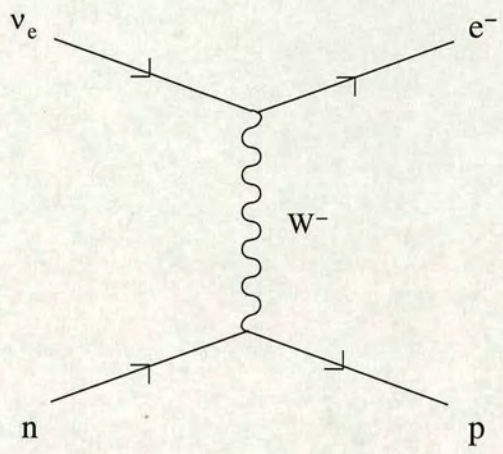

Figure 2.5: neutron-neutrino scattering via W^- exchange.

netic scattering such as electron-proton scattering via photon exchange we have a scattering matrix

$$\mathcal{M} = (-ie)^2 \bar{u}_e(\vec{k}')\gamma_\mu u_\nu(\vec{k}) \frac{-i}{q^2} \langle p(\vec{p}')|J_e^\mu(\vec{q})|p(\vec{p})\rangle, \tag{2.13}$$

where J_e^μ is the electromagnetic current[5]

$$J_e^\mu = \frac{2}{3}\bar{u}\gamma^\mu u - \frac{1}{3}\bar{d}\gamma^\mu d + \ldots. \tag{2.14}$$

The hadronic part has then a general decomposition

$$\langle p(\vec{p}')|J_e^\mu(\vec{q})|p(\vec{p})\rangle = \bar{u}_p(\vec{p}')[\gamma^\mu f_1(q^2) + i\sigma^{\mu\nu}\frac{q_\nu}{2m_p} f_2(q^2)]u_p(\vec{p}), \tag{2.15}$$

where m_p is the proton mass, $q = p' - p$ is the momentum transfer, and the $f_i(q^2)$ are the vector current form factors.

[5]There are obviously similar terms for the other quark flavours however we generally assume their overlap with the nucleon to be small.

In weak processes the situation is more complicated as the current has both vector and axial parts. In neutron-neutrino scattering (Figure 2.5) for instance the hadronic part of the scattering matrix is given by

$$\langle p(\vec{p}')|J_\mu(\vec{q})|n(\vec{p})\rangle, \tag{2.16}$$

where J^μ is the weak current given by $J^\mu = \bar{u}\gamma^\mu(1-\gamma_5)d$. We can param-

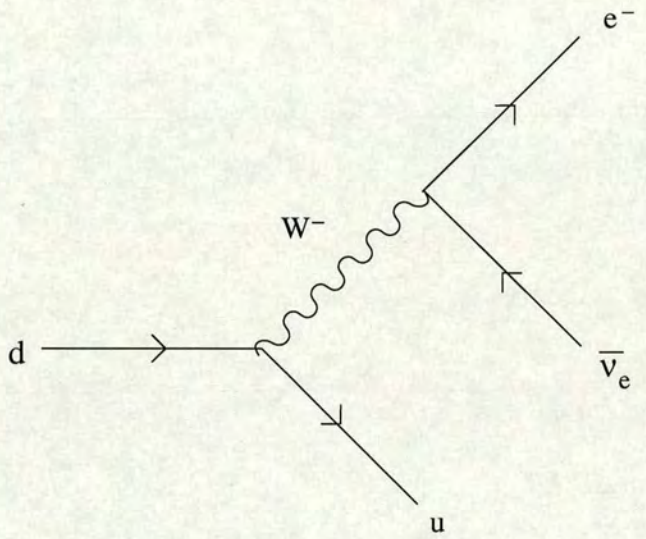

Figure 2.6: β decay.

eterize both the vector and axial parts as before[6]

$$\begin{aligned}\langle p(\vec{p}')|V_\mu^+|n(\vec{p})\rangle &\equiv \langle p(\vec{p}')|\bar{u}\gamma_\mu d|n(\vec{p})\rangle \\ &= \bar{u}_p(\vec{p}')[\gamma_\mu f_1(q^2) + i\sigma_{\mu\nu}\frac{q^\nu}{m_p+m_n}f_2(q^2)]u_n(\vec{p})\end{aligned} \tag{2.17}$$

[6]Note there is one less vector form factor than the axial case. This is due to the conservation of the vector current [8] which places an extra constraint on the form of the vector matrix element and reduces the number of degrees of freedom. This constraint is not present in the axial current which is not conserved for non-zero quark mass.

$$\langle p(\vec{p}')|A_\mu^+|n(\vec{p})\rangle \equiv \langle p(\vec{p}')|\bar{u}\gamma_\mu\gamma_5 d|n(\vec{p})\rangle$$
$$= \bar{u}_p(\vec{p}')[\gamma_\mu\gamma_5 g_1(q^2) + i\sigma_{\mu\nu}\frac{q^\nu}{m_p+m_n}\gamma_5 g_2(q^2) + \frac{q_\mu}{m_p+m_n}\gamma_5 g_3(q^2)]u_n(\vec{p}). \tag{2.18}$$

One situation of interest is when the momentum transfer q is very small. This would correspond to the case of β decay (Figure 2.6). Then the matrix elements take on the simple form

$$\langle p(\vec{p})|V_\mu^+|n(\vec{p})\rangle = \bar{u}_p(\vec{p})\gamma_\mu f_1(0)u_n(\vec{p}) \tag{2.19}$$

$$\langle p(\vec{p})|A_\mu^+|n(\vec{p})\rangle = \bar{u}_p(\vec{p})\gamma_\mu\gamma_5 g_1(0)u_n(\vec{p}). \tag{2.20}$$

The quantities $f_1(0)$ and $g_1(0)$ are known as the vector and axial charges of the nucleon. In this form though they are defined in terms of matrix elements between two different nucleon states. However the difference in the two nucleon masses is small and so we can use isospin symmetry in order to express this matrix element in a "diagonal" form. We first define vector and axial isospin currents[7] by

$$V_\mu^i = \frac{1}{2}\bar{\psi}\gamma_\mu\sigma^i\psi$$
$$A_\mu^i = \frac{1}{2}\bar{\psi}\gamma_\mu\gamma_5\sigma^i\psi. \tag{2.21}$$

Since the vector current is a conserved current we have an associated charge operator which we can define as

$$Q_V^i = \int d^3x V_0^i(\vec{x},t). \tag{2.22}$$

[7]The σ^i for $i = 1,2,3$ are the generators of $SU(2)_f$.

We can then form combinations $V_\mu^\pm = V_\mu^1 \pm iV_\mu^2$ and $A_\mu^\pm = A_\mu^1 \pm iA_\mu^2$ and corresponding raising and lowering operators Q_V^+ and Q_V^- which satisfy

$$\begin{aligned} Q_V^+|n\rangle &= |p\rangle, & Q_V^+|p\rangle &= 0 \\ Q_V^-|p\rangle &= |n\rangle, & Q_V^-|n\rangle &= 0. \end{aligned} \tag{2.23}$$

Using the commutation relations

$$[Q_V^+, V_\mu^3] = -V_\mu^+, \qquad [Q_V^+, A_\mu^3] = -A_\mu^+, \tag{2.24}$$

we have

$$\begin{aligned} \langle p|V_\mu^+|n\rangle &= -\langle p|[Q_V^+, V_\mu^3]|n\rangle \\ &= \langle p|V_\mu^3|p\rangle - \langle n|V_\mu^3|n\rangle \\ &= 2\langle p|V_\mu^3|p\rangle, \end{aligned} \tag{2.25}$$

and similarly $\langle p|A_\mu^+|n\rangle = 2\langle p|A_\mu^3|p\rangle$.

As $V_\mu^3 = \frac{1}{2}(\bar{u}\gamma_\mu u - \bar{d}\gamma_\mu d)$ we have from conservation of charge that $f_1(0) = 1$, while the axial charge $g_A = g_1(0)$ is given by

$$\langle p|A_\mu^+|n\rangle = \frac{1}{2}\langle p|\bar{u}\gamma_\mu\gamma_5 u - \bar{d}\gamma_\mu\gamma_5 d|p\rangle = g_A\bar{u}_p\gamma_\mu\gamma_5 u_n. \tag{2.26}$$

2.3.2 Inelastic scattering

In deep inelastic scattering processes the momentum transfer is large enough to destroy the incoming nucleon. In electron-proton scattering through photon exchange the scattering matrix is given by

$$\mathcal{M} = (-ie)^2\bar{u}_e(\vec{k}')\gamma_\mu u_e(\vec{k})\frac{i}{q^2}\langle X(\vec{p}')|J_e^\mu(\vec{q})|p(\vec{p})\rangle, \tag{2.27}$$

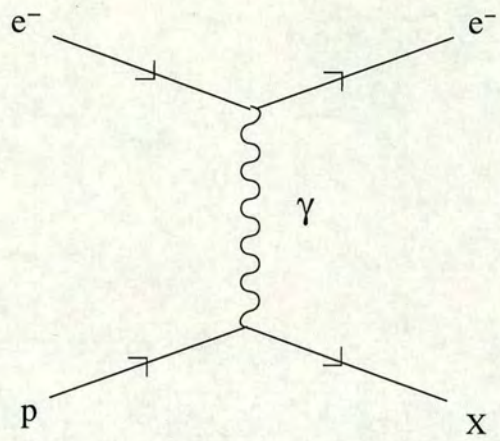

Figure 2.7: Electron-Proton Deep inelastic scattering.

where now the final hadronic state X is unknown (Figure 2.7). The relevant kinematic variables are given in Table 2.1. In order to calculate the cross section this matrix must be squared and summed over all possible final states. The cross section again factorizes into a leptonic piece and a hadronic piece. In the laboratory frame (rest frame of the nucleon) this is given by [9]

$$\frac{d^2\sigma}{d\Omega dE'} = \frac{\alpha^2}{q^4}\frac{E'}{m_N E} L_{\mu\nu} W^{\mu\nu}. \tag{2.28}$$

The leptonic tensor $L_{\mu\nu}$ involves only point particles and can be evaluated directly. Using the identity

$$\sum_{spin} u(k)\bar{u}(k) = \not{k}\,, \tag{2.29}$$

where the lepton mass is taken to be small and hence ignored. For unpolarized leptons we have

$$L_{\mu\nu}(k,k') = \sum_{spin} \bar{u}(k')\gamma_\mu u(k)\bar{u}(k)\gamma_\nu u(k')$$

E	Energy of the incoming electron
E'	Energy of the outgoing electron
$q = k' - k$	momentum of the virtual photon
$Q^2 = -q^2$	as $q^2 < 0$
$\nu = \frac{p.q}{m_N}$	The energy loss of the electron
$x = \frac{Q^2}{2m_N\nu}$	Bjorken scaling variable
$\omega = 1/x$	

Table 2.1: DIS kinematic variables.

$$\begin{aligned} &= \frac{1}{2}Tr[\not{k}'\gamma_\mu \not{k}\gamma_\nu] \\ &= 2(k'_\mu k_\nu + k'_\nu k_\mu - g_{\mu\nu}k'.k). \end{aligned} \tag{2.30}$$

When the incoming lepton beams are polarized there is an additional term and $L_{\mu\nu}$ is given by

$$L_{\mu\nu}(k, s_l, k') = 2(k'_\mu k_\nu + k'_\nu k_\mu - g_{\mu\nu}k'.k + i\epsilon_{\mu\nu\alpha\beta}q^\alpha s_l^\beta), \tag{2.31}$$

where s_l^β is the incoming lepton polarization vector given by

$$2s_l^\beta = \bar{u}(k, s)\gamma^\beta\gamma_5 u(k, s). \tag{2.32}$$

$W^{\mu\nu}$ is defined in terms of the hadronic matrix element. First taking the Fourier transform of this matrix element

$$\langle X(\vec{p}')|J_e^\mu(\vec{q})|p(\vec{p})\rangle = \int d^4x e^{-iq.x}\langle X(\vec{p}')|J_e^\mu(x)|p(\vec{p})\rangle, \tag{2.33}$$

we can then define[8] the hadronic tensor $W^{\mu\nu}$

$$W^{\mu\nu}(p, q) = \frac{1}{4\pi}\sum_X \langle p(\vec{p})|J_e^\mu(-\vec{q})|X(\vec{p}')\rangle\langle X(\vec{p}')|J_e^\nu(\vec{q})|p(\vec{p})\rangle$$

[8]The first step is from a Fourier transform and then translation invariance. The second step uses the completeness relation $\sum |X\rangle\langle X| = 1$. The final step is true since the second

$$
\begin{aligned}
&= \frac{1}{4\pi}\sum_X \int d^4x e^{-iq.x}\langle p(\vec{p})|J_e^\mu(x)|X(\vec{p}')\rangle\langle X(\vec{p}')|J_e^\nu(0)|p(\vec{p})\rangle \\
&= \frac{1}{4\pi}\int d^4x e^{-iq.x}\langle p(\vec{p})|J_e^\mu(x)J_e^\nu(0)|p(\vec{p})\rangle \\
&= \frac{1}{4\pi}\int d^4x e^{-iq.x}\langle p(\vec{p})|[J_e^\mu(x), J_e^\nu(0)]|p(\vec{p})\rangle. \qquad (2.34)
\end{aligned}
$$

A Lorentz decomposition of $W^{\mu\nu}$ in terms of known momenta and unknown structure functions can be carried out. A general decomposition for DIS processes [9] is given by

$$
\begin{aligned}
W^{\mu\nu}(p,q) &= (-g^{\mu\nu}+\frac{q^\mu q^\nu}{q^2})F_1(x,Q^2)+\frac{1}{p.q}(p^\mu-\frac{p.q}{q^2}q^\mu)(p^\nu-\frac{p.q}{q^2}q^\nu)F_2(x,Q^2) \\
&\quad -\frac{i}{p.q}\epsilon^{\mu\nu\alpha\beta}q_\alpha s_\beta g_1(x,Q^2)-\frac{i}{p.q}\epsilon^{\mu\nu\alpha\beta}q_\alpha(s_\beta-\frac{s.q}{p.q}p_\beta)g_2(x,Q^2). \qquad (2.35)
\end{aligned}
$$

The F_i's and g_i's are respectively the unpolarized and polarized structure functions associated with deep inelastic scattering, while the polarization vector s_β here is obviously referring to the polarization of the nucleon. It should be noted that in both the leptonic and hadronic tensors, terms involving polarization vectors are antisymmetric under exchange of indices μ, ν while the unpolarized terms are symmetric. This implies that when calculating the cross section, the terms in $l_{\mu\nu}W^{\mu\nu}$ either contain both polarization vectors or neither. Hence the unpolarized structure functions F_i are probed by unpolarized leptons and nucleons, while the polarized structure functions require both polarized leptons and nucleons.

term in the commutator vanishes. Note that $\sum_X$ is shorthand for not only the sum over final states but also integrating over final momenta.

2.3.3 Drell-Yan processes

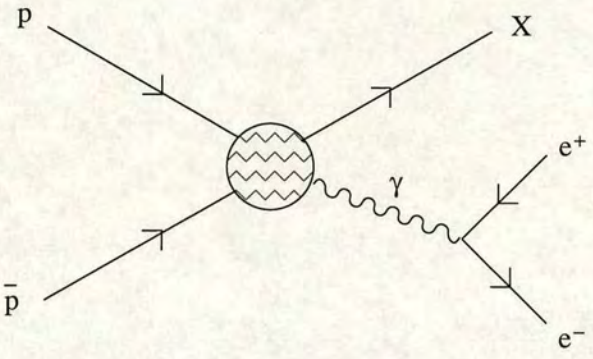

Figure 2.8: Drell-Yan scattering of $p\bar{p}$.

Another method for probing nucleon structure is by looking at Drell-Yan processes. Here two incoming hadron beams are collided together, e.g. $p\bar{p}$. A quark and antiquark then annihilate to form a virtual photon which will then decay into a e^+, e^- lepton pair, with the rest of the hadronic material scattering off in the form of unknown hadron jets (Figure 2.8). The hadronic tensor $W_{\mu\nu}$ is then calculated in exactly the same way as for DIS, with the only difference being that we now have two initial state hadrons instead of one. It is given by

$$W_{\mu\nu}(p_1, p_2; k) = \frac{1}{4\pi} \int d^4x e^{-ik.x} \langle p(\vec{p_1})\bar{p}(\vec{p_2})|[J_e^\mu(x), J_e^\nu(0)]|p(\vec{p_1})\bar{p}(\vec{p_2})\rangle, \tag{2.36}$$

where $k = k_1 + k_2$ is the photon 4-momentum. What distinguishes Drell-Yan processes from those in DIS is that we have two initial states. This means that the two incoming particles can have different helicities, and therefore in the massless limit, different chiralities. Hence there is a contribution to the

hadronic tensor which is chirally odd i.e. the incoming particles flip chiralities. This contribution was obviously not present in DIS as we only have one spin vector associated with the DIS tensor. This leads to a further structure function h_1 known as the transversity. This can be measured experimentally by looking at the asymmetry A of the polarized cross-section

$$A = \frac{\sigma^{\perp\perp} - \sigma^{\perp\top}}{\sigma^{\perp\perp} + \sigma^{\perp\top}}, \tag{2.37}$$

where $\sigma^{\perp\perp}$ ($\sigma^{\perp\top}$) is the cross-section for two transversely polarized (with respect to beam direction) proton beams where the spins are parallel (anti-parallel) to each other.

2.4 The parton model

While we can decompose the matrix elements given in the previous sections into structure functions, the physical interpretation of these functions is still unclear. The parton model provides a simple picture of scattering process and so can help in this regard. In this model the hadrons are considered to be made up of a collection of free, on-shell partons (i.e. quarks and gluons). In high energy interactions this a reasonable approximation due to asymptotic freedom. The scattering cross-section is then simply the (incoherent) sum of the cross-sections for free quarks and gluons.

These free quarks and gluons can be described by parton distribution functions. For a hadron carrying momentum p, then the parton will be carrying a momentum fraction ξp with $0 < \xi < 1$ (the parton is assumed to be moving co-linearly with respect to the hadron). A quark parton distribution function $q_\sigma(\xi)$ is then the probability of finding a quark carrying momentum

ξp. The subscript σ is the spin polarization along the incoming beam direction, with $\sigma = \uparrow (\downarrow)$ indicating spin polarization parallel (anti-parallel) with respect to the hadron. There are similar definitions for antiquark ($\bar{q}_\sigma(\xi)$) and gluon ($G(\xi)$) distribution functions. It should be noted that a parton with momentum ξp has an invariant mass $\xi^2 M_N^2$, which obviously depends on ξ. However we again assume we are working in a high energy scattering regime and so can neglect target mass corrections.

To lowest order, only the quarks will scatter with the virtual photon as gluons have no charge. While the hadrons are spatially extended, the partons are point-like and so the contribution to $W_{\mu\nu}$ from a single quark takes roughly the same form as the lepton tensor $l_{\mu\nu}$ (2.30) with the replacement $k \to \xi p$. The only difference being we must as before sum over the final particle phase space. Hence for a single quark we have

$$W_{\mu\nu} = \frac{1}{4\pi} e_q^2 \int \frac{d^3p'}{(2\pi)^3 2E_{p'}} \frac{1}{\xi} (2\pi)^4 \delta^4(\xi p + q - p') \times 2(\xi p'_\mu p_\nu + \xi p'_\nu p_\mu - g_{\mu\nu} \xi p'.p + i\epsilon_{\mu\nu\alpha\beta} q^\alpha s^\beta). \quad (2.38)$$

The e_q factor is the charge of the quark in question, and there is an extra factor $\frac{1}{\xi}$ which is a reflection of the fact that as the proton states are normalized to $2p^0$ the parton states are normalized to $2p^0\xi$.

If the electron-quark scattering is assumed to be elastic i.e. $(\xi p + q)^2 \approx 0$, then the phase space integral can be done by noting that

$$\begin{aligned} \int \frac{d^3p'}{(2\pi)^3 2E_{p'}} \delta^4(\xi p + q - p') &= \int \frac{d^4p'}{(2\pi)^4} (2\pi) \delta^4(\xi p + q - p') \delta((\xi p + q - p')^2) \\ &= \int \frac{d^4p'}{(2\pi)^4} (2\pi) \delta^4(\xi p + q - p') \delta(2\xi p.q + q^2) \\ &= \int \frac{d^4p'}{(2\pi)^4} \frac{(2\pi)}{2p.q} \delta^4(\xi p + q - p') \delta(\xi + \frac{q^2}{2p.q}). \end{aligned}$$

(2.39)

The integral (2.38) can then be performed by making the replacement $p' = \xi p + q$, and since the leptonic current J_e^μ is conserved we have the relation $q^\mu l_{\mu\nu} = 0$, meaning we can drop the terms in $W_{\mu\nu}$ containing q^μ and q^ν. Finally as the partons are massless the spin vector s_β can be expressed as $s_\beta = h_q \xi p_\beta$ where $h_q = 1, -1$ is the parton's helicity. Putting all this together we get the final result

$$W_{\mu\nu} = \frac{e_q^2}{2\xi p.q}[2\xi^2 p_\mu p_\nu - g_{\mu\nu}\xi p.q + ih\xi\epsilon_{\mu\nu\alpha\beta}q^\alpha p^\beta]\delta(\xi - x). \tag{2.40}$$

The result for antiquarks is identical. Comparing this result with equation (2.35) we see that for each quark we have a contribution to the structure functions given by

$$\begin{aligned} F_1^q(x) &= \frac{e_q^2}{2}\delta(\xi - x) \\ F_2^q(x) &= e_q^2\xi\delta(\xi - x) \\ g_1^q(x) &= \frac{e_q^2}{2}h_q h_N \delta(\xi - x) \\ g_2^q(x) &= 0. \end{aligned} \tag{2.41}$$

The full structure functions are then calculated by integrating over all possible momentum fractions ξ, weighted by the corresponding distribution function $q_\sigma(\xi)$. This gives

$$\begin{aligned} F_1(x) &= \sum_q \frac{e_q^2}{2}(q_\uparrow(x) + q_\downarrow(x) + \bar{q}_\uparrow(x) + \bar{q}_\downarrow(x)) \\ F_2(x) &= \sum_q e_q^2 x(q_\uparrow(x) + q_\downarrow(x) + \bar{q}_\uparrow(x) + \bar{q}_\downarrow(x)) \\ g_1(x) &= \sum_q \frac{e_q^2}{2}(q_\uparrow(x) - q_\downarrow(x) + \bar{q}_\uparrow(x) - \bar{q}_\downarrow(x)) \\ g_2(x) &= 0. \end{aligned} \tag{2.42}$$

Thus from the parton model we see that F_1 is the sum of the probabilities of finding a quark or antiquark with momentum fraction x in the hadron, while g_1 is the difference in the probabilities of finding quarks and antiquarks with momentum fraction x and spins parallel/anti-parallel to the hadron. We can also read off the Callan-Gross relation [10].

$$F_2(x) = 2xF_1(x). \tag{2.43}$$

As g_2 is identically zero, it has no interpretation in the parton model.

The parton model result for the transversity $h_1(x)$ is given by [11]

$$h_1(x) = \sum_q \frac{e_q^2}{2}(q_\perp(x) - q_\top(x) - \bar{q}_\perp(x) + \bar{q}_\top(x)), \tag{2.44}$$

where $q_\perp(x)$, $q_\top(x)$ are the transversely polarized quark distribution functions.

Finally we note that the parton model structure functions are only functions of x and are independent of Q^2. One way of explaining this is that as the structure functions are dimensionless, they can be expressed as functions of the dimensionless variables x and $\frac{Q^2}{M_N^2}$. However if the partons are essentially free particles then the hadron scale, i.e the hadron mass M_N, should be irrelevant and the structure functions should be independent of Q^2, and depend only on x. This is known as Bjorken Scaling [12] and provides evidence that hadrons are not fundamental particles, but have internal structure. However this scaling is only approximate, as the quarks are only approximately free. The QCD coupling constant α_s, while small, is not zero in the DIS regime and so will give rise to QCD corrections which allow a small dependence on Q^2. These corrections or "scaling violations" can be calculated in perturbation theory and so provide a test of QCD.

2.5 Operator product expansion

The hadronic tensor $W^{\mu\nu}$ (2.35) describes the hadronic part of the DIS cross-section. We can relate this to the Compton forward scattering amplitude

$$T^{\mu\nu} = i \int d^4x e^{-iq.x} \langle p(\vec{p}) | T(J_e^\mu(x) J_e^\nu(0)) | p(\vec{p}) \rangle \tag{2.45}$$

using the optical theorem[9] [8]. This gives

$$\mathrm{Im}(T^{\mu\nu}) = 2\pi W^{\mu\nu}. \tag{2.46}$$

$T^{\mu\nu}$ involves the matrix element of a product of two currents. One method of dealing with products of currents is to use the operator product expansion [13]. To illustrate the idea we consider a product of two local operators

$$\mathcal{O}_i(x)\mathcal{O}_j(0). \tag{2.47}$$

For small x the operators are practically at the same point, so for scales larger than x, the product will look like a local operator. Hence in the limit $x \to 0$ we can expand the operator product as a series of local operators

$$\mathcal{O}_i(x)\mathcal{O}_j(0) \underset{x \to 0}{=} \sum_k C_{ijk}(x)\mathcal{O}_k(0). \tag{2.48}$$

Note as we have made no assumptions yet about the external states, the coefficient functions $C_{ijk}(x)$ will depend on the operators $\mathcal{O}_i$, $\mathcal{O}_j$ and the separation x, but will otherwise be independent of the matrix element that is being calculated. In fact, all of the q dependence of the operator product is now contained in these coefficients. In momentum space this relation is written as

$$\int d^4x e^{iq.x} \mathcal{O}_i(x)\mathcal{O}_j(0) \underset{q \to \infty}{=} \sum_k C_{ijk}(q)\mathcal{O}_k(0). \tag{2.49}$$

[9] $T(J_1 J_2)$ is the time ordered product of the currents J_1, J_2.

States of definite dimension and spin can be used to form a basis for the expansion. An operator of spin n can be formed from the symmetric, traceless parts of a general operator of dimension d with n Lorentz indices

$$\mathcal{O}_d^{\mu_1 \cdots \mu_n}. \tag{2.50}$$

A dimensional analysis is useful in order to group together terms in order of their relevance. We can look at the contribution each term has to $L_{\mu\nu}W^{\mu\nu}$. The matrix element of $\mathcal{O}_d^{\mu_1 \cdots \mu_n}$ transforms as[10]

$$\langle p|\mathcal{O}_d^{\mu_1 \cdots \mu_n}|p\rangle \propto M_N^{d-n-2}\ \mathcal{S}[p^{\mu_1} \ldots p^{\mu_n}], \tag{2.51}$$

where $\mathcal{S}$ is projecting out the symmetric, traceless part of the tensor product, and M_N is the nucleon mass. Each of the free Lorentz indices must be either contracted with the external lepton momenta, or a q^α coming from the coefficient function. All of these will give terms of the order $p.q$. Also as $T^{\mu\nu}$ is dimensionless, all the terms in the expansion must also be dimensionless. Hence the coefficient function must have dimension Q^{2-d}. Putting this together we have the contribution of $\mathcal{O}_d^{\mu_1 \cdots \mu_n}$ given by

$$\begin{aligned} C_{\mu_1 \ldots \mu_n}\mathcal{O}_d^{\mu_1 \cdots \mu_n} &\propto \frac{(p.q)^n}{Q^n} Q^{2-d} M_N^{d-n-2} \\ &\propto \frac{(p.q)^n}{Q^{2n}} Q^{2-d+n} M_N^{d-n-2} \\ &\propto \omega^n \left(\frac{Q}{M_N}\right)^{2-d+n} \\ &\propto \omega^n \left(\frac{Q}{M_N}\right)^{2-t}, \end{aligned} \tag{2.52}$$

where t is the twist of the operator, defined as $t = dimension - spin$. The lowest possible gauge invariant operators are twist 2, with higher twist con-

[10] $|p\rangle$ has dimension M^{-1}.

tributions suppressed by factors of $(\frac{M_N}{Q})$.

A basis for twist 2 quark operators is formed from the symmetric traceless parts of

$$\begin{aligned} \mathcal{O}_q^{\mu_1..\mu_n} &= (\frac{i}{2})^{n-1}\bar{q}\gamma^{\mu_1}\overleftrightarrow{D}^{\mu_2}\cdots\overleftrightarrow{D}^{\mu_n}q \\ \mathcal{O}_{5q}^{\mu_1..\mu_n} &= (\frac{i}{2})^{n-1}\bar{q}\gamma^{\mu_1}\gamma_5\overleftrightarrow{D}^{\mu_2}\cdots\overleftrightarrow{D}^{\mu_n}q, \end{aligned} \tag{2.53}$$

while the basis for gluon operators is

$$\mathcal{O}_g^{\mu_1..\mu_n} = (\frac{i}{2})^{n-2}TrF^{\lambda\mu_1}\overleftrightarrow{D}^{\mu_2}\cdots\overleftrightarrow{D}^{\mu_{n-1}}F_\lambda^{\mu_n}. \tag{2.54}$$

however to lowest order in α_s the gluon operators can be ignored. The symmetric derivative $\overleftrightarrow{D}^\mu = \frac{1}{2}(\overrightarrow{D}^\mu - \overleftarrow{D}^\mu)$ is chosen so that the operators have simple behaviour under charge conjugation.

We now, through the operator product expansion, have a way of expanding a product of currents into a series of local operators of lowest twist. There is a problem with this approach though, as the operator product expansion is valid in the region $\omega \propto \frac{1}{Q} \to 0$ while the physical region of DIS is $1 < |\omega| < \infty$. However we can use analytic continuation to relate moments of structure functions in the physical region to calculable matrix elements. In order to see how this works, we first define the $\tilde{F}_1(x, Q^2)$ to be the structure function of $T^{\mu\nu}$ which is equivalent to $F_1(x, Q^2)$ of $W^{\mu\nu}$. Due to (2.52) we can expand $\tilde{F}_1(\omega)$[11]

$$\tilde{F}_1(\omega) = \sum_q \sum_n 2C_q^{F_1,n} v_q^n \omega^n, \tag{2.55}$$

[11]As we are using only lowest twist, up to $O(\frac{1}{Q^2})$ terms, $\tilde{F}_1$ can be written purely in terms of ω.

where $C_q^{F_1,n}$ are coefficient functions, which as we are in the OPE region, can be calculated perturbatively. v_q^n is given by

$$\langle p|\mathcal{O}_d^{\mu_1\cdots\mu_n}|p\rangle = 2v_q^n\ \mathcal{S}[p^{\mu_1}...p^{\mu_n}]. \tag{2.56}$$

The analytical structure of $\tilde{F}_1(\omega)$ is such that it will have branch cuts along

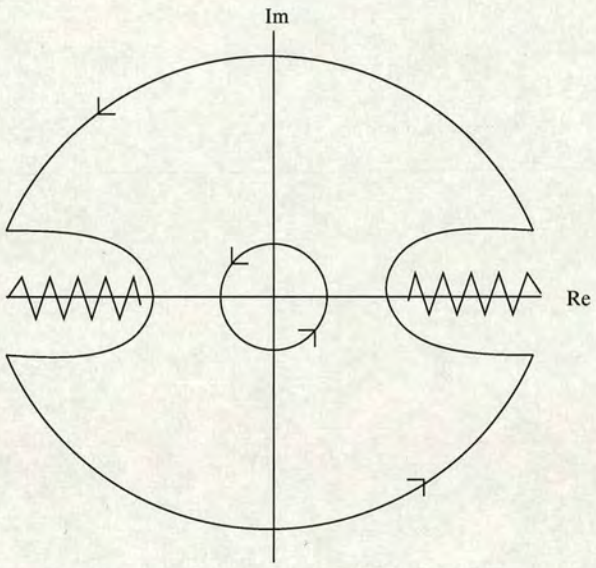

Figure 2.9: The analytic continuation of $\tilde{F}_1(\omega)$ showing the initial contour $|\omega| < 1$, and this contour expanded to infinity.

the real axis in the physical region (corresponding to a continuum of possible intermediate states), but no other singularities (see Figure 2.9). Hence we can pick out individual terms in the expansion by noting that

$$\sum_q 2C_q^{F_1,n}v_q^n = \frac{1}{2\pi i}\oint_{|\omega|<1} d\omega \frac{\tilde{F}_1(\omega)}{\omega^{n+1}}. \tag{2.57}$$

This contour can be expanded above and below the branch cuts, out to infinity. Assuming that the contribution from the contour at infinity vanishes,

then the only contribution to the contour will come from the discontinuity across the branch cuts. This is given by

$$\tilde{F}_1(\omega + i\epsilon) - \tilde{F}_1(\omega - i\epsilon) = 2iIm\tilde{F}_1(\omega) = 4\pi i F_1(\omega), \tag{2.58}$$

so we have

$$\sum_q 2C_q^{F_1,n} v_q^n = 2(1 - (-1)^{n+1}) \int_1^\infty d\omega \frac{F_1(\omega)}{\omega^{n+1}}. \tag{2.59}$$

Substituting in $x = w^{-1}$ we get the result

$$2\int_0^1 dx x^{n-1} F_1(x, Q^2) = \sum_q C_q^{F_1,n} v_q^n + O(\frac{1}{Q^2}), \tag{2.60}$$

where n is even. Similar rules can be derived[12] for other structure functions to give

$$\begin{aligned}
\int_0^1 dx x^{n-2} F_2(x, Q^2) &= \sum_q C_q^{F_2,n} v_q^n + O(\frac{1}{Q^2}) \\
2\int_0^1 dx x^n g_1(x, Q^2) &= \sum_q C_q^{g_1,n} a_q^n + O(\frac{1}{Q^2}) \\
2\int_0^1 dx x^n g_2(x, Q^2) &= \frac{n}{n+1} \sum_q (C_q^{g_2,n} d_q^n - C_q^{g_1,n} a_q^n) + O(\frac{1}{Q^2}) \\
2\int_0^1 dx x^n h_1(x, Q^2) &= \frac{n}{n+1} \sum_q C_q^{h_1,n} h_q^n + O(\frac{1}{Q^2}).
\end{aligned} \tag{2.61}$$

The unpolarized moment rules are true for all even $n \geq 2$, while the polarized moments hold for even $n \geq 0$. For the polarized structure functions, with polarization vector s^α, we must measure matrix elements of the form $\mathcal{O}_{5q}^{\alpha\{\mu_1..\mu_n\}}$. a_q^n is then the matrix element of the totally symmeterized operator $\mathcal{O}_{5q}^{\{\alpha\mu_1..\mu_n\}}$ and d_q^n is the matrix element of the remaining piece. For

[12] see for example [9].

the transversity $h_1(x, Q^2)$, h_q^n is the matrix element of the tensor operator defined by

$$\mathcal{O}_{\sigma q}^{\alpha\{\mu_1..\mu_n\}} = i^n \bar{q}\sigma^{\alpha\{\mu_1}\gamma_5 \overleftrightarrow{D}^{\mu_2} \cdots \overleftrightarrow{D}^{\mu_n\}} q, \tag{2.62}$$

where $\sigma^{\mu\nu} = \frac{1}{2}[\gamma^\mu, \gamma^\nu]$.

These moments also have parton model interpretations. The moments of the unpolarized structure functions v_q^n are powers of the fraction of the nucleon momentum carried by the parton, while the polarized moments are related to the fraction of the nucleon spin carried by the parton.

Chapter 3

Lattice QCD

The QCD Lagrangian while formally quite simple, is in actual fact very hard to solve due to its non-linear nature. While perturbation theory can be applied at high energy scales, the large value of the coupling α_s at low energies causes perturbation theory to fail. To study low energy QCD phenomena such as hadron masses and matrix elements we need a non-perturbative approach.

Lattice gauge theory provides a non-perturbative formulation of QCD. In this formulation the path integral (or partition function) is first analytically continued to imaginary times by performing a Wick rotation, changing the Minkowski space-time to a Euclidean one. This transforms the partition function into the form of a statistical ensemble average. The continuum is then replaced by a 4-D hypercubic lattice of points with a finite lattice spacing a. This reduces the infinite degrees of freedom in the partition function to a finite (although still large) number. The addition of a lattice spacing also introduces a minimum length scale into the theory which is the equivalent of

a momentum cutoff and so regularizes the Feynman integrals. By removing the lattice structure (i.e. taking the limit as $a \to 0$) while keeping physical results constant we can define a renormalization procedure. While the lattice allows us to precisely define our path integral, it is still an integral over a large number of degrees of freedom and so we must employ Monte-Carlo techniques in order to evaluate it.

3.1 Lattice gauge theory

In quantum field theory, all the physical information about a system is contained within vacuum expectation values of time-ordered products of field operators. These Green functions can be generated from the partition function, which for QCD takes the form

$$Z = \int \mathcal{D}\mathcal{U}\mathcal{D}\bar{\psi}\mathcal{D}\psi e^{iS_{QCD}}, \tag{3.1}$$

where

$$S_{QCD} = -\frac{1}{4}Tr\int d^4x \mathcal{F}^{\mu\nu}\mathcal{F}_{\mu\nu} + \int d^4x \bar{\psi}(i\gamma^\mu \mathcal{D}_\mu - m)\psi, \tag{3.2}$$

and the integral is formally defined as the sum over all possible field configurations. The path integral representation of these Green functions is then given by

$$G_{\alpha_1,..,\alpha_k,\beta_1,..,\beta_k}(x_1,..,x_k,y_1,..,y_k) =$$

$$\frac{1}{Z}\int \mathcal{D}\mathcal{U}\mathcal{D}\bar{\psi}\mathcal{D}\psi\psi_{\alpha_1}(x_1)..\psi_{\alpha_k}(x_k)\bar{\psi}_{\beta_1}(y_1)..\bar{\psi}_{\beta_k}(y_k)e^{iS_{QCD}}. \tag{3.3}$$

However the paths here are weighted with an oscillating function $e^{iS_{QCD}}$, and so are not well suited to numerical calculations. We therefore perform a Wick

rotation to reformulate the theory in a Euclidean space-time. This is done by taking $t \to -i\tau$. The new Euclidean path integral is then

$$Z = \int \mathcal{D}\mathcal{U}\mathcal{D}\bar{\psi}\mathcal{D}\psi e^{-S^E_{QCD}} \tag{3.4}$$

$$S^E_{QCD}{}^1 = \frac{1}{4}Tr\int d^4x \mathcal{F}_{\mu\nu}\mathcal{F}_{\mu\nu} + \int d^4x \bar{\psi}(\gamma^\mu_E \mathcal{D}_\mu + m)\psi, \tag{3.5}$$

and now our Euclidean Green functions are

$$\begin{aligned}&\langle \psi_{\alpha_1}(x_1)..\psi_{\alpha_k}(x_k)\bar{\psi}_{\beta_1}(y_1)..\bar{\psi}_{\beta_k}(y_k)\rangle \\ &= \frac{1}{Z}\int \mathcal{D}\mathcal{U}\mathcal{D}\bar{\psi}\mathcal{D}\psi\psi_{\alpha_1}(x_1)..\psi_{\alpha_k}(x_k)\bar{\psi}_{\beta_1}(y_1)..\bar{\psi}_{\beta_k}(y_k)e^{-S^E_{QCD}}.\end{aligned} \tag{3.6}$$

From now on we will always work in Euclidean space, so the Euclidean superscripts will be dropped.

This new Euclidean path integral is completely equivalent to the original Minkowski path integral, however now the paths in the integral are weighted with a real factor and the path integral is in the form of a statistical ensemble average. However we cannot yet treat this like a statistical mechanics problem as firstly we still haven't precisely defined the path integral, and also the action contains Grassmann valued fields. While the Grassmann valued fields can be dealt with simply due to the fact that the fermion integration can be performed analytically, to deal with the first problem we have to introduce the lattice structure and discretize the action.

[1]For Gamma matrix conventions, see Appendix 10.1

3.1.1 The Lattice Action

As mentioned above, to define the path integral we must give it a finite number of degrees of freedom. We do this by discretizing our space-time into a hyper-cubic lattice of points, and introduce a finite length scale a which will define our lattice spacing. This forces us however to make a discretized version of the action (3.5). Our continuum space-time index x_μ is thus replaced by a hyper-cubic index n_μ, the integrals become finite sums, the derivatives become finite differences, and in order to make our action dimensionless we scale all the parameters according to their dimension. This procedure can be summarized as

$$\begin{aligned} x_\mu &\rightarrow an_\mu \\ \psi(x) &\rightarrow \frac{1}{a^{3/2}}\psi(n) \\ \bar{\psi}(x) &\rightarrow \frac{1}{a^{3/2}}\bar{\psi}(n) \\ m &\rightarrow \frac{1}{a}m \\ \int d^4x &\rightarrow a^4 \sum \\ \partial_\mu \psi(x) &\rightarrow \frac{1}{a^{5/2}}\partial_\mu \psi(n), \end{aligned} \tag{3.7}$$

where the derivative is now given by the finite difference

$$\partial_\mu \psi(n) = \frac{1}{2}[\psi(n+\hat{\mu}) - \psi(n-\hat{\mu})]. \tag{3.8}$$

As with the continuum case we must ensure that our discretized action is gauge invariant. In the prescription just described, the finite difference will now leave the fermionic part of the action with terms that are bilinear in the

fermionic fields, but at different points in spacetime i.e. terms of the form

$$\bar{\psi}(n)\psi(n+\hat{\mu}). \tag{3.9}$$

Under a local gauge transformation $S(n)$ these terms will transform as

$$\bar{\psi}(n)\psi(n+\hat{\mu}) \longrightarrow \bar{\psi}(n)S^{\dagger}(n)S(n+\hat{\mu})\psi(n+\hat{\mu}). \tag{3.10}$$

This is clearly not gauge invariant. In order to preserve gauge invariance, we introduce a parallel transporter

$$U(n,n+\hat{\mu}) \equiv U_{\mu}(n) = e^{iagA_{\mu}(n)}, \tag{3.11}$$

where $A_{\mu}(n)$ is the gauge potential. Under a local gauge transformation U transforms as

$$U_{\mu}(n) \longrightarrow S(n)U_{\mu}(n)S^{\dagger}(n+\hat{\mu}). \tag{3.12}$$

The product $\bar{\psi}(n)U_{\mu}(n)\psi(n+\hat{\mu})$ is thus gauge invariant. Note that this parallel transporter or link variable is directed, and so the parallel transporter along the same link in the opposite direction is

$$U(n+\hat{\mu},n) \equiv U_{\mu}^{\dagger}(n) = e^{-iagA_{\mu}(n)}. \tag{3.13}$$

Hence just as in the continuum case we are forced to replace the ordinary partial derivative with a covariant derivative which is dependent on the gauge potential in order to maintain gauge invariance. The new derivative term is then

$$D_{\mu}\psi(n) = \frac{1}{2}[U_{\mu}(n)\psi(n+\hat{\mu}) - U_{\mu}^{\dagger}(n-\hat{\mu})\psi(n-\hat{\mu})]. \tag{3.14}$$

Putting this all together we can arrive at a discretized version of the fermion action

$$S_F = \sum_{n,\mu}\frac{1}{2}\bar{\psi}(n)\gamma_{\mu}[U_{\mu}(n)\psi(n+\hat{\mu}) - U_{\mu}^{\dagger}(n-\hat{\mu})\psi(n-\hat{\mu})] + \sum_{n} m\bar{\psi}(n)\psi(n). \tag{3.15}$$

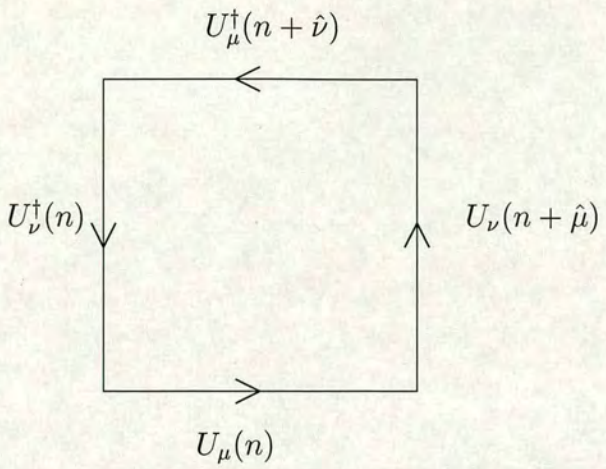

Figure 3.1: The plaquette $U_{\mu\nu}(n)$.

If we now look at the gauge action, it must be made out of the link variables, and again be gauge invariant. The link variables themselves are not gauge invariant (see 3.12), however the trace of any closed loop of link variables is. The smallest such loop, or plaquette (see Figure 3.1) is given by:

$$U_{\mu\nu}(n) = U_\mu(n)U_\nu(n+\hat{\mu})U_\mu^\dagger(n+\hat{\nu})U_\nu^\dagger(n). \tag{3.16}$$

Substituting (3.11) into this expression we get

$$U_{\mu\nu}(n) = e^{iagA_\mu(n)}e^{iagA_\nu(n+\hat{\mu})}e^{-iagA_\mu(n+\hat{\nu})}e^{-iagA_\nu(n)}. \tag{3.17}$$

For small lattice spacing we can expand this expression in powers of a

$$A_\nu(n+\hat{\mu}) = A_\nu(n) + a\partial_\mu A_\nu(n) + \mathcal{O}(a^2). \tag{3.18}$$

Substituting this into (3.17) and repeated use of the Baker-Campbell-Hausdorff formula

$$e^A e^B = e^{A+B+\frac{1}{2}[A,B]}, \tag{3.19}$$

we find, ignoring terms above $\mathcal{O}(a^2)$,

$$\begin{aligned} U_{\mu\nu}(n) &= e^{iagA_\mu(n)+iagA_\nu(n)+ia^2g\partial_\mu A_\nu(n)-\frac{1}{2}a^2g^2[A_\mu(n),A_\nu(n)]} \\ &\quad \times e^{-iagA_\mu(n)-iagA_\nu(n)-ia^2g\partial_\nu A_\mu(n)-\frac{1}{2}a^2g^2[A_\mu(n),A_\nu(n)]} \\ &= e^{ia^2g\partial_\mu A_\nu(n)-ia^2g\partial_\nu A_\mu(n)-a^2g^2[A_\mu(n),A_\nu(n)]} \\ &= e^{ia^2g\{\partial_\mu A_\nu(n)-\partial_\nu A_\mu(n)+ig[A_\mu(n),A_\nu(n)]\}}. \end{aligned} \tag{3.20}$$

This is equivalent to

$$U_{\mu\nu}(n) = e^{iga^2F_{\mu\nu}(n)}, \tag{3.21}$$

where $F_{\mu\nu}$ is the discretized version of the field strength tensor which in the limit $a \to 0$ is given by

$$F_{\mu\nu} = \partial_\mu A_\nu - \partial_\nu A_\mu + ig[A_\mu, A_\nu]. \tag{3.22}$$

A simple expansion of (3.21) gives

$$U_{\mu\nu}(n) = 1 + iga^2F_{\mu\nu}(n) - \frac{g^2a^4}{2}F_{\mu\nu}(n)F_{\mu\nu}(n) + \mathcal{O}(a^6). \tag{3.23}$$

We can then use this to to define a gauge action S_G by

$$S_G = \frac{1}{3}\beta \sum_{plaq} ReTr(1 - U_{\mu\nu}), \tag{3.24}$$

where

$$\beta = \frac{6}{g^2}. \tag{3.25}$$

We have now formulated a discretized version of both the fermion and gauge parts of the action. We must now check that they give the correct continuum limit. By substituting (3.23) into (3.24) and taking the limit $a \to 0$, it's clear that we will get the correct continuum gauge action. However the naive prescription given for the fermion action (3.15) does not give the correct continuum limit.

3.1.2 Fermion Doubling

To see why the naive discretization of the fermion action fails to give the correct continuum limit, we look at the free field propagator. The free field action ($U_\mu(n) = 1$) is given by

$$S_F = \sum_{n,\mu} \frac{1}{2}\bar{\psi}(n)\gamma_\mu[\psi(n+\hat{\mu}) - \psi(n-\hat{\mu})] + \sum_n m\bar{\psi}(n)\psi(n). \tag{3.26}$$

this can be rewritten as

$$S_F = \sum_{n,l} \bar{\psi}(n)K(n,l)\psi(l), \tag{3.27}$$

where

$$K(n,l) = \sum_\mu \frac{1}{2}\gamma_\mu[\delta_{l,n+\hat{\mu}} - \delta_{l,n-\hat{\mu}}] + m\delta_{l,n}. \tag{3.28}$$

The propagator is given by the inverse of this matrix. We can obtain this easily by taking the Fourier transform of $K(n,l)$

$$K(n,l) = \int_{-\pi}^{\pi} \frac{d^4p}{(2\pi)^4}(i\gamma_\mu \sin(p_\mu) + m)e^{ip(l-n)}, \tag{3.29}$$

where a sum over μ is assumed. $K^{-1}(n,l)$ is then given by

$$K^{-1}(n,l) = \int_{-\pi}^{\pi} \frac{d^4p}{(2\pi)^4} \frac{(-i\gamma_\mu \sin(p_\mu) + m)}{\sin^2(p_\mu) + m^2} e^{ip(n-l)}, \tag{3.30}$$

or on replacing the parameters by their dimensional counterparts and taking the limit as $a \to 0$,

$$K^{-1}(x,y) = \lim_{a\to 0} \int_{-\pi/a}^{\pi/a} \frac{d^4p}{(2\pi)^4} \frac{(\frac{-i}{a}\gamma_\mu \sin(p_\mu a) + m)}{\frac{1}{a^2}\sin^2(p_\mu a) + m^2} e^{ip(x-y)}. \tag{3.31}$$

Now this expression is the form of a single particle propagator, but the denominator has sixteen zeros corresponding to sixteen propagators. In

the limit of vanishing quark mass, these correspond to particles with 3-momentum components either 0 or $\pm\frac{\pi}{a}$. So when the continuum limit is taken we end up with sixteen species of fermions instead of one. This is the fermion doubling problem. It should be noted that this is not an aberration caused by a poor choice of discretization, nor is it cured by the introduction of gauge fields. In fact the Nielson-Ninomiya theorem [14] shows that problem occurs under very general conditions and is linked to the chiral properties of the action.

3.2 Chiral symmetry

In any simulation of a physical theory it is advisable that your simulation matches your theory as closely as possible. It is obviously then desirable to reproduce as many of the symmetries of your original theory as possible. In particular if we wish to probe the chiral regime of QCD, we would be well advised to run simulations with an action that has good chiral properties. The fermionic part of the QCD action has a continuous chiral symmetry. To be more specific it is invariant under chiral transformations of the fermion fields. Under such transformations the fields ψ and $\bar{\psi}$ transform as

$$\begin{aligned} \psi &\to e^{i\alpha\gamma_5}\psi \\ \bar{\psi} &\to \bar{\psi}e^{i\alpha\gamma_5}, \end{aligned} \tag{3.32}$$

which means the action (where $\not{\mathcal{D}} = \mathcal{D}_\mu\gamma_\mu$) transforms in the zero mass limit as

$$\bar{\psi}\not{\mathcal{D}}\psi \to \bar{\psi}e^{i\alpha\gamma_5}\not{\mathcal{D}}e^{i\alpha\gamma_5}\psi. \tag{3.33}$$

If we now look at infinitesimal transformations where $\alpha \ll 1$, the above transformation law becomes

$$\bar{\psi}\not{\mathcal{D}}\psi \rightarrow \bar{\psi}\not{\mathcal{D}}\psi + \bar{\psi}(i\alpha\gamma_5\not{\mathcal{D}} + i\alpha\not{\mathcal{D}}\gamma_5)\psi. \tag{3.34}$$

It clear then if we want our action to be invariant under chiral transformations, then the second term in the above expression must be zero. This leads to the condition that

$$\{\gamma_5, \not{\mathcal{D}}\} = 0. \tag{3.35}$$

It is at this point that we run into the Nielson-Ninomiya Theorem that was alluded to earlier. This theorem states that it is not possible to find a consistent lattice action which simultaneously possesses all the properties given below :

- A local $\not{\mathcal{D}}$ operator
- The correct continuum limit
- $\{\gamma_5, \not{\mathcal{D}}\} = 0$
- No doublers.

This would imply that in order to obtain the correct continuum limit, with no doublers, and have a local action, then we must sacrifice chiral symmetry. In general this is precisely what was done.

3.2.1 Wilson Fermions

The original solution to the fermion doubling problem was proposed by Wilson [15]. It involves adding an extra term to the action which when dimensions are reintroduced is proportional to the lattice spacing. This term

will then vanish in the naive continuum limit, but will remove the doublers by giving all the non-zero momentum excitations a mass which is inversely proportional to the lattice spacing. Wilson's action is then

$$S_F^W = S_F - \frac{r}{2}\sum_n \bar{\psi}\Box\psi, \tag{3.36}$$

where S_F is the naive action (3.15), r is the Wilson parameter (and is usually chosen to be 1) and $\Box$ is the four dimensional lattice Laplacian defined by

$$\Box\psi(n) = \sum_\mu [U_\mu(n)\psi(n+\hat{\mu}) + U_\mu^\dagger(n-\hat{\mu})\psi(n-\hat{\mu})] - 8\psi(n). \tag{3.37}$$

Proceeding as with the naive case we look at the free field propagator. Again we can write the action in the form

$$S_F^W = \sum_{n,l} \bar{\psi}(n)K(n,l)\psi(l), \tag{3.38}$$

where $K(n,l)$ is given now by

$$K(n,l) = (m+4r)\delta_{l,n} - \frac{1}{2}\sum_\mu [(r-\gamma_\mu)\delta_{l,n+\hat{\mu}} + (r+\gamma_\mu)\delta_{l,n-\hat{\mu}}]. \tag{3.39}$$

Inverting this as before to get the free particle propagator K^{-1} and reintroducing the dimensional variables we get

$$K^{-1}(x,y) = \lim_{a\to 0}\int_{-\pi/a}^{\pi/a} \frac{d^4p}{(2\pi)^4} \frac{(\frac{-i}{a}\gamma_\mu sin(p_\mu a) + m)}{\frac{1}{a^2}sin^2(p_\mu a) + m(p)^2} e^{ip(x-y)}, \tag{3.40}$$

where the parameter $m(p)$ is now momentum dependent quantity given by

$$m(p) = m + \frac{2r}{a}\sum_\mu sin^2(p_\mu a/2). \tag{3.41}$$

This momentum dependent mass parameter solves the doubling problem. For the $p_\mu = (0,0,0,0)$ fermion, $m(p)$ is simply m as before. However for

the other 15 species which have non-zero components of momenta, $m(p)$ picks up a term proportional to $2r/a$ which diverges as $a \to 0$. Hence these species decouple in the continuum limit, leaving only one species which can propagate. While this has solved the problem of the extra fermions, the Wilson action (3.38) clearly no longer preserves chiral symmetry as expected from Nielson-Ninomiya.

An alternative to Wilson-like fermions is the staggered formulation. This preserves a $U(1) \otimes U(1)$ remnant of the full $U(4) \otimes U(4)$ chiral symmetry, however this is done at the expense of other symmetries, in particular flavour symmetry [16]. As such I will not discuss this formulation here.

3.2.2 Ginsparg-Wilson relation

A solution to the problem of simulating chiral fermions was first proposed by Ginsparg and Wilson [3], and more recently by Lüscher [17]. The method was to define a lattice version of chiral symmetry at finite lattice spacing which would reduce to the usual chiral symmetry in the continuum limit. Thus the lattice fermion fields would transform under a new on-shell chiral symmetry as follows

$$\begin{aligned} \psi &\to e^{i\alpha\gamma_5(1-\frac{a}{2}\not{p})}\psi \\ \bar{\psi} &\to \bar{\psi}e^{i\alpha(1-\frac{a}{2}\not{p})\gamma_5}. \end{aligned} \tag{3.42}$$

This as before leads to the transformation law for the action

$$\bar{\psi}\not{p}\psi \to \bar{\psi}e^{i\alpha\gamma_5(1-\frac{a}{2}\not{p})}\not{p}\,e^{i\alpha(1-\frac{a}{2}\not{p})\gamma_5}\psi. \tag{3.43}$$

If we again look at infinitesimal transformations we have

$$\not{D} = 1 + i\alpha((1 - \frac{a}{2}\not{D})\gamma_5\not{D} + \not{D}\gamma_5(1 - \frac{a}{2}\not{D})). \tag{3.44}$$

This means as before that if we wish the action to be invariant under these new transformations we must have :

$$\{\gamma_5, \not{D}\} = a\not{D}\gamma_5\not{D}. \tag{3.45}$$

This is known as the Ginsparg-Wilson relation.

This lattice version of chiral symmetry thus no longer requires that γ_5 anti-commutes with $\not{D}$, replacing that condition with the weaker condition that they anti-commute up to some factor, which is proportional to the lattice spacing. This has several useful consequences. Firstly, since it only differs from continuum chiral symmetry by a term proportional to a, then in the continuum we regain full chiral symmetry. Secondly, for any ψ that satisfies the Dirac equation this is an exact chiral symmetry at fixed, non-zero lattice spacing. Finally, since we have dropped the condition that γ_5 anti-commute with $\not{D}$, we can avoid a conflict with the Nielson-Ninomiya theorem.

3.2.3 Overlap formalism

While the Ginsparg-Wilson relation gives a condition which the Dirac operator must satisfy in order to preserve chiral symmetry, it gives no information on the form of $\not{D}$. A possible solution, due to Neuberger [4] is the overlap formalism. The construction proceeds as follows :

We first write our $\not{D}$ in the form

$$a\not{D} = 1 + \gamma_5 V. \tag{3.46}$$

Note we are free to do this without loss of generality as (3.46) can be considered as the definition of V. If we now impose γ_5 hermiticity we have

$$\gamma_5 \not{D} \gamma_5 = \not{D}^\dagger, \tag{3.47}$$

and so

$$a\not{D}^\dagger = 1 + V^\dagger \gamma_5 = 1 + V\gamma_5. \tag{3.48}$$

Hence $V = V^\dagger$ and V is Hermitian.

The GW relation also constrains the form of V. By multiplying (3.45) on the left by γ_5 and using (3.47) we have

$$\not{D} + \not{D}^\dagger = a\not{D}^\dagger \not{D}, \tag{3.49}$$

so

$$\begin{aligned} \frac{1}{a}(1+\gamma_5 V) + \frac{1}{a}(1+V^\dagger\gamma_5) &= \frac{a}{a^2}(1+V^\dagger\gamma_5)(1+\gamma_5 V) \\ 2 + \gamma_5 V + V\gamma_5 &= 1 + \gamma_5 V + V\gamma_5 + V^2. \end{aligned} \tag{3.50}$$

Hence $V^2 = 1$ and so V is also unitary. So we need a V which is hermitian and unitary. Neuberger's solution was the operator

$$V = \frac{\gamma_5(aD_w - 1)}{\sqrt{(aD_w - 1)^\dagger (aD_w - 1)}}, \tag{3.51}$$

where D_w is any valid lattice Dirac operator, but is usually taken to be the Wilson-Dirac operator. Since the D_w is also γ_5 Hermitian (which is easily seen from the Wilson action (3.36)), then it is clear that this expression for V satisfies both the requirements of unitarity and hermiticity. Putting this form back into (3.46) we have

$$a\not{D} = 1 + \frac{(aD_w - 1)}{\sqrt{(aD_w - 1)^\dagger (aD_w - 1)}}$$

$$= 1+\gamma_5\frac{\gamma_5(aD_w-1)}{\sqrt{[\gamma_5(aD_w-1)]^\dagger\gamma_5(aD_w-1)}}$$
$$= 1+\gamma_5\frac{\gamma_5(aD_w-1)}{\sqrt{[\gamma_5(aD_w-1)]^2}}, \tag{3.52}$$

where the last line comes from the fact that $[\gamma_5(aD_w - 1)]$ is Hermitian. Hence we can write this expression as

$$a\not{\mathcal{D}} = 1+\gamma_5\mathrm{sgn}[\gamma_5(aD_w-1)], \tag{3.53}$$

where

$$\mathrm{sgn}(M) = \frac{M}{\sqrt{M^2}}. \tag{3.54}$$

For a real number x, $\mathrm{sgn}(x) = -1$ for $x < 0$, and $\mathrm{sgn}(x) = 1$ for $x > 0$

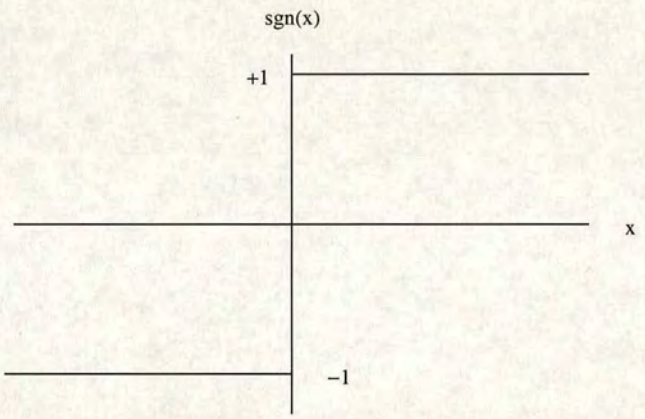

Figure 3.2: $\mathrm{sgn}(x)$.

(see Figure 3.2). For a matrix M, we define the sgn function as equivalent to diagonalising the matrix M, and then taking the sign of the eigenvalues. This operator satisfies the Ginsparg-Wilson relation by construction, so all that is left to check now is that it gives the correct continuum limit. This

is easily seen by looking at (3.52). If $\not{\partial}$ is the continuum derivative $\gamma_\mu \partial_\mu$ we can write this as

$$\begin{aligned} a\not{D} &= 1 + \gamma_5 \frac{\gamma_5(a\not{\partial} + O(a^2) - 1)}{\sqrt{[\gamma_5(a\not{\partial} + O(a^2) - 1)]^2}} \\ &= 1 + \frac{(a\not{\partial} - 1)}{\sqrt{\gamma_5(a\not{\partial} - 1)\gamma_5(a\not{\partial} - 1)}} + O(a^2) \\ &= 1 + \frac{(a\not{\partial} - 1)}{\sqrt{(1 + a\not{\partial})(1 - a\not{\partial})}} + O(a^2) \\ &= a\not{\partial} + O(a^2). \end{aligned} \tag{3.55}$$

So $\not{D}$ gives the correct continuum limit so long as D_w does, again reinforcing that any valid action can be used for D_w. So far we have only dealt with the massless overlap Dirac operator. We can define a massive operator

$$aD_{ov} = (1 + \frac{am_q}{2}) + (1 - \frac{am_q}{2})\gamma_5 \mathrm{sgn}(\gamma_5(D_w - 1)), \tag{3.56}$$

which by similar arguments to (3.55) can be shown to be the continuum Dirac operator with bare mass m_q.

While we now have a mass term for the quarks we are simulating, we can still vary the mass parameter for the auxiliary action D_w. The spectrum of the Wilson Dirac operator is given schematically by Figure 3.3, where the offset on the real axis is the mass. For physical (small) quark masses this offset is very small, and fluctuations can cause D_w to have very near-zero modes. This is problematic as the time taken to invert the operator is greatly dependent on the norm of the lowest lying eigenvalue. However as we are merely taking the sgn of D_w, we are free to choose any mass parameter ρ without affecting the continuum limit of the system. In fact, an appropriate choice can help reduce the computational cost of the inversion. If we choose

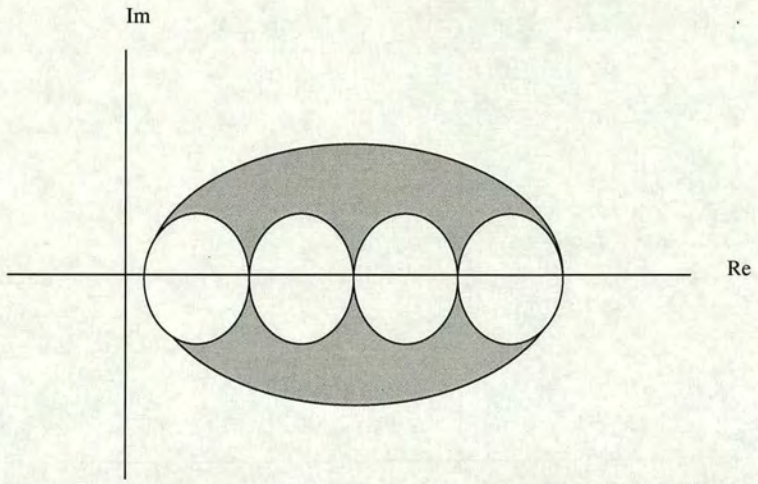

Figure 3.3: Wilson-Dirac eigenvalues with positive mass term.

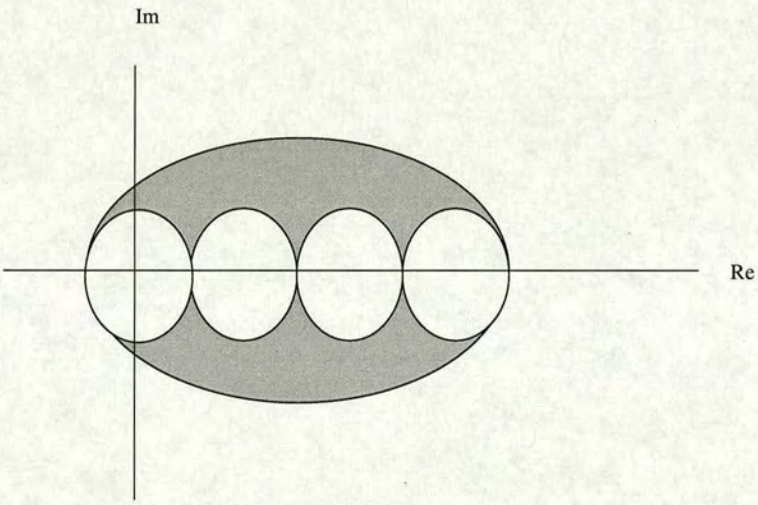

Figure 3.4: Wilson-Dirac eigenvalues with negative mass term.

a negative mass parameter as in Figure 3.4 then we are hopefully in a region which has very few low-lying eigenvalues. To put in a particular value of ρ

we exchange $(aD_w - 1)$ with $(aD_w - \rho)$ in (3.53). However this will require a rescaling of $\not{D}$ since in the continuum limit

$$\lim_{a\to 0} \gamma_5 \mathrm{sgn}[\gamma_5(aD_w - \rho)] = \frac{a\not{\partial} - \rho}{\rho}. \tag{3.57}$$

This implies a rescaling of (3.53) by ρ, so now

$$a\not{D} = \rho(1 + \gamma_5 \mathrm{sgn}[\gamma_5(aD_w - \rho)]), \tag{3.58}$$

and hence the massive overlap operator (3.56) is now given by

$$aD_{ov} = \rho(1 + \frac{am_q}{2\rho}) + \rho(1 - \frac{am_q}{2\rho})\gamma_5 \mathrm{sgn}(\gamma_5(aD_w - \rho)). \tag{3.59}$$

This is the massive overlap Dirac operator that will be used to run simulations. All that is left to do is to work out how to apply the sgn function in the most efficient manner.

3.3 Rational approximations

While the application of the sgn function is mathematically well defined for a matrix, it is not something which is particularly practical for implementation on a computer. The operator D_w is a very large sparse matrix, and diagonalising this is prohibitively expensive. An alternative to applying the sgn operator itself, is to find a rational approximation to the sgn function

$$\mathrm{sgn}(x) \approx \mathrm{sgn}_{m,n}(x) \equiv \frac{P_m(x)}{Q_n(x)}. \tag{3.60}$$

We wish to find a rational approximation to a constant odd function. This can be done by finding a rational approximation $r(x)$ of the function $\frac{1}{\sqrt{x}}$ and then forming the function $xr(x^2)$. The sgn function is discontinuous at

the origin, while our approximation will be a continuous function. Hence we approximate $\mathrm{sgn}(x)$ over the interval $[\xi, 1]$ with $\xi > 0$. Note we are free to scale the approximation interval to whatever value we like as $\mathrm{sgn}(x) = \mathrm{sgn}(kx)$. The approximation can be written in the form

$$\mathrm{sgn}_{2n+1,2n}(x) = xc_0 \frac{\prod_{k=1}^{n}(x^2 + p_k)}{\prod_{k=1}^{n}(x^2 + q_k)}. \tag{3.61}$$

We can then expand this rational function as a partial fraction [18]

$$\mathrm{sgn}_{2n+1,2n}(x) = x(c_0 + \sum_{k=1}^{n} \frac{c_k}{(x^2 + q_k)}); \qquad c_k = c_0 \frac{\prod_{i=1}^{n}(q_k + p_i)}{\prod_{i=1, i\neq k}^{n}(q_k - q_i)}. \tag{3.62}$$

As every term in this approximation is now of the form $\frac{1}{x^2+s}$ where s is some shift, then the cost of applying this operator is roughly the same as one Conjugate gradient (CG) [19] inversion of x^2 (or in our case $(\gamma_5 D_w)^2$) [20].

While we now have a functional form for our rational approximation, we still don't know the coefficients c_0, p_k, q_k. Chebyshev's theorem states that to any degree there is a unique optimal rational approximation to a continuous function on a unit interval (for a proof see [21]). This optimal function can be found by iterative methods such as the Remez algorithm [22]. However for the case of the sgn function, the optimal rational approximation is known analytically. The result is due to Zolotarev, who showed that the coefficients of the optimal approximation can be written in terms of the Jacobi elliptic functions [23]. For a detailed discussion on how to calculate these coefficients see [24].

The accuracy of our rational approximation, for a given order, will depend on the range of approximation region. As the spectrum of $(\gamma_5 D_w)^2$ typically contains a few isolated low-lying eigenmodes and a dense continuum above, in practice we project out a number of the lowest lying eigenvalues and deal

with them explicitly before inverting $(\gamma_5 D_w)^2$. This ensures the accuracy of our approximation over the whole remaining spectrum. Also, as the cost of the Krylov space inversion of $(\gamma_5 D_w)^2$ is determined by the matrix's condition number, this makes a big difference to the time taken to apply $\mathrm{sgn}_{2n+1,2n}(x)$.

3.4 Conjugate gradient and chiral sources

When we come to form propagators, we must invert the overlap operator (3.59). This then leads to a nested CG procedure, with an inner CG needed to apply the sgn function, and an outer CG to invert the resulting operator. The propagator G is found by solving the equation

$$D_{ov} G = s, \tag{3.63}$$

where s^a_α is a fermionic source, which for point sources (we deal with smeared sources in Section 4.3.1) is a delta-function in spin, colour and space-time. Conjugate gradient solves linear systems of the form

$$Ax = b, \tag{3.64}$$

where A is a positive definite, hermitian matrix, and x and b are vectors. Hence we solve for one spin/colour component of G at a time, and must perform 12 inversions. For the inner CG solve $(\gamma_5 D_w)^2$ is obviously hermitian, positive definite, however D_{ov} is not and so CG cannot be used directly to invert it. We avoid this problem by solving the auxiliary system

$$D^\dagger_{ov} D_{ov} G = D^\dagger_{ov} s, \tag{3.65}$$

which will give the same result. While this allows us to use CG, it now seems that for every step in the inversion we must apply the sgn function twice.

This can be avoided however as we are using a chiral spin basis[2]. Our sources are diagonal in spin space, and so in this basis are eigenstates of chirality, i.e for a chiral source vector χ

$$\gamma_5 \chi = \pm \chi. \tag{3.66}$$

If for simplicity we just look at the massless case (the massive case follows an identical argument) and look at D_{ov} in the form (3.46), the Krylov space for our inversion will be formed by successive applications of $D_{ov}^\dagger D_{ov}$ to the source vector. If we have a chiral source χ then

$$\begin{aligned} D_{ov}^\dagger D_{ov} \chi &= (1 + V\gamma_5)(1 + \gamma_5 V)\chi \\ &= (2 + \gamma_5 V + V\gamma_5)\chi \\ &= (2 + (\gamma_5 \pm 1)V)\chi. \end{aligned} \tag{3.67}$$

Hence we only need to apply the sgn function once for each application of $D_{ov}^\dagger D_{ov}$. Note this is a valid procedure for our auxiliary system (3.65) even though $D_{ov}^\dagger s$ is not chiral. This is because of the property

$$D_{ov}^\dagger D_{ov} = \gamma_5 D_{ov} D_{ov}^\dagger \gamma_5 = D_{ov} D_{ov}^\dagger, \tag{3.68}$$

so D_{ov} commutes with its hermitian conjugate and for each application of $D_{ov}^\dagger D_{ov}$ we have

$$(D_{ov}^\dagger D_{ov}) D_{ov}^\dagger s = D_{ov}^\dagger (D_{ov}^\dagger D_{ov}) s, \tag{3.69}$$

so the whole Krylov space commutes with $D_{ov}^\dagger$. We can therefore solve on the chiral source s then simply multiply the solution by $D_{ov}^\dagger$.

[2]See Appendix 10.1.

Although this chiral source trick saves a factor of two in our inversions, and multi-shift techniques can be used to form propagators for multiple masses using the same outer Krylov space [25], this nested Conjugate gradient procedure makes the the inversion procedure extraordinarily costly compared to previous methods.

3.5 Monte Carlo methods

The expectation value of any observable $\mathcal{O}$ we wish to measure is given by

$$\langle \mathcal{O} \rangle = \frac{1}{Z} \int \mathcal{D}\mathcal{U}\mathcal{D}\bar{\psi}\mathcal{D}\psi \mathcal{O} e^{-S_{QCD}}, \tag{3.70}$$

where Z is given by (3.4). As S_{QCD} is bilinear in the fermion fields, the fermion integrations can always be carried out analytically [16],[26] so the expectation value can always be written in the form

$$\langle \mathcal{O} \rangle = \frac{\int \mathcal{D}\mathcal{U} \mathcal{O}[U] e^{-S_{EFF}[U]}}{\int \mathcal{D}\mathcal{U} e^{-S_{EFF}[U]}}, \tag{3.71}$$

where now the integration is only over gauge degrees of freedom. There are still however far too many degrees of freedom to carry out this integral analytically. Instead we seek to create a representative sample of configurations which has the same distribution as the complete phase space (namely $e^{-S[U]}$). If we generate such a sample then we can approximate the expectation value by

$$\langle \mathcal{O} \rangle \approx \frac{1}{N} \sum_{i=1}^{N} \mathcal{O}[U_i], \tag{3.72}$$

where the U_i are configurations of a sample of size N. By increasing the sample size N, this approximation can be made arbitrarily good as the error is proportional to $\frac{1}{\sqrt{N}}$.

We generate this sample by a Markov process (see for example [27]). Here we start with some initial configuration U_i, then through some stochastic process update the configuration to form a new configuration U_f with probability $P(U_i \to U_f)$, such that the probability of getting U_f depends on U_i, but is independent of all previous configurations. There are many different algorithms for carrying out these stochastic updates. For pure gauge theories, configurations are generally generated through a mixture of overrelaxation and Metropolis algorithms [28, 29]. When simulating dynamical fermions, the standard algorithm is Hybrid Monte-Carlo [30].

3.6 Quenched approximation

As mentioned in the previous section the fermionic contribution to the path integral can be computed analytically. In fact the contribution is given by

$$Z_{ferm} = \int \mathcal{D}\bar{\psi}\mathcal{D}\psi e^{-\bar{\psi}K\psi} = \det K, \tag{3.73}$$

where K is our Dirac operator. However due to the huge cost of evaluating the fermion determinant we cannot at present generate gauge configurations with overlap fermions in any reasonable amount of time. We are forced therefore to work in an approximation known as the quenched approximation. In this approximation we set the fermion determinant $\det K$ equal to a constant. This avoids the huge cost of evaluating it. Physically this is equivalent to removing virtual (internal) quark loops from the vacuum (Figure 3.5). This can be seen most easily from the Wilson formulation. Equation (3.38) can

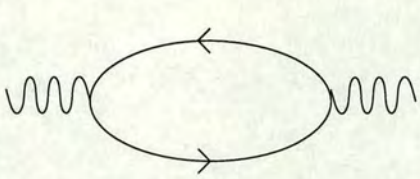

Figure 3.5: Vacuum polarizations forbidden in the quenched approximation.

be rewritten as

$$S_F^W = \frac{1}{2\kappa} \sum_{n,l} \bar{\psi}(n) \tilde{K}(n,l) \psi(l), \tag{3.74}$$

where the hopping parameter κ is given by

$$\kappa = \frac{1}{8r + 2m}, \tag{3.75}$$

and the reparameterized fermion matrix $\tilde{K}$ is

$$\begin{aligned} \tilde{K}(n,l) &= \delta_{l,n} + \kappa \sum_{\mu} [(r - \gamma_\mu) U_\mu(n) \delta_{l,n+\hat{\mu}} + (r + \gamma_\mu) U_\mu^\dagger(n - \hat{\mu}) \delta_{l,n-\hat{\mu}}] \\ &= \delta_{l,n} + \kappa M[U]_{l,n}. \end{aligned} \tag{3.76}$$

We have separated the fermion matrix into a constant local piece, and a non-local interacting term which depends on the gauge fields. It's clear now that setting det K equal to a constant is equivalent to setting $\kappa = 0$. This corresponds to the sea quark mass becoming infinite, and so there can be no vacuum polarization effects, such as those shown in Figure (3.5).

While this may seem pretty drastic, quenched QCD does exhibit many of the features of full QCD such as spontaneous chiral symmetry breaking [31], confinement and asymptotic freedom [32, 33]. However the gauge configurations have been reweighted. As we don't know the true QCD weighting det K, this is an uncontrolled approximation. Also the deviation from QCD

will presumably get worse as $m_q \to 0$, as vacuum polarization effects will become more important. We also have the problem that our signals become polluted with unphysical zero-modes which would not occur in QCD (as det K = 0). In spite of these problems, quenched QCD is in general considered to be a reasonable approximation until sufficient computer power is available to simulate dynamical overlap fermions.

3.7 Lüscher-Weisz gauge action

By removing dynamical fermions from the vacuum, we are only propagating through pure gauge backgrounds. The standard gauge action is given as before by

$$S_F = \beta \sum_{plaq} \frac{1}{3} \text{ Re Tr } [1 - U_{plaq}]. \tag{3.77}$$

While this gives the correct continuum limit, we arrived at this expression by making an expansion of the continuum gauge action in powers of the lattice spacing a, and then discarded terms of $O(a^2)$ and higher, hence the Wilson gauge action (3.77) will have $O(a^2)$ errors. However we can add higher order terms to this action to make an improved action which will cancel these $O(a^2)$ errors and be closer to the continuum theory when we are working at non-zero lattice spacing. This will give smoother configurations which hopefully should increase the locality of the fermion operator, and greatly reduce the condition number of the fermion inversions.

The Wilson gauge action (3.77) is composed of four link loops, which are the smallest loops we can make on the lattice. The next simplest terms we could add to the action to cancel the $O(a^2)$ errors are six link loops. There

are 3 topologically distinct six link loops : rectangles, bent rectangles, and parallelograms (Figure 3.6) Lüscher and Weisz [34] showed that in fact only

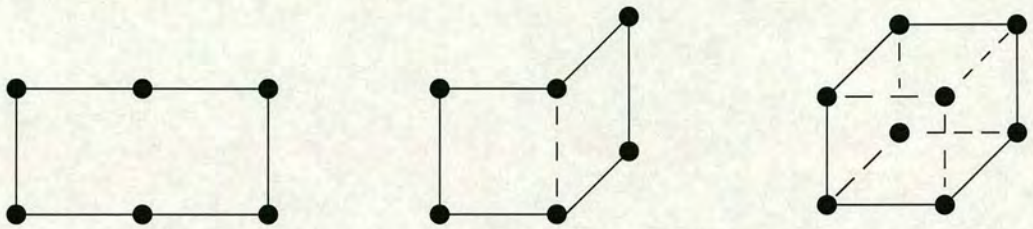

Figure 3.6: Six link loops.

two of these terms are needed to cancel $O(a^2)$ errors. This of course leads to constraints on the relative weightings of the two remaining terms, but still leaves a one parameter family of solutions. The coefficients can be calculated in lattice perturbation theory.

This improvement is however only a classical improvement of the action. Further improvement can be made by considering quantum effects. In particular, the gauge action was designed so that in the limit as $a \to 0$ we recovered the continuum gauge action. This is based on the expansion

$$U_\mu(x) \equiv e^{iagA_\mu} = 1 + iagA_\mu(x) - \frac{a^2g^2}{2}A_\mu^2(x) + \dots . \tag{3.78}$$

While naively it seems that the $O(a^2)$ term will be suppressed as we head towards the continuum limit, Lepage and Mackenzie [35] showed that the contraction of the A_μ's leads to divergences coming from tadpole diagrams which are order $\frac{1}{a^2}$. So this term is suppressed only by powers of g and not a. To factor out these tadpole diagrams they use the fact that in the continuum, the expectation value of the $1 + iagA_\mu(x)$ is 1, whereas in the

lattice theory the tadpole contributions cause it to be much smaller. Hence the average value of the link variables is a measure of the tadpole pollution, and we can remove this by simply rescaling the link variables contained in lattice operators by

$$U_\mu(x) \to \frac{U_\mu(x)}{u_0}, \tag{3.79}$$

where the mean value of the links u_0 can be approximated in a gauge invariant way by

$$u_0 = \left(\frac{1}{3}\text{Re Tr}\langle U_{plaq}\rangle\right)^{1/4}. \tag{3.80}$$

This tadpole improvement should help the lattice operators be more "continuum like" and has the advantage that it is a relatively cheap non-perturbative improvement.

The tadpole improved coefficients have been calculated to one loop in perturbation theory [36] and the results are given below. The action is thus given by

$$\begin{aligned} S_G^{LW} &= \beta_1 \sum_{pl} \frac{1}{3} \text{Re Tr}\left[1 - U_{plaq}\right] + \beta_2 \sum_{rt} \frac{1}{3} \text{Re Tr}\left[1 - U_{rect}\right] \\ &+ \beta_3 \sum_{pg} \frac{1}{3} \text{Re Tr}\left[1 - U_{parl}\right], \end{aligned} \tag{3.81}$$

where

$$\begin{aligned} \beta_2 &= -\frac{\beta_1}{20u_0^2}[1 + 0.4805\alpha] \\ \beta_3 &= -\frac{\beta_1}{u_0^2} 0.03325\alpha \\ \alpha &= -\frac{ln\left(u_0^4\right)}{3.06839}. \end{aligned}$$

β_1 remains as an overall scale factor.

This is the (tadpole improved) Lüscher-Weisz gauge action, and it is this action which has been used to generate the gauge configurations for the Monte-Carlo simulations.

3.8 Continuum and chiral extrapolations

Our Monte-Carlo simulations are carried out at fixed lattice spacing, and at quark masses above the physical quark masses. In order to make contact with experimentally measured quantities we must extrapolate our data. In order to do this we generate data at several lattice spacings and several masses and form continuum ($a \to 0$) and chiral ($m \to m_u/m_d$) extrapolations.

We can extrapolate from heavy quark masses down to physical quark masses using chiral perturbation theory [37, 38] (or for quenched simulations, quenched chiral perturbation theory [39, 40]). As chiral perturbation theory is formulated in the continuum, strictly speaking we should first take the continuum limit and then the chiral limit. However for most data sets this is not really practical, and in practice one usually first takes the chiral limit, then the continuum limit.

In general there is no guarantee this should work, and there is evidence that for theories that don't possess chiral symmetry that these two limits don't commute [41, 42]. However in the case of Ginsparg-Wilson fermions, we have chiral symmetry at fixed lattice spacing. Hence we would expect that chiral perturbation theory should still work away from the continuum limit, and that these two limits should commute. This appears to be the case [42].

Chapter 4

Two point correlation functions

Hadron masses and decay constants can be measured from two point correlation functions. These correlation functions take the form

$$C_{\mathcal{O}_1\mathcal{O}_2}(t;\vec{p}) = \langle \mathcal{O}_1(t;\vec{p})\mathcal{O}_2^\dagger(0;\vec{p})\rangle, \tag{4.1}$$

where the operators $\mathcal{O}_i$ are formed from products of quark and antiquark fields, and the angle brackets denote a path integral of the form of equation (3.3). The fermion fields can be integrated out by performing all possible Wick contractions. The correlation functions can then be written in terms of products of quark propagators which we can calculate on the lattice. The remaining integration over gauge degrees of freedom is done by then averaging over gauge configurations in the usual way. The various operators which are used, and the methods for extracting physical information from these correlations functions will be detailed in this section.

4.1 Meson correlation functions

In order to study hadron spectroscopy, we must first find a set of operators which we can use to create and destroy these particles. The form of these operators will be guided not only by the quantum numbers of the state we are looking at, but also by the physical observables we are trying to obtain. Mesons are quark-antiquark states and so it is natural to make operators which are bilinear in the quark and antiquark fields. We must also make sure the operator has the same J^{PC} numbers as the meson we wish to study. For example, the π^- state has J^{PC} values of 0^{-+}. Hence we are looking for an operator which transforms as a scalar under spatial rotations, negatively under parity, and positively under charge conjugation. Two such operators which would suffice would be the pseudoscalar $\bar{u}\gamma_5 d$ and the axial vector $\bar{u}\gamma_4\gamma_5 d$. The J^{PC} numbers of some relevant flavour non-singlet bilinears are given in Table 4.1. The positively charged versions can be found by simply exchanging u and d (flavour singlet operators will be discussed shortly). While we now have some idea as to the form of these operators, we still don't know how to extract a mass from these two point functions. To do this we must leave the path integral formulation for a moment, and look at the equivalent operator formalism. We can describe the propagation of a pion for example, from the point $(\vec{0}, 0)$ to the point $(\vec{x}, t)$ by the following matrix element

$$\langle 0|\mathbf{O}_\pi(\vec{x}, t)\mathbf{O}_\pi^\dagger(\vec{0}, 0)|0\rangle. \tag{4.2}$$

This describes a pion being created out of the vacuum at $t = 0$, and being annihilated at time t. We can then insert a complete set of energy eigenstates

Table 4.1: Quark bilinears

State	Operators	J^{PC}	meson
Scalar	$\bar{u}d$	0^{++}	a_0^-
	$\bar{u}\gamma_4 d$	0^{+-}	none
Pseudoscalar	$\bar{u}\gamma_5 d$	0^{-+}	π^-
	$\bar{u}\gamma_4\gamma_5 d$	0^{-+}	π^-
Vector	$\bar{u}\gamma_i d$	1^{--}	ρ^-
	$\bar{u}\gamma_i\gamma_4 d$	1^{--}	ρ^-
Axial	$\bar{u}\gamma_i\gamma_5 d$	1^{++}	a_1^-
Tensor	$\bar{u}\gamma_i\gamma_j d$	1^{+-}	b_1^-

$|n\rangle$ of of the QCD Hamiltonian. These propagate (in Euclidean time) by picking up a factor $e^{-E_n t}$. The matrix element can thus be written as

$$\langle 0|\mathbf{O}_\pi(\vec{x},t)\mathbf{O}_\pi^\dagger(\vec{0},0)|0\rangle = \sum_n \frac{\langle 0|\mathbf{O}_\pi(\vec{x})|n\rangle\langle n|\mathbf{O}_\pi^\dagger(\vec{0})|0\rangle}{2E_n} e^{-E_n t}. \tag{4.3}$$

At large t, only the ground state wave function will remain due to the exponential damping factor. If we isolate the zero momentum case the energy of this state will be equal to its mass. We can do this by making a Fourier projection of the operators over $\vec{x}$. i.e. we can form a state of definite 3-momentum $\vec{p}$ by the Fourier transform

$$\mathbf{O}_\pi(t;\vec{p}) = \frac{1}{V}\sum_{\vec{x}} e^{-i\vec{p}.\vec{x}}\mathbf{O}_\pi(\vec{x},t), \tag{4.4}$$

where V is a normalization factor equal to the spatial volume. Hence setting $\vec{p}=0$ in the above expression we find that summing our operator over $\vec{x}$ will

project onto the zero momentum state where $E_n = M_n$, and so we find that for large t

$$\langle 0|\frac{1}{V}\sum_{\vec{x}} \mathbf{O}_\pi(\vec{x},t)\mathbf{O}_\pi^\dagger(\vec{0},0)|0\rangle = \frac{\langle 0|\mathbf{O}_\pi|\pi\rangle\langle\pi|\mathbf{O}_\pi^\dagger|0\rangle}{2M_\pi} e^{-M_\pi t} = A_{\mathbf{O}_\pi\mathbf{O}_\pi} e^{-M_\pi t}, \tag{4.5}$$

where $|\pi\rangle$ is the ground state pion wave function. Thus we can find the mass of the ground state by looking at the large t exponential decay of the two point function (4.5). Note (4.5) is not quite correct as we have a finite volume which is anti-periodic in time, and so we will also have a backward propagating state and the two point function is properly given by

$$\langle 0|\frac{1}{V}\sum_{\vec{x}} \mathbf{O}_\pi(\vec{x},t)\mathbf{O}_\pi^\dagger(\vec{0},0)|0\rangle = A_{\mathbf{O}_\pi\mathbf{O}_\pi}[e^{-M_\pi t} + \tau_1\tau_2 e^{-M_\pi(T-t)}], \tag{4.6}$$

where T is the time extent of the lattice and τ_1, τ_2 are factors determined by how the operators act under time reversal $t \to T - t$. For two pseudoscalar pion operators which transform negatively under time reversal, we have $\tau_1 = \tau_2 = -1$.

If we return to the path integral formalism, we can now write down a general meson operator

$$M_\Gamma(t;\vec{p}) = \frac{1}{\sqrt{V}} \sum_{\vec{x},f_1,f_2} c_{f_1f_2} e^{-i\vec{p}.\vec{x}} \overline{\psi}^{f_1}(\vec{x},t)\Gamma\psi^{f_2}(\vec{x},t), \tag{4.7}$$

where we are summing over all spatial sites and quark flavours, with coefficients c_{f1f2}, and Γ is an arbitrary spin matrix (e.g for $\overline{u}\gamma_5 d$, $\Gamma = \gamma_5$ and $c_{ud} = 1$ with all other coefficients zero).

The source operator is then

$$M_\Gamma^\dagger(t;\vec{p}) = \frac{1}{\sqrt{V}} \sum_{\vec{x},f_1,f_2} c^*_{f_1f_2} e^{i\vec{p}.\vec{x}} \overline{\psi}^{f_2}(\vec{x},t)\gamma_4\Gamma^\dagger\gamma_4\psi^{f_1}(\vec{x},t). \tag{4.8}$$

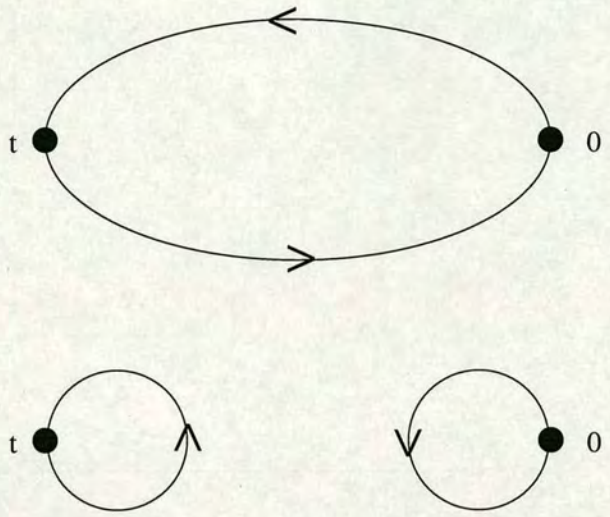

Figure 4.1: Connected and disconnected diagrams contributing to meson two point functions.

If we form the correlation function given in (4.1), we have an integral over four fermion fields. We can integrate out the fermions by forming all possible Wick contractions and our correlation function will then be given in terms of products of quark propagators. If we have states which are flavour non-singlets, then there will be only one possible combination of Wick contractions which will produce a connected diagram. If however we have degenerate flavours then there will be two possible Wick contractions, one connected, and one disconnected (see Figure 4.1). The result is then

$$
\begin{aligned}
& C_{\Gamma_1\Gamma_2}(t;\vec{p}) = \langle M_{\Gamma_1}(t;\vec{p}) M^{\dagger}_{\Gamma_2}(0;\vec{p})\rangle \qquad (4.9)\\
= \; & -\frac{1}{V}\sum_{\vec{x},\vec{y},f_1,f_2} |c_{f_1 f_2}|^2 e^{-i\vec{p}.(\vec{x}-\vec{y})} \\
\times \; & \{\langle Tr_{SC}[G^{(f_2)}(\vec{x},t;\vec{y},0)\gamma_4\Gamma_2^{\dagger}\gamma_4 G^{(f_1)}(\vec{y},0;\vec{x},t)\Gamma_1]\rangle_U
\end{aligned}
$$

$$- \delta_{f_1,f_2}\langle Tr_{SC}[G^{(f_1)}(\vec{x},t;\vec{x},t)\Gamma_1]Tr_{SC}[G^{(f_2)}(\vec{y},0;\vec{y},0)\gamma_4\Gamma_2^\dagger\gamma_4]\rangle_U\},$$

where the trace is over spin and colour, and the angle brackets here denote integration only over U. The terms G in the above expression are quark propagators defined by

$$G_{\alpha\beta}^{(f)ab}(x,y) = \langle\psi_\alpha^a(x)\bar{\psi}_\beta^b(y)\rangle_{\psi\bar{\psi}}, \tag{4.10}$$

where α and β are spin indices, a and b are colour indices, and the integration is here over all fermion degrees of freedom. The propagator is as stated in Section 3.1.2, given by the inverse of the fermion matrix. This matrix is dependent on the gauge fields and so must be inverted configuration by configuration. Note it is also dependent on the quark fields since the propagator will be mass dependent. The disconnected piece of (4.9) is very costly as it involves calculating a point to point propagator for every point on a particular time slice, each requiring an inversion the Dirac operator. Due to the immense cost of performing these inversions this is simply unfeasible, and so we will only consider flavour non-singlet quantities where the disconnected term does not occur.

For the connected piece we need two point to all propagators : one for the quark, and one for the antiquark. However we can make the problem simpler. We can use translational invariance to move all our sources y to the origin. This is perfectly legitimate as we are averaging over background configurations and so one point is as good as any other. Also we have the property

$$G^\dagger = \gamma_5 G \gamma_5, \tag{4.11}$$

since if D_{ov} obeys this property, so must its inverse. Hence we can rewrite

(4.9) for flavour non-singlet mesons as

$$C_{\Gamma_1\Gamma_2}(t;\vec{p}) = -\sum_{\vec{x},f_1,f_2} |c_{f_1f_2}|^2 e^{-i\vec{p}.\vec{x}} \times \{\langle Tr_{SC}[G^{(f_2)}(\vec{x},t;\vec{0},0)\gamma_4\Gamma_2^\dagger\gamma_4\gamma_5 G^{*(f_1)}(\vec{x},t;\vec{0},0)\gamma_5\Gamma_1]\rangle_U. \quad (4.12)$$

This is useful as now the correlation function is written in terms of a single propagator, and so we only need to perform one inversion (per fermion field) on each configuration.

4.2 Baryon correlation functions

For baryons we must again find operators with the same quantum numbers as the states we are interested in. Baryons are three quark states and so must contain three fermion fields, however the nucleon has $J^P = \frac{1}{2}^+$ and so the nucleon operator must have only one free Dirac index. This can be achieved by contracted two of the fermion fields with a product of gamma matrices to form a di-quark structure. As baryons must be colour singlets, the operator must also be totally antisymmetric under colour, which is achieved by contracting the colour indices with ϵ_{abc} as in (2.6). A suitable proton operator is then given by [43, 44]

$$B_\alpha(t;\vec{p}) = \frac{1}{\sqrt{V}}\sum_{\vec{x}} e^{-i\vec{p}.\vec{x}}\epsilon_{abc}u_\alpha^a(\vec{x},t)[u^b(\vec{x},t)C\gamma_5 d^c(\vec{x},t)], \quad (4.13)$$

where C is the charge conjugation matrix[1]. The particular gamma matrix product $C\gamma_5$ is chosen to ensure that the operator has the correct transformation properties under charge conjugation and parity. The neutron operator

[1] see Appendix 10.1.

can be obtained by the exchange $u \leftrightarrow d$. The anti-baryon is given by

$$\bar{B}_\alpha(t;\vec{p}) = \frac{1}{\sqrt{V}} \sum_{\vec{x}} e^{i\vec{p}.\vec{x}} \epsilon_{abc} [\bar{d}^c(\vec{x},t) C\gamma_5 \bar{u}^b(\vec{x},t)] \bar{u}^a_\alpha(\vec{x},t). \tag{4.14}$$

Two point correlations are then formed as before

$$C_\Gamma(t;\vec{p}) = \Gamma_{\beta\alpha} \langle B_\alpha(t;\vec{p}) \bar{B}_\alpha(0;\vec{p}) \rangle, \tag{4.15}$$

where we have introduced an arbitrary Dirac projection operator Γ. The reason for this matrix is that fermion fields contain both positive and negative parity components. This means that the operator (4.13) will have an overlap not only with the nucleon, but also its $J^P = \frac{1}{2}^-$ parity partner. Since we are only interested in the nucleon state, we can project out the positive parity part of the correlation function by using a parity projection, which for unpolarized nucleons is given by $\Gamma_{unpol} = \frac{1}{2}(1+\gamma_4)$. For polarized nucleons (at rest), a spin projector along an arbitrary axis $\vec{n}$ is given by $\frac{1}{2}(1+i\sigma\gamma_5\vec{\gamma}.\vec{n})$, where $\sigma = \pm 1$ picks out the spin up or down states along the polarization axis. We have then our general polarized projector

$$\Gamma_{pol}(\sigma) = \frac{1}{2}(1+\gamma_4)\frac{1}{2}(1+i\sigma\gamma_5\vec{\gamma}.\vec{n}). \tag{4.16}$$

After performing the fermion integration we have

$$\begin{aligned} C_\Gamma(t;p) = & \sum_{\vec{x}} e^{i\vec{p}.\vec{x}} \epsilon_{abc}\epsilon_{a'b'c'} \\ & \times \{ \langle Tr_S[\Gamma G^{(u)aa'}(\vec{x},t;\vec{0},0)] Tr_S[G^{(u)bb'}(\vec{x},t;\vec{0},0)\tilde{G}^{(d)cc'}(\vec{x},t;\vec{0},0)] \\ & + Tr_S[\Gamma G^{(u)aa'}(\vec{x},t;\vec{0},0)\tilde{G}^{(d)cc'}(\vec{x},t;\vec{0},0) G^{(u)bb'}(\vec{x},t;\vec{0},0)] \rangle_U \}, \end{aligned} \tag{4.17}$$

where Tr_S is a trace over Dirac indices. $\tilde{G}$ is defined as

$$\tilde{G} = (C\gamma_5 G C\gamma_5)^{T_S}, \tag{4.18}$$

with T_S meaning transposed in Dirac space. Note in contrast to the meson case, there are no disconnected terms in the baryon two point functions. However as before, the correlation function can be calculated on each gauge configuration from only one propagator inversion per fermion flavour.

4.3 Overlap improvements

The hadron operators we have written down have the same quantum numbers and transformation properties as the states we are interested in, but are localised point objects. As hadrons are spatially extended objects this may result in a very small overlap with the hadron wavefunction and thus a poor signal. Ideally we would like to simply measure the true hadron wavefunction, but since we don't know what that looks like, we must take the operators we have and find ways to improve our signal.

We implement two operator improvements which we will detail in this section. Firstly we smear our hadron operators at both sink and source. This takes our point operator and spreads it out over a time slice and so makes the operator look more like a hadron. Secondly, we project the wavefunction onto a non-relativistic wavefunction. This non-relativistic projection has computational benefits as well as hopefully improving the overlap.

4.3.1 Jacobi Smearing

The basic idea behind smearing a state operator is to try make a point operator have some non-zero spatial extent which will hopefully have a greater overlap with the state in question. There are a variety of different smearing

techniques available, all of which yield very similar results [45]. This is to be expected as the smearing should only alter the operator in a reasonable small area surrounding the source (otherwise our operator would no longer be local), and so should not effect the long distance physics.

In this thesis we use Jacobi smearing [46]. Here a smeared source s is defined from the original point source s_0 by

$$\sum_{\vec{x}'} K(\vec{x},t;\vec{x}',t)s(\vec{x}',t) = s_0(\vec{x},t), \tag{4.19}$$

where the smearing matrix K is given by

$$K = 1 - \kappa_s D_s. \tag{4.20}$$

κ_s is a smearing parameter and D_s is a covariant derivative on a timeslice

$$D_{s\alpha\beta}(\vec{x},t;\vec{y},t) = \delta_{\alpha\beta}\sum_{i=1}^{3}[U_i(\vec{x},t)\delta_{\vec{x}+\vec{i},\vec{y}} + U_i^\dagger(\vec{x}-\vec{i},t)\delta_{\vec{x}-\vec{i},\vec{y}}]. \tag{4.21}$$

Clearly to find our smeared source s we require the matrix K^{-1}. Instead of inverting this matrix explicitly, we perform N_s iterations of the Jacobi algorithm[2]. The nth source in the iterative sequence is given by

$$s^{(n)} = s_0 + \kappa_s D_s s^{(n-1)}, \tag{4.22}$$

with the obvious initial condition $s^{(0)} = s_0$.

We thus increase the size of the operator by hitting it successively with D_s. The operator should increase in size in the manner of a random walk where N_s is the number of steps, and κ_s is roughly analogous to the step size.

[2]See for example [47].

An effective rms radius r for the operator centred at $(\vec{x}_0, t_0)$ can be defined as [46]

$$r^2 = \sum_{\vec{x}} \frac{(\vec{x} - \vec{x}_0)^2 |s(\vec{x}, t_0)|^2}{|s(\vec{x}, t_0)|^2}. \tag{4.23}$$

We choose the values $\kappa_s = 0.21$ and $N_s = 50$. This gives our source a radius in lattice units of approximately $r = 3.5$ [48], which for the ensembles used here will make our operator roughly half the size of the physical nucleon.

Smeared propagators are then found by smearing the point source and then inverting D_{ov} on the smeared source. This will give a smeared to local propagator. To get a totally smeared propagator we must smear the resulting propagator on each time slice.

Finally it should be noted that the operator D_s is diagonal in spin space, and so the chiral source trick of Section 3.4 is unaffected by this smearing.

4.3.2 Non-relativistic projection

When we formed the baryon two point function (4.15) we used the matrix Γ to project out the positive parity part of the two point function. As each term in the correlation function is made up from combinations of the six quark and antiquark fields, this will still contain positive and negative parity quark field components, so long as they add up to give total positive parity. We can go one step further than this and project out the positive parity components of each quark field. To do this we project each of the quark fields

$$q \to \frac{1}{2}(1 + \gamma_4)q, \qquad \bar{q} \to \bar{q}\frac{1}{2}(1 + \gamma_4). \tag{4.24}$$

This projection is equivalent to using the proton wavefunction

$$B_\alpha^{NR}(t;\vec{p}) = \frac{1}{\sqrt{V}}\sum_{\vec{x}} e^{-i\vec{p}.\vec{x}}\epsilon_{abc}u_\alpha^a(\vec{x},t)[u^b(\vec{x},t)C\gamma_5\frac{1}{2}(1+\gamma_4)d^c(\vec{x},t)], \quad (4.25)$$

where we have made the substitution $C\gamma_5 \rightarrow C\gamma_5\frac{1}{2}(1+\gamma_4)$ in (4.13). A similar substitution is made in the anti-proton to give

$$\bar{B}_\alpha(t;\vec{p}) = \frac{1}{\sqrt{V}}\sum_{\vec{x}} e^{i\vec{p}.\vec{x}}\epsilon_{abc}[\bar{d}^c(\vec{x},t)\frac{1}{2}(1+\gamma_4)C\gamma_5\bar{u}^b(\vec{x},t)]\bar{u}_\alpha^a(\vec{x},t). \quad (4.26)$$

These new proton wavefunctions have exactly the same quantum numbers and transformation properties as the previous baryon operators and so are valid proton operators. This wavefunction is the same proton wavefunction [49] as predicted by the $SU(6)$ flavour/spin symmetry model (see for example [50]). In this model light quark (u,d,s) flavour symmetry $SU(3)_f$ and $SU(2)$ spin symmetry are embedded into $SU(6)$ flavour/spin supermultiplets. This model predicts the ground state octet and decuplet and has made many successful predictions. For example the ratio of the proton and nucleon magnetic moments which in this model is -1.5, compared to the experimental value of -1.46 [50]. It is therefore reasonable to believe this wavefunction is close to the true proton wavefunction. It should be noted though that as spin is a space-time symmetry and flavour is not, this unified symmetry cannot be relativistically invariant. However for slow moving valence quarks it should be a good approximation, hence the designation as a non-relativistic projection.

A consequence of this projection is that now the baryon wavefunction has two pieces: a $C\gamma_5$ piece and a $C\gamma_5\gamma_4$ piece. In the forward region $0 \leq t \leq \frac{T}{2}$, these two pieces add, however they have opposite behaviour under time reversal, and so will subtract in the region $\frac{T}{2} \leq t \leq T$. This leads to a

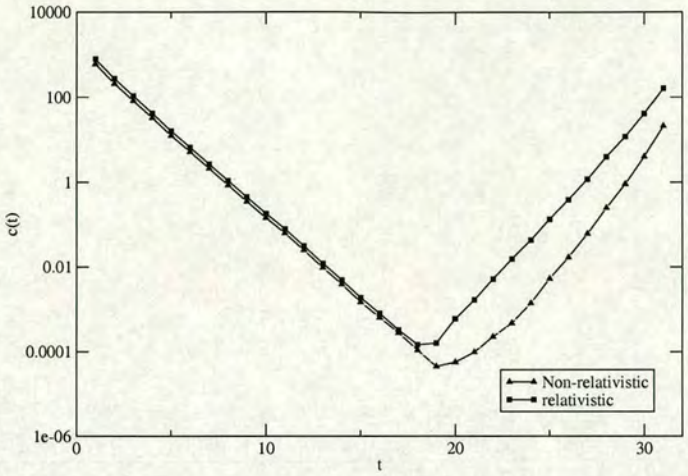

Figure 4.2: Two point proton correlation functions for both relativistic and non relativistic operators.

suppression of the backward signal and increases the length of the e^{-Mt} arm giving a slightly longer fit range (see Figure 4.2). This projection also has computational benefits when we come to form matrix elements which will be discussed in the next chapter.

Lastly we note that while this procedure can also be used for positive parity mesons such as the a_0 state, it must be modified in the case of negative parity meson states. The ground state vector and pseudoscalar mesons are negative parity and made of an even number of quark and antiquark fields, hence they must couple both positive and negative parts together. We therefore cannot project out one parity state from all the fields of these meson operators without killing the state. The projection must therefore be modified in this case to project out one parity state from the quark fields and the opposite parity state from the antiquark fields.

4.4 Meson decay constants

The decay constants introduced in Section 2.2 can be determined from combinations of two point functions containing local(L) and smeared(S) operators. The source operator represents a spatially extended hadronic state and so is smeared to increase its overlap with the hadron. However the sink operator is part of a weak current. It represents a point-like gauge boson, so must remain local. Define for example the correlation function $C^{LS}_{O_1O_2}(t)$. This has the smeared operator $O_2^\dagger$ at source (time 0), and local operator O_1 at sink (time t).

By transforming (2.11), (2.12) to Euclidean space and taking the case of zero-momentum we can define the pseudoscalar and vector meson decay constants by

$$\begin{aligned} \langle 0|\mathbf{A}_4|\pi\rangle &= \sqrt{2}\, m_\pi f_\pi \\ \langle 0|\mathbf{V}_i|\rho,\lambda\rangle &= e(\lambda)_i \frac{m_\rho^2}{f_\rho}, \end{aligned} \tag{4.27}$$

where $e(\lambda)_i$ is the polarization vector. V and A are the vector and axial currents

$$\begin{aligned} V_\mu &= \bar{\psi}\gamma_\mu\psi \\ A_\mu &= \bar{\psi}\gamma_\mu\gamma_5\psi. \end{aligned} \tag{4.28}$$

The matrix element for f_π can be computed from the correlation functions $C^{LS}_{A_4P}(t)$ and $C^{SS}_{PP}(t)$, where P is the pseudoscalar. By comparison with (4.5) we have

$$\langle 0|\mathbf{A}_4|\pi\rangle = \frac{\sqrt{2m_\pi}A^{LS}_{A_4P}}{\sqrt{A^{SS}_{PP}}}. \tag{4.29}$$

Similarly, for f_ρ we have

$$\langle 0|\mathbf{V}_i|\rho,\lambda\rangle = e(\lambda)_i \frac{\sqrt{2m_\rho}\sum_k A^{LS}_{V_k V_k}}{\sqrt{3\sum_k A^{SS}_{V_k V_k}}}, \tag{4.30}$$

where we have averaged the amplitudes to increase our statistics.

Chapter 5

Three point correlation functions

While two point functions are sufficient for studying hadron masses and decay constants, in order to study nucleon matrix elements of the form $\langle \mathbf{N}|\mathcal{O}|\mathbf{N}\rangle$ we will need to study three point correlation functions. These are defined analogously to (4.15) by

$$C_\Gamma(t,\tau;\vec{p};\vec{q};\mathcal{O}) = \Gamma_{\beta\alpha}\langle B_\alpha(t;\vec{p}')\mathcal{O}(\tau;\vec{q})\bar{B}_\beta(0;\vec{p})\rangle. \tag{5.1}$$

Here we have a baryon of momentum p created at time 0. There is then an operator insertion $\mathcal{O}$ at time τ which carries momentum q. The final nucleon then carries momentum $p' = p + q$ and is annihilated at time t. We again include an arbitrary projection matrix Γ. The baryon operators are defined as before. We form an operator of definite momentum q by the Fourier transform

$$\mathcal{O}(\tau,\vec{q}) = \sum_{\vec{x}} e^{i\vec{q}.\vec{x}}\mathcal{O}(\vec{x},\tau). \tag{5.2}$$

Some care is needed here as $\mathcal{O}$ need not be a local operator. For all the matrix elements examined in this thesis, $\mathcal{O}$ will be bilinear in the fermion fields, so we can define

$$\mathcal{O}(\tau,\vec{q}) = \sum_{\vec{x},v,w} e^{i\vec{q}.\vec{x}} \bar{\psi}_{\alpha}^{a(f)}(v)\mathcal{O}_{\alpha\beta}^{ab}(v,w;\vec{x},\tau)\psi_{\beta}^{b(f)}(w). \tag{5.3}$$

For local operators, $v = w = x$, however for non-local operators this is not the case, and $x \equiv (\vec{x},\tau)$ is the operator's "centre of gravity", which we take as the point of the momentum insertion.

5.1 Ratios of correlation functions

To relate matrix elements to correlation functions we must again appeal to the operator formalism . We proceed as in the two-point case and replace our field variables with the vacuum expectation value of the time ordered product of the corresponding operators. Our corresponding correlation function is then

$$C_{\Gamma}(t,\tau;\vec{p};\vec{q};\mathbf{O}) = \Gamma_{\beta\alpha}\langle 0|\mathbf{B}_{\alpha}(t;\vec{p}')\mathbf{O}(\tau;\vec{q})\bar{\mathbf{B}}_{\beta}(0;\vec{p})|0\rangle. \tag{5.4}$$

We now insert two complete sets of states. For well separated operators $t \gg \tau \gg 0$, only the ground states will remain and we have

$$\begin{aligned} C_{\Gamma}(t,\tau;\vec{p};\vec{q};\mathbf{O}) = & \\ & \frac{1}{2E_p 2E_{p'}}\Gamma_{\beta\alpha}\langle 0|\mathbf{B}_{\alpha}(t;\vec{p}')|N(\vec{p}')\rangle\langle N(\vec{p}')|\mathbf{O}(\tau;\vec{q})|N(\vec{p})\rangle\langle N(\vec{p})|\bar{\mathbf{B}}_{\beta}(0;\vec{p})|0\rangle \\ & = \frac{1}{2E_p 2E_{p'}}\Gamma_{\beta\alpha}\langle 0|\mathbf{B}_{\alpha}(\vec{p}')|N(\vec{p}')\rangle\langle N(\vec{p}')|\mathbf{O}(\vec{q})|N(\vec{p})\rangle\langle N(\vec{p})|\bar{\mathbf{B}}_{\beta}(\vec{p})|0\rangle \\ & \qquad \times e^{-E_{p'}(t-\tau)}e^{-E_p\tau}, \end{aligned} \tag{5.5}$$

where we have already integrated over the momenta of the complete sets of states. We are interested in matrix elements with $\vec{q} = 0$. In this case $p' = p$ and this expression reduces to

$$C_\Gamma(t, \tau; \vec{p}; \vec{0}; \mathbf{O}) = \frac{1}{(2E_p)^2}\Gamma_{\beta\alpha}\langle 0|\mathbf{B}_\alpha(\vec{p})|N(\vec{p})\rangle\langle N(\vec{p})|\mathbf{O}(\vec{0})|N(\vec{p})\rangle\langle N(\vec{p})|\bar{\mathbf{B}}_\beta(\vec{p})|0\rangle e^{-E_p t}. \tag{5.6}$$

By comparison with (4.3) we see that the matrix element we are interested in can be obtained by taking the ratio of the three point function with the corresponding two-point function. So we have

$$\begin{aligned} R_\Gamma(t; \tau; \vec{p}, \vec{0}; \mathcal{O}) &= \frac{C_\Gamma(t, \tau; \vec{p}; \vec{0}; \mathcal{O})}{C_\Gamma(t; \vec{p})} \\ &= \frac{1}{2E_p}\langle N(\vec{p})|\mathbf{O}(\vec{0})|N(\vec{p})\rangle. \end{aligned} \tag{5.7}$$

Note the time dependence has cancelled out here and we thus expect this ratio to be constant. However the above argument was based on the fact we have well separated operators and only the groundstate contributes, so in practice we look for a plateau region between the source and sink.

5.2 Connected diagrams

While the baryon two point function is completely connected, the three point functions have both connected and disconnected pieces (see Figure 5.1). If we look at the proton three point function with $\vec{q} = 0$, and for the moment consider just the connected terms, after integrating out the fermion fields we can arrange the terms [51] as

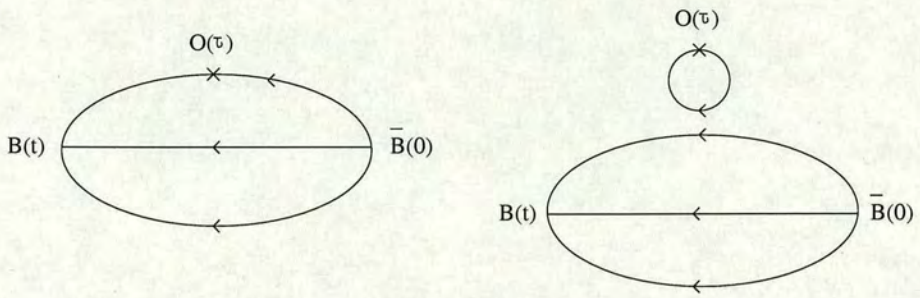

Figure 5.1: Connected and disconnected diagrams contributing to the baryon 3pt function.

$$C_\Gamma(t,\tau;\vec{p};\mathcal{O}) = -\sum_{\vec{y},v,w} \langle Tr_{SC}[\Sigma_\Gamma^{(f)}(\vec{0},0;\vec{p},t;v)\mathcal{O}(v,w;\vec{y},\tau)G^{(f)}(w;\vec{0},0)]\rangle_U, \tag{5.8}$$

where the generalised propagator $\Sigma_\Gamma^{(f)}(\vec{0},0;\vec{p},t;v)$ can be written as

$$\Sigma_\Gamma^{(f)}(\vec{0},0;\vec{p},t;v) = \sum_{\vec{x}} S_\Gamma^{(f)}(\vec{x},t;\vec{0},0;\vec{p})G^{(f)}(\vec{x},t;v). \tag{5.9}$$

The generalised sources $S_\Gamma^{(f)}(\vec{x},t;\vec{0},0;\vec{p})$ differ depending on whether or not the current is inserted into a u or d quark line. For a u quark line we have

$$\begin{aligned} S_\Gamma^{(u)}(\vec{x},t;\vec{0},0;\vec{p}) = e^{-i\vec{p}.\vec{x}}\epsilon^{abc}\epsilon^{a'b'c'} \times \\ \{\tilde{G}^{(d)bb'}(\vec{x},t;\vec{0},0)G^{(u)cc'}(\vec{x},t;\vec{0},0)\Gamma \\ +Tr_S[\tilde{G}^{(d)bb'}(\vec{x},t;\vec{0},0)G^{(u)cc'}(\vec{x},t;\vec{0},0)]\Gamma \\ +\Gamma G^{(u)bb'}(\vec{x},t;\vec{0},0)\tilde{G}^{(d)cc'}(\vec{x},t;\vec{0},0) \\ +Tr_S[\Gamma G^{(u)bb'}(\vec{x},t;\vec{0},0)]\tilde{G}^{(d)cc'}(\vec{x},t;\vec{0},0)\}, \end{aligned} \tag{5.10}$$

while for the d quark line

$$S_\Gamma^{(d)}(\vec{x},t;\vec{0},0;\vec{p}) = e^{-i\vec{p}.\vec{x}}\epsilon^{abc}\epsilon^{a'b'c'} \times \{\tilde{G}^{(u)bb'}(\vec{x},t;\vec{0},0)\tilde{\Gamma}\tilde{G}^{(u)cc'}(\vec{x},t;\vec{0},0) + Tr_S[\Gamma G^{(u)bb'}(\vec{x},t;\vec{0},0)]\tilde{G}^{(u)cc'}(\vec{x},t;\vec{0},0)\} \quad , \tag{5.11}$$

where terms of the form $\tilde{X}$ are defined in (4.18).

The generalised sources S_Γ are composed of propagators of the form $G(x,0)$ which we have already calculated for the two point functions, however the second term on the right hand side of (5.9) is a propagator from all points, to all points, and so would seem to require a separate inversion for every space-time point which is obviously prohibitively expensive. However since $G(\vec{x},t;v)$ is a Green's function of D_{ov} we have from (5.9)

$$\sum_v \Sigma_\Gamma^{(f)}(\vec{0},0;\vec{p},t;v)D_{ov}(v;v') = S_\Gamma^{(f)}(\vec{v'},t;\vec{0},0;\vec{p})\delta_{v'_4 t}, \tag{5.12}$$

which on taking the transpose conjugate and using $D_{ov}^\dagger = \gamma_5 D_{ov}\gamma_5$ becomes

$$\sum_v D_{ov}(v;v')\gamma_5\Sigma_\Gamma^{(f)\dagger}(\vec{0},0;\vec{p},t;v) = \gamma_5 S_\Gamma^{(f)\dagger}(\vec{v'},t;\vec{0},0;\vec{p})\delta_{v'_4 t}. \tag{5.13}$$

This is now in the same form as (3.63), and so we can use Conjugate gradients to solve for Σ_Γ by inverting D_{ov} on the generalised source given on the right-hand side of (5.13).

Thus to find the connected three point function we first invert on our original fermion source to form a quark propagator. We then tie two of these propagators together to form the generalised sources S_Γ, and then invert of this source to form the generalised propagator Σ_Γ. We then correlate a quark

propagator, and generalised propagator and the operator insertion as shown in (5.8).

The advantage of this procedure is that once both types of propagators have been calculated, they are independent of the operator insertion, and so any number of operators can be inserted at no extra cost. However as we must form the generalised source at a particular time slice we must perform separate inversions for each sink time t. We must also form separate inversions for each nucleon momentum $\vec{p}$ and for each Γ (i.e polarized or un-polarized).

5.3 Disconnected diagrams

As well as the connected terms, we also have disconnected diagrams contributing to the baryon three-point function (Figure (5.1)). These take the form

$$\begin{aligned} C_\Gamma(t,\tau;\vec{p};\mathcal{O}) = &- \sum_{\vec{x},v,w} e^{i\vec{p}.\vec{x}} \epsilon_{abc}\epsilon_{a'b'c'} \\ &\times\langle\{Tr_S[\Gamma G^{(u)aa'}(\vec{x},t;\vec{0},0)]Tr_S[G^{(u)bb'}(\vec{x},t;\vec{0},0)\tilde{G}^{(d)cc'}(\vec{x},t;\vec{0},0)] \\ &+Tr_S[\Gamma G^{(u)aa'}(\vec{x},t;\vec{0},0)\tilde{G}^{(d)cc'}(\vec{x},t;\vec{0},0)G^{(u)bb'}(\vec{x},t;\vec{0},0)]\} \\ &\times Tr_S[\Gamma G^{(f)dd'}(w,v)\mathcal{O}^{d'd}(v,w;\vec{y},\tau)]\rangle_U, \end{aligned} \tag{5.14}$$

where f can be u or d. This is simply the baryon propagator correlated with a quark loop. The quark loop, like the meson disconnected diagram, requires a propagator from all point to all points. This again practically cannot be calculated. If we assume isospin symmetry, these terms arising from the u

and the d disconnected quark loops should be equal in magnitude as they only interact with the baryon through gluon exchange. We can then cancel out these terms if we restrict ourselves to looking at only the non-singlet parts of the three-point functions, i.e.

$$\langle N(t)\mathcal{O}^{NS}(\tau)N(0)\rangle = \langle N(t)\mathcal{O}^{u}(\tau)N(0)\rangle - \langle N(t)\mathcal{O}^{d}(\tau)N(0)\rangle. \qquad (5.15)$$

Note this cancels out any contributions from the gluonic operators (2.54) for precisely the same reason.

5.4 Non-relativistic projection

Before we perform the second stage inversion to produce the generalised propagator Σ_Γ, we can improve the source on the right-hand side of (5.9) in the same way as we did the original fermion source : namely by Jacobi smearing and using the non-relativistic projection. The second of these also has a computational benefit for the second stage inversion. If we consider the non-relativistic projection defined in (4.24), then this has the effect of transforming each quark propagator G as

$$G \to \frac{1}{2}(1+\gamma_4)G\frac{1}{2}(1+\gamma_4). \qquad (5.16)$$

If we consider an arbitrary propagator in 2×2 Dirac block diagonal form, then explicitly in the chiral basis[1] the above transformation becomes

$$\begin{pmatrix} A & B \\ C & D \end{pmatrix} \to \frac{1}{4}\begin{pmatrix} 1 & 1 \\ 1 & 1 \end{pmatrix}\begin{pmatrix} A & B \\ C & D \end{pmatrix}\begin{pmatrix} 1 & 1 \\ 1 & 1 \end{pmatrix}$$

[1]See Appendix 10.1

$$= \frac{1}{4} \begin{pmatrix} A+B+C+D & A+B+C+D \\ A+B+C+D & A+B+C+D \end{pmatrix}. \tag{5.17}$$

This transformation therefore has the effect of block averaging the propagator in Dirac space. If we now look at the form of the sources on the right-hand side of (5.13), these will all be of the form

$$\begin{pmatrix} X & X \\ -X & -X \end{pmatrix}. \tag{5.18}$$

So we find that if we invert on the first two spin components (i.e. the first column) this will give exactly the same result as the second two components. We therefore only have to calculate six spin/colour components for the second stage inversion, which obviously cuts our inversion time in half.

5.5 Lattice operators

In this section so far we have dealt with how to generate a nucleon three point function for an arbitrary operator insertion. We now want to specify exactly what operators we wish to measure.

In Section 2 we saw how moments of structure functions can be related to matrix elements of twist 2 operators. A basis for these operators is given in (2.53). However these are continuum, Minkowski space-time operators. In order to find equivalent Lattice, Euclidean space operators we must Wick rotate the operator and discretize the derivative (see Section 3.1). A further concern is that the operators given in (2.53) were chosen for their transformation properties under the Lorentz group. In particular they cannot mix with operators of the same or lower dimension. This ensures that they have

simple multiplicative renormalization coefficients [52]. When we change to Euclidean space our symmetry group changes from the Lorentz group to the orthogonal group $O(4)$. On discretization this becomes the hypercubic group $H(4) \subset O(4)$. While our continuum operators transformed under an irreducible representation of the Lorentz group, as we now have a smaller symmetry group, these operators will in general transform under a reducible representation of $H(4)$ and so mixing can occur. In order to avoid this problem we choose operators which transform under irreducible representations of $H(4)$. Bases for irreducible representations of $H(4)$ are given in [53].

Another consideration is the nucleon momentum $\vec{p}$. Larger momenta will cause noisier signals, so we wish to keep $\vec{p}$ as small as possible, and so here we choose $\vec{p} = 0$. This however does put some constraints on the operators that can be measured, as some of the matrix elements might depend on $\vec{p}$ and hence vanish for $\vec{p} = 0$.

Using zero momentum also makes the polarizations simpler. For unpolarized moments we use the projection matrix Γ_{unpol} defined in Section 4.2, while for polarized structure functions we choose operators polarized in the y direction. As the polarized structure functions are related to the difference of the spin up and spin down parton distribution functions (see Section 2.4), we use the spin projector

$$\Gamma_{pol} = \Gamma_{pol}(\sigma = +1) - \Gamma_{pol}(\sigma = -1) = \frac{1}{2}(1 + \gamma_4) i\gamma_5\gamma_2, \tag{5.19}$$

where $\Gamma_{pol}(\sigma)$ is defined in (4.16).

The lattice operators measured here, the particular moment and matrix element which they are related to, and the value of the 3pt to 2pt ratio are shown in Table 5.1. All of these operators transform under irreducible

	Operators	Moment	Ratio
$\mathcal{O}_{v_{2,b}}$	$\mathcal{O}^q_{\{44\}} - \frac{1}{3}\sum_i \mathcal{O}^q_{\{ii\}}$	$M_1(F_1) \sim v_2$	$-\frac{E_p^2+\frac{1}{3}\vec{p}^2}{E_p} v_{2,b}$
$\mathcal{O}_{a_0}$	$\mathcal{O}^{5q}_2$	$M_0(g_1) \sim a_0$	$i\frac{m_N}{E_p} a_0$
$\mathcal{O}_{a_{1,b}}$	$\mathcal{O}^{5q}_{\{24\}}$	$M_1(g_1) \sim a_1$	$-\frac{1}{2} i m_N a_{1,b}$
$\mathcal{O}_{h_{1,b}}$	$\mathcal{O}^{\sigma q}_{\{24\}}$	$M_1(h_1) \sim h_1$	$h_{1,b}$

Table 5.1: Measured lattice operators relating to moments of structure functions.

representations of $H(4)$ and so relevant operator mixing is avoided. Some operators have a b suffix. This is because these matrix elements have more than one traceless, symmetric irreducible representation [53]. For the matrix elements shown here these representations correspond to "off-diagonal" operators whose matrix elements are directly proportional to $\vec{p}$, and "diagonal" elements whose matrix elements are proportional to E_p. The off-diagonal elements conventionally have the suffix a, and since we only have zero momentum, we cannot consider them, and restrict ourselves to 'diagonal' elements with the suffix b. $M_n(f(x))$ is the nth moment of $f(x)$ defined by

$$M_n(f(x)) = \int_0^1 x^n f(x) dx. \tag{5.20}$$

5.6 Operator improvement

Any Lattice action that satisfies the Ginsparg-Wilson relation (3.45) is automatically $O(a)$ improved [54, 55]. This is due to the fact that any $O(a)$ terms in the action must be of the form of a clover term $\bar{\psi}\sigma_{\mu\nu}F_{\mu\nu}\psi$, since the $O(a)$ terms of any action can be removed by the addition of a term of this

form [56, 57]. However a term of this kind would explicitly break the on-shell chiral symmetry of (3.45), and so no term of this kind can be present, hence the action must have lattice artifacts that are at most $O(a^2)$.

This guarantees that measurements of the mass spectrum will be $O(a)$ improved, but for matrix elements we must also improve the operators. For matrix elements of an operator $\mathcal{O}$, we must consider any $O(a)$ operators $\mathcal{O}_i$ which have the same transformation properties under $H(4)$, charge conjugation and parity, as these operators can mix with $\mathcal{O}$ under renormalization, leading to $O(a)$ lattice artifacts. By taking suitable linear combinations of $\mathcal{O}$ with these additional irrelevant operators we can form an operator whose lattice artifacts will be at most $O(a^2)$. A general improved operator $\mathcal{O}^{imp}$ can be written as

$$\mathcal{O}^{imp} = \mathcal{O} + am_q c_0 \mathcal{O} + a \sum_i c_i \mathcal{O}_i, \tag{5.21}$$

with mixing coefficients c_i which will in general depend on the gauge coupling. However for GW fermions the situation is greatly simplified as all of the irrelevant operators $\mathcal{O}_i$ sit in a different chiral multiplet to $\mathcal{O}$ and hence are forbidden to mix with $\mathcal{O}$ [58]. Hence all the coefficients $c_i = 0$, and all that remains is to determine the coefficient c_0. A suitably chosen value should ensure our improved operators have a smaller quark mass dependence, although as all the quantities here will be extrapolated to the chiral limit, the final results will be independent of c_0. For on-shell matrix elements this coefficient is given by [59]

$$c_0 = \frac{\frac{1}{2\rho}}{1 - \frac{am_q}{2\rho}}, \tag{5.22}$$

which on substitution into (5.21) gives

$$\mathcal{O}^{imp} = (1 - \frac{am_q}{2\rho})^{-1}\mathcal{O}. \tag{5.23}$$

Thus for on-shell quantities, $O(a)$ improvement is achieved by a simple multiplicative factor which is independent of the operator measured.

Chapter 6

Renormalization

So far all the quantities we have discussed have been written in terms of bare quantities. While this is sufficient for calculations of the mass spectrum, matrix elements must be renormalized in order to compare our lattice results with experimentally measured, physical quantities. In this section we discuss why this procedure is needed, and how in general it is carried out. We explain how some renormalization constants can be determined non-perturbatively on the lattice through the use of Ward identities. The remaining matrix elements considered in this thesis will be renormalized using lattice perturbation theory, and we give brief outline of how these calculations are carried out, and how different renormalization scales and schemes can be related to each other.

6.1 Renormalization

The path integral (3.1) can be expressed as a perturbative series[1] in the gauge coupling, with higher order terms relating to Feynman diagrams with progressively more interactions. Many of these diagrams have divergent amplitudes and so give infinite contributions to any calculated process. This is clearly a problem as any physically measurable process should give us a finite answer. The problem is rooted in the fact that we are forming a perturbative series with the wrong parameters. The bare input parameters of the theory are shifted by the interactions, and so we must calculate these shifts and absorb them into the bare parameters to give us renormalized parameters. These renormalized parameters will then lead to finite physical results.

In general this is a two stage process. We must first find a way to render the divergent integrals finite. This process, known as "Regularization", can be achieved either by introducing a momentum cut-off, or by other means such as dimensional regularization. In this case we calculate in an arbitrary dimension d (which we will eventually analytically continue back to 4). Both of these methods introduce a new scale, μ, into the theory in order to keep the results dimensionally correct.

While we now have finite integrals, any physical result should not depend on how we regularized the integrals, (in our case what value of lattice spacing a we choose). Therefore we must redefine our bare parameters in such a way that our integrals remain finite as we remove a. We define our renormalized parameters though a set of renormalization conditions. These can for example define the physical masses and charges, or a scattering amplitude at fixed

[1] See for example [8].

momenta. A particular choice of renormalization conditions is referred to as a renormalization scheme. Whichever scheme is chosen however, the renormalization conditions are always written in terms of (in principal) physically measurable quantities, as their purpose is to fix the bare parameters to their physical counterparts. Once we have these conditions we then rescale our parameters such that the renormalization conditions hold. The renormalization conditions thus provide a set of constraints which completely determine how the bare parameters should be rescaled.

In the specific case of matrix elements calculated on the lattice, operator matrix elements (or more loosely speaking the operators) will depend on the lattice spacing a. When we come to renormalize an operator $\mathcal{O}$, the rescaling of all the parameters in the Lagrangian leads to an overall rescaling of the operator by a factor $Z_{\mathcal{O}}$, so that our renormalized operator $\mathcal{O}_R$ is given by

$$\mathcal{O}_R^S(\mu) = Z_{\mathcal{O}}^S(a\mu)\mathcal{O}(a), \tag{6.1}$$

such that our renormalized matrix element remains finite in the limit $a \to 0$. The superscript on $Z_{\mathcal{O}}^S$ denotes a particular renormalization scheme S. Thus we absorb the a dependence of the operator into the renormalization constant $Z_{\mathcal{O}}$, although we must still state our answer in terms of the renormalization scheme S and scale μ.

6.2 Non-perturbative renormalization

While the perturbative procedure described in the previous section can in principle be used to determine the renormalization constants (up to a specified order) of any operator, it is in general a very complex procedure as

the discretization of the QCD Lagrangian leads to more complicated expressions than in the continuum. It can also lead to extra diagrams which are not present in the continuum theory. However for certain operators we can exploit symmetry arguments to give us non-perturbative determinations of their renormalization constants through the use of lattice Ward identities. In the following subsections we show how these identities can be used to measure these factors on the lattice.

6.2.1 Z_V

In continuum QCD, for n_f flavours of degenerate quarks there is an exact symmetry of the Lagrangian (2.1) under the transformations

$$\begin{aligned} \psi(x) &\rightarrow e^{iT^a\alpha_a}\psi(x) \\ \bar{\psi}(x) &\rightarrow \bar{\psi}(x)e^{-iT^a\alpha_a}, \end{aligned} \tag{6.2}$$

where T^a is a generator of the the flavour symmetry group $SU(n_f)$. An equivalent flavour singlet transformation is also a symmetry. This is achieved by setting $T^a = I$. The invariance of the Lagrangian under the corresponding infinitesimal transformations (neglecting contact terms) leads to the following Ward identities for the non-singlet transformations

$$\langle \partial_\mu V_\mu^a \Omega \rangle = 0, \tag{6.3}$$

where Ω is an arbitrary functional of the fermion and gauge fields, and V_μ^a is the local vector current

$$V_\mu^a = \bar{\psi}\gamma_\mu T^a \psi. \tag{6.4}$$

An identical expression is derived for the singlet case. In the continuum, as this a conserved current it does not need to be renormalized. This is not the case for the overlap Lagrangian at finite lattice spacing due to discretization errors. As the overlap operator is non-local, so is the conserved current [60]. The local vector current is not conserved, and so if we require these identities to hold at fixed lattice spacing, the vector currents must be renormalized with a finite renormalization constant Z_V. We can measure Z_V by considering the following nucleon matrix element

$$Z_V \langle N(p)|V_\mu^{NS}|N(p)\rangle, \tag{6.5}$$

where V_μ^{NS} is the non-singlet current

$$V_\mu^{NS} = \bar{u}\gamma_\mu u - \bar{d}\gamma_\mu d. \tag{6.6}$$

The renormalized vector current simply counts the number of quarks of a given flavour and so we must have

$$Z_V \langle N(p)|V_4^{NS}|N(p)\rangle = \langle N(p)|\,(\ 2\ -\ 1\ )\,|N(p)\rangle = 2E_p, \tag{6.7}$$

and so by rearrangement we have

$$Z_V^{-1} = R(V_4^{NS}), \tag{6.8}$$

where $R(V_4^{NS})$ is the ratio of three point to two point functions described in (5.7).

6.2.2 Z_A

We proceed in a similar manner to determine the renormalization constant for the local axial current. In the continuum we have the chiral transformations

$$\psi(x) \ \rightarrow \ e^{iT^a \alpha_a \gamma_5}\psi(x)$$

$$\bar{\psi}(x) \rightarrow \bar{\psi}(x)e^{iT^a\alpha_a\gamma_5}, \tag{6.9}$$

where we again have flavour non-singlet ($T^a \in su(n_f)$), and flavour singlet ($T^a = I$) transformations, however the singlet transformation is anomalous [8].

If we consider just the non-singlet transformation, the corresponding Ward identity is

$$Z_A\langle\partial_\mu A^a_\mu\Omega\rangle = 2Z_mZ_P\langle mP^a\Omega\rangle. \tag{6.10}$$

Here A^a_μ and P^a are respectively the local axial and pseudoscalar currents

$$A^a_\mu = \bar{\psi}\gamma_\mu\gamma_5T^a\psi, \qquad P = \bar{\psi}\gamma_5T^a\psi, \tag{6.11}$$

m is the bare quark mass, and Z_A, Z_P, Z_m are their corresponding renormalization constants. Again Ω is an arbitrary functional.

While it seems we now have three renormalization constants, in the continuum we can remove two of these. Firstly if we consider the mass terms in the action, for two flavours (the argument is virtually identical for arbitrary N_f) we have terms

$$m_u\bar{u}u + m_d\bar{d}d. \tag{6.12}$$

These can be separated into singlet and non-singlet parts as

$$\frac{1}{2}(m_u + m_d)(\bar{u}u + \bar{d}d) + \frac{1}{2}(m_u - m_d)(\bar{u}u - \bar{d}d) \tag{6.13}$$

As each of these terms must be renormalization group invariant we have $Z_m^{-1} = Z_S$, where Z_m is the non-singlet $(m_u - m_d)$ mass renormalization and S^a is the non-singlet scalar current

$$S^a = \bar{\psi}T^a\psi. \tag{6.14}$$

Further, if we apply a infinitesimal chiral transformation

$$\delta\psi = i\alpha_b T^b \gamma_5 \psi, \qquad \delta\bar{\psi} = \bar{\psi} i T^b \alpha_b \gamma_5, \tag{6.15}$$

to the scalar and pseudoscalar currents we have

$$\delta S^a = -i f_{abc} \alpha_b P^c, \qquad \delta P^a = -i f_{abc} \alpha_b S^c \tag{6.16}$$

Hence S and P transform as a doublet, and therefore we must have $Z_P = Z_S$. We can now substitute these results into (6.10). If we choose Ω to be a pion operator we can determine Z_A from

$$Z_A = \frac{2m\langle 0|P|\pi\rangle}{\langle 0|\partial_\mu A_\mu|\pi\rangle}. \tag{6.17}$$

Note this is only useful in our lattice simulation if we can show that these renormalization constants also cancel away from the continuum.

6.2.3 Local currents at finite lattice spacing

At non-zero lattice spacing we do not have the symmetry (6.2), but the weaker on-shell chiral symmetry

$$\begin{aligned} \psi(x) &\rightarrow e^{iT^a\alpha_a\gamma_5(1-\frac{1}{2}a\not{\mathcal{P}})}\psi(x) \\ \bar{\psi}(x) &\rightarrow \bar{\psi}(x)e^{iT^a\alpha_a(1-\frac{1}{2}a\not{\mathcal{P}})\gamma_5}, \end{aligned} \tag{6.18}$$

The corresponding Ward identity is

$$Z'_A\langle\partial_\mu A'^a_\mu\Omega\rangle = 2Z_m Z'_P\langle mP'^a\Omega\rangle, \tag{6.19}$$

where A'^a_μ and P'^a are now new lattice axial and pseudoscalar currents

$$A'^a_\mu = \bar{\psi}\gamma_\mu\gamma_5(1-\frac{1}{2}a\not{\mathcal{P}})T^a\psi, \qquad P'^a = \bar{\psi}\gamma_5(1-\frac{1}{2}a\not{\mathcal{P}})T^a\psi. \tag{6.20}$$

We can similarly define lattice vector and scalar currents

$$V_\mu'^a = \bar{\psi}\gamma_\mu(1 - \frac{1}{2}a\not{\mathcal{D}})T^a\psi, \qquad S'^a = \bar{\psi}(1 - \frac{1}{2}a\not{\mathcal{D}})T^a\psi. \tag{6.21}$$

These currents are related to their local counterparts by the fact that they transform under the lattice chiral symmetry (6.18) in the same way as the local operators transform in the continuum [61]. Namely under the non-singlet transformations

$$\delta\psi_i = i\alpha_b T^b_{ij}\gamma_5(1 - \frac{1}{2}a\not{\mathcal{D}})\psi_j, \quad \delta\bar{\psi}_i = \bar{\psi}_j i T^b_{ji}\alpha_b(1 - \frac{1}{2}a\not{\mathcal{D}})\gamma_5, \tag{6.22}$$

the scalar and pseudoscalar currents transform as

$$\delta S'^a = -if_{abc}\alpha_b P'^c, \qquad \delta P'^a = -if_{abc}\alpha_b S'^c, \tag{6.23}$$

while similarly the vector and axial currents transform as

$$\delta V_\mu'^a = -if_{abc}\alpha_b A_\mu'^c, \qquad \delta A_\mu'^a = -if_{abc}\alpha_b V_\mu'^c. \tag{6.24}$$

Thus as these operators transform as a closed pairs we have

$$Z_{S'} = Z_{P'}, \qquad Z_{V'} = Z_{A'}. \tag{6.25}$$

Further, as the difference between the local and lattice operators is of the form $\bar{\psi}\Gamma\frac{1}{2}a\not{\mathcal{D}}\psi$, when we insert this operator into a three-point function, the two fermion fields will form two propagators with fields from the external states, one of which will cancel with $\not{\mathcal{D}}$. This will leave one propagator which by virtue of chiral symmetry cannot be proportional to $1/a$. Thus we have for all local operators $\mathcal{O}$ and corresponding lattice operators $\mathcal{O}'$, that (up to lattice artifacts) $Z_\mathcal{O} = Z_{\mathcal{O}'}$. Hence even at finite lattice spacing we expect

$$Z_S = Z_P, \qquad Z_V = Z_A. \tag{6.26}$$

Finally as the massive Dirac operator D_{ov} (3.59) can be written as

$$D_{ov} = (1 - \frac{1}{2}am)\not{p} + m, \tag{6.27}$$

the mass dependent terms are of the form

$$m\bar{\psi}(1 - \frac{1}{2}a\not{p})\psi, \tag{6.28}$$

and so proceeding as in the continuum case, we have that $Z_m^{-1} = Z_S$.

Thus as we have chiral symmetry away from the continuum, the relationships we derived between the renormalization constants in the continuum are still valid at finite lattice spacing. We are therefore free to use (6.17) to calculate Z_A.

6.3 Perturbative renormalization

The remaining operators in this thesis will be calculated from one-loop lattice perturbation theory. However as these numbers are not calculated here, I will only give a brief overview of the methods employed to calculate these numbers. For a full account see [62, 63].

In order to determine the renormalization constant $Z_{\mathcal{O}}$ of the operator $\mathcal{O}$ we must specify a renormalization scheme. A common choice on the lattice is a MOM scheme. Here the renormalization conditions specify that the gauge fixed quark propagator G must be proportional to the tree level propagator at some scale μ. A similar condition holds for the amputated Green function $\Lambda_{\mathcal{O}}$, which is formed from an operator insertion into a quark line. Thus we have

$$Z_\psi^{\mathrm{MOM}}(a\mu)G|_{p^2=\mu^2} \;=\; G^{\mathrm{tree}}$$

Figure 6.1: One loop diagrams contributing to Z_ψ.

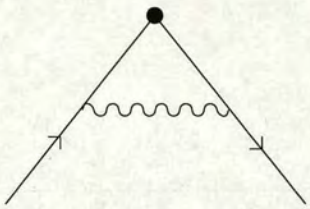

Figure 6.2: One loop diagram contributing to $Z_\mathcal{O}$.

$$\frac{Z_\mathcal{O}^{\mathrm{MOM}}(a\mu)}{Z_\psi^{\mathrm{MOM}}(a\mu)}\Lambda_\mathcal{O}|_{p^2=\mu^2} = \Lambda_\mathcal{O}^{\mathrm{tree}} + \ldots, \tag{6.29}$$

where the ... indicate other Dirac structures, which since they are simply a result of the lattice breaking Lorentz invariance are ignored. Contributions to the wavefunction renormalization (Figure 6.1) and the operator renormalization (Figure 6.2) are then calculated.

The result for a general operator can be written as

$$Z_\mathcal{O}^{\mathrm{MOM}} = 1 - \frac{g^2 C_F}{16\pi^2}[\gamma_\mathcal{O}\log(a\mu) + B_\mathcal{O}^{\mathrm{MOM}}], \tag{6.30}$$

where C_F is the quadratic Casimir of $SU(3)$, $\gamma_\mathcal{O}$ is the anomalous dimension, and $B_\mathcal{O}$ is a finite piece which will in general depend on the scheme. These perturbative results can then be tadpole improved as described in Section 3.7.

As the Wilson coefficients for the operator product expansion are often

calculated in the $\overline{MS}$ scheme, we can convert the MOM scheme numbers to the $\overline{MS}$ scheme by

$$Z_{\psi,\mathcal{O}}^{\overline{MS}}(a\mu) = Z_{\psi,\mathcal{O}}^{\overline{MS},\mathrm{MOM}} Z_{\psi,\mathcal{O}}^{\mathrm{MOM}}(a\mu), \tag{6.31}$$

where $Z_{\psi,\mathcal{O}}^{\overline{MS},\mathrm{MOM}}$ is calculable in continuum perturbation theory [64].

Finally, the numbers calculated in [62, 63] are calculated at $\mu = \frac{1}{a}$ in order to avoid the logarithms in (6.31) becoming large. As the lattice spacing changes with the coupling, in order to perform a continuum extrapolation we must transform our renormalization constants to the same scale. The scale dependence of a renormalized operator $\mathcal{O}^S$ in scheme $\mathcal{S}$ is determined using the renormalization group equation

$$\left[\frac{\partial}{\partial \log \mu} + \beta^S(g^S(\mu))\frac{\partial}{\partial g^S} + \gamma_m^S(g^S(\mu))\frac{\partial}{\partial \log m^S(\mu)} + \gamma_{\mathcal{O}}^S(g^S(\mu))\right]\mathcal{O}^S(\mu) = 0, \tag{6.32}$$

where

$$\begin{aligned}
\beta^S(g^S(\mu)) &\equiv \frac{\partial g^S(\mu)}{\partial \log \mu} \\
\gamma_m^S(g^S(\mu)) &\equiv \frac{\partial \log m^S(\mu)}{\partial \log \mu} \\
\gamma_{\mathcal{O}}^S(g^S(\mu)) &\equiv \frac{\partial \log Z_{\mathcal{O}}^S(\mu)}{\partial \log \mu}.
\end{aligned} \tag{6.33}$$

Thus β, γ_m, and $\gamma_{\mathcal{O}}$ respectively determine the scale dependence of the coupling, the mass, and the operator.

As this is a differential equation in μ, if we integrate this equation we should get a result which is independent of the scale. This is the renormalization group invariant (RGI) form of the operator

$$\mathcal{O}^{RGI} = \Delta Z_{\mathcal{O}}^S(\mu)\mathcal{O}^S(\mu), \tag{6.34}$$

where $\Delta Z_{\mathcal{O}}^{S}(\mu)$ is the factor picked up from integration. It can be written [49] as

$$[\Delta Z_{\mathcal{O}}^{S}(\mu)]^{-1} = [2b_0(g^S(\mu)^2]^{-\frac{d_0}{2b_0}} \exp \int_0^{g^S(\mu)} d\xi \left[\frac{\gamma_{\mathcal{O}}^{S}(\xi)}{\beta^S(\xi)} + \frac{d_0}{b_0\xi}\right], \tag{6.35}$$

where b_0 and d_0 are the lowest order terms in the expansion of β and $\gamma_{\mathcal{O}}$. We can therefore use the RGI form of operator to change from one scale μ to another scale μ' since

$$\Delta Z_{\mathcal{O}}^{S}(\mu)\mathcal{O}^S(\mu) = \mathcal{O}^{RGI} = \Delta Z_{\mathcal{O}}^{S}(\mu')\mathcal{O}^S(\mu'), \tag{6.36}$$

and so

$$\mathcal{O}^S(\mu') = \frac{\Delta Z_{\mathcal{O}}^{S}(\mu)}{\Delta Z_{\mathcal{O}}^{S}(\mu')}\mathcal{O}^S(\mu). \tag{6.37}$$

Chapter 7

Locality and condition number

While the overlap operator preserves chiral symmetry, it does so at a cost. The interactions are no longer nearest neighbour and so it is no longer obvious that the the operator is local. However if we can show that the non-locality of the operator decays exponentially with distance, then for an application of D_{ov} to the field $\psi(x)$, the product $D_{ov}\psi(x)$ will be dominated by contributions from points close to x. Further if the localization length scales with the lattice spacing then strict locality will be returned in the continuum limit. As long as our operator satisfies these conditions, while it is not ultra-local in the sense of having only nearest neighbour interactions, it can be considered local enough.

In this section we attempt to prove our operator is local in the sense of the definition of locality given above. Furthermore, in Section 3.7 we commented on our hope that using the Lüscher-Weisz gauge action, as opposed to the Wilson gauge action, would increase the locality of our Dirac operator and also improve the condition number of the matrix inversion. Here

we investigate to what extent these statements are true. We compare locality and condition number on two $16^3 \times 32$ Lüscher-Weisz ensembles with $\beta = 8.00, 8.45$, and also a $16^3 \times 32$ ensemble of Wilson gauge configurations with $\beta = 6.00$. The Wilson gauge ensemble was chosen to have the same lattice spacing as the $\beta = 8.45$ set, and so allow a direct comparison of the two actions. All ensembles contain 50 configurations.

We also look at the dependence of these quantities on the negative mass parameter ρ. As any physical quantities we measure should not depend on our choice of ρ (see Section 3.2.3), we can use our results to determine an optimal choice.

7.1 Locality

In order to prove locality we follow the method of [65].
We first define a source field

$$\chi_\alpha(x) = \delta_{xy}\delta_{\alpha 1}, \tag{7.1}$$

where y is one particular point on the lattice and α runs over both colour and spin indices. The only non local part of the overlap operator is the sgn function so we apply this to our delta function source and see how far the signal spreads. We define a new field

$$\psi(x) = \mathrm{sgn}[\gamma_5(D_w - \rho)]\chi(x), \tag{7.2}$$

and then look at the decay of this field with distance $r = ||x - y||_1$ where r is defined in terms of the "taxi driver" norm

$$||x - y||_1 = \sum_\mu |x_\mu - y_\mu|, \tag{7.3}$$

which we calculate modulo the size of the lattice dimension in question. The function[1]

$$f(r) = max\{||\psi(x)||, ||x - y||_1 = r\} \tag{7.4}$$

is plotted for all three ensembles, with $\rho = 1.0, 1.2, 1.4, 1.6, 1.8$. We also include the free-field measurement. The results are shown in Figures 7.1, 7.2, 7.3, and 7.4.

In all cases $f(r)$ decays rapidly with distance. From around $r > 13$, $f(r)$ can be fitted reasonably well with a single exponential.

$$f(r) = Ae^{\frac{-\nu r}{a}}. \tag{7.5}$$

Around $r > 20$ we run into rounding errors as we are at the limit of machine precision, so this determines our fit region. The results for the fits $f(r)$ to (7.5) are shown in Table 7.1.

From symmetry arguments we would expect the free field results to show an optimal value of ρ around 1.0. The free field result is not as smooth as the other results, as can be seen by the kinks in Figure 7.1. This is most likely due to the fact that for a given r there are many different ways of forming that path, some of which are purely spatial, some purely timelike, and some mixtures of the two. Thus we might expect shifts in the amplitudes, especially at distances which are multiples of the lattice size, which would lead to a non-uniform exponential decay. This effect does not appear in the other cases so is presumably a product of the high levels of degeneracy in the free field case. This does however mean that the fitting with a single exponential is less trust-worthy than in the other cases. Nevertheless, the

[1] where $||\psi(x)||$ is the usual vector norm $\sqrt{\psi^\dagger\psi}$.

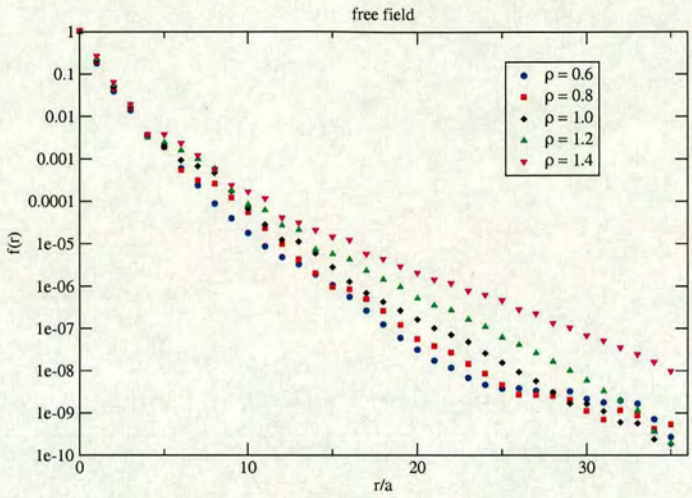

Figure 7.1: $f(r)$ against $\frac{r}{a}$ for free field.

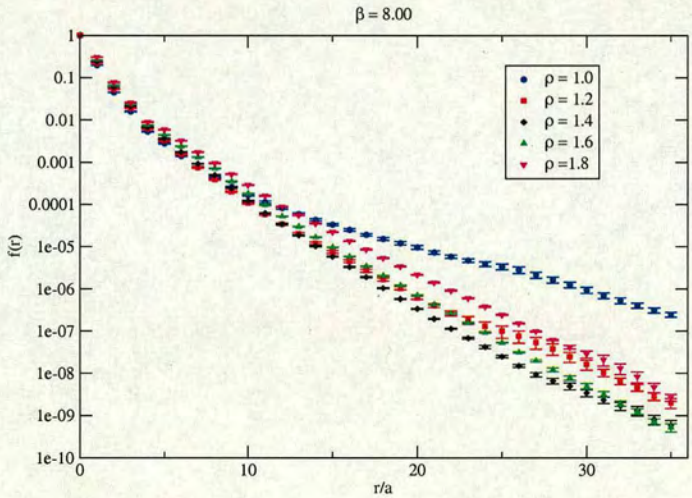

Figure 7.2: $f(r)$ against $\frac{r}{a}$ for $\beta = 8.00$.

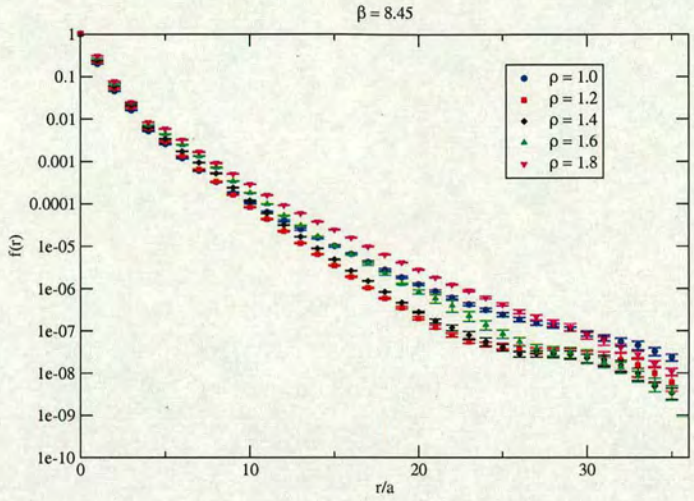

Figure 7.3: $f(r)$ against $\frac{r}{a}$ for $\beta = 8.45$.

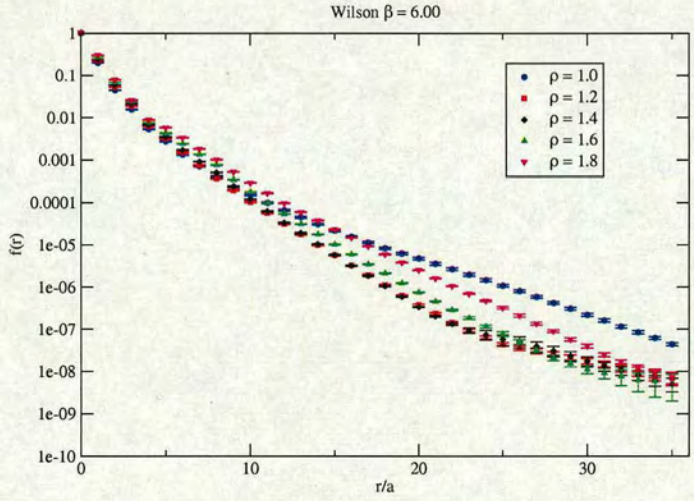

Figure 7.4: $f(r)$ against $\frac{r}{a}$ for Wilson $\beta = 6.00$.

Gauge action	ρ	A	ν
Lüscher-Weisz,	1.0	0.00191^{+31}_{-32}	0.270^{+9}_{-11}
$\beta = 8.00$	1.2	0.0111^{+15}_{-16}	0.489^{+7}_{-7}
	1.4	0.0334^{+19}_{-20}	0.577^{+3}_{-3}
	1.6	0.0280^{+15}_{-13}	0.531^{+3}_{-3}
	1.8	0.0232^{+14}_{-11}	0.464^{+3}_{-3}
Lüscher-Weisz,	1.0	0.00671^{+90}_{-74}	0.432^{+7}_{-6}
$\beta = 8.45$	1.2	0.0315^{+32}_{-24}	0.608^{+7}_{-5}
	1.4	0.0326^{+22}_{-23}	0.588^{+4}_{-5}
	1.6	0.0171^{+23}_{-22}	0.495^{+9}_{-10}
	1.8	0.0209^{+8}_{-9}	0.451^{+3}_{-3}
Wilson,	1.0	0.00187^{+18}_{-13}	0.302^{+5}_{-4}
$\beta = 6.00$	1.2	0.0215^{+36}_{-25}	0.552^{+9}_{-7}
	1.4	0.0325^{+18}_{-23}	0.575^{+3}_{-4}
	1.6	0.0374^{+21}_{-19}	0.547^{+4}_{-4}
	1.8	0.0225^{+12}_{-9}	0.460^{+3}_{-3}
Free field	0.6	0.01259	0.628
	0.8	0.0770	0.701
	1.0	0.170	0.733
	1.2	0.00543	0.457
	1.4	0.00384	0.372

Table 7.1: Fit parameters for $f(r)$ against r/a.

value of the decay parameter ν does appear to have a maximum around $\rho = 1.0$.

While $\rho = 1.0$ is the expected optimal value for free-field, once we turn on the interactions the spectrum of the Dirac operator will shift, and so we would expect that the optimal value would shift as well. All 3 ensembles do show a maximum turning point for ν as ρ is varied. For Lüscher-Weisz $\beta = 8.00$, the optimum value of ρ seems to sit at 1.4, while for Lüscher-Weisz $\beta = 8.45$, and Wilson $\beta = 6.00$, the optimum value sits somewhere between 1.2 and 1.4.

At the optimal values, there is only a small difference in the decay parameter. For the two Lüscher-Weisz ensembles, the $\beta = 8.45$ set shows at most a 5% increase over the $\beta = 8.00$ set. From this we can conclude that ν is fairly independent of the lattice spacing, and hence our localization radius $f(r)$ will collapse to a delta function in the continuum limit. Similarly when the $\beta = 8.45$ set is compared to the Wilson numbers the effect is at most 5%. Thus with an appropriate choice of ρ, the localization properties of the Dirac operator have very little dependence on the underlying gauge field. This is perhaps not surprising. The source of the non-locality is the fermion operator: it couples sites together at arbitrary distances. The gauge field merely determines the strength of these interactions. Further, the difference between the two gauge actions is only at the $\mathcal{O}(a^2)$ level and so should (hopefully) be small.

7.2 Condition number

The time taken to invert the Dirac operator is related to the ratio of the largest and smallest eigenvalues of the operator. This is known as the condition number κ of the Dirac matrix. While the exact number of iterations required for an inversion will depend on the whole spectrum of the operator, the condition number is still a good measure of relative inversion time since we would expect in general that the number of iterations required to increase the accuracy of a matrix solve would grow proportional to the square root of the condition number [66].

For the overlap operator, most of the time during the inversion is spent in the inner kernel of the nested conjugate gradient applying the sgn operator. This is equivalent to an inversion of $(\gamma_5 D_w)^2$ (see Section 3.3), so it is the condition number of this matrix that will to a great extent determine the computational cost of our propagator inversions. However as mentioned earlier, the spectrum of $\gamma_5 D_w$ has a few discrete low lying eigenvalues, followed by a dense continuum. As such we project out some quantity of these near-zero modes and deal with them explicitly. While this is done primarily to ensure the accuracy of the rational approximation, it also has the computational benefit of lowering the resulting matrix's condition number and thus speeding up the inversion.

The mean of the condition number $\bar{\kappa}$ and the standard deviation $s(\kappa)$ for $(\gamma_5 D_w)^2$ on each of the three ensembles considered in this section are shown in Table 7.2. We again look at the ρ dependence. We show the values without eigenvalue projections, and also after projection of the 16 lowest lying eigenvalues.

		Without projection		With Projection	
Gauge action	ρ	$\bar{\kappa}$	$s(\kappa)$	$\bar{\kappa}$	$s(\kappa)$
Lüscher-Weisz,	1.0	2.356×10^{10}	1.664×10^{11}	37615	13542
$\beta = 8.00$	1.2	1.319×10^{8}	7.148×10^{8}	10914	5907
	1.4	4.000×10^{7}	1.893×10^{8}	6845	3888
	1.6	9.400×10^{7}	5.711×10^{8}	5529	3303
	1.8	5.209×10^{8}	2.331×10^{9}	5379	3309
Lüscher-Weisz,	1.0	1.643×10^{6}	1.079×10^{7}	1415	88
$\beta = 8.45$	1.2	1.728×10^{6}	1.095×10^{7}	650	39
	1.4	2.507×10^{4}	1.064×10^{5}	463	27
	1.6	4.417×10^{4}	1.317×10^{5}	416	28
	1.8	1.799×10^{4}	6.078×10^{4}	444	28
Wilson,	1.0	5.200×10^{6}	2.617×10^{7}	3865	677
$\beta = 6.00$	1.2	5.851×10^{8}	4.118×10^{9}	1496	300
	1.4	1.665×10^{7}	8.933×10^{7}	1115	218
	1.6	1.120×10^{7}	7.077×10^{7}	1105	278
	1.8	1.114×10^{6}	3.801×10^{6}	1250	261

Table 7.2: Mean and standard deviations for κ of $(\gamma_5 D_w)^2$, with and without projection.

In all cases we see that the eigenvalue projection has a drastic effect on the condition number. In some cases it drops both ($\bar{\kappa}$) and $s(\kappa)$ by four to five orders of magnitude (see Figure 7.5). The mean obviously drops because we are removing the lowest eigenvalues. We also expect $s(\kappa)$ to drop even more rapidly than $\bar{\kappa}$ as we approach the eigenvalue continuum since in addition to the overall lowering of the condition number, the remaining eigenvalues become bunched closer and closer together and so the variation per configuration will become smaller and smaller.

If we now compare the $\beta = 8.00, \rho = 1.4$ projected result with the corresponding $\beta = 8.45$ result (Figure 7.6), we see that for the $\beta = 8.45$ set we have clearly projected out all of the discrete near-zero modes as we have a low condition number, and more importantly very little variation from configuration to configuration. For the $\beta = 8.00$ set, we have a matrix which has a condition number an order of magnitude higher, and which still has some variation. This is a result of the stronger value of the coupling, which leads to a coarser lattice. It is known from analysis of the full spectrum of $(\gamma_5 D_w)$ that the number of near zero modes increases as the lattice spacing increases. The continuum also becomes less dense with increasing lattice spacing [65]. Thus for larger physical volumes, we end up with an increasingly poorly conditioned matrix. To help ameliorate this, when we come to perform the full propagator inversions we project more eigenvalues for the coarser lattice. In practice, projecting out the lowest 64 eigenvalues ensures we reach the continuum region and lowers the solver iteration counts to a tolerable level. However as this region is also wider we still end up a system which is poorly conditioned in comparison to the finer lattice.

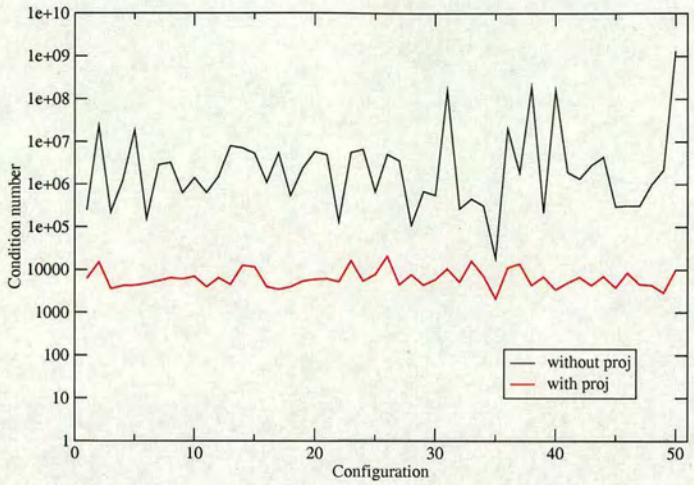

Figure 7.5: Condition number of $(\gamma_5 D_w)^2$ on Lüscher-Weisz with $\beta = 8.00$, $\rho = 1.4$.

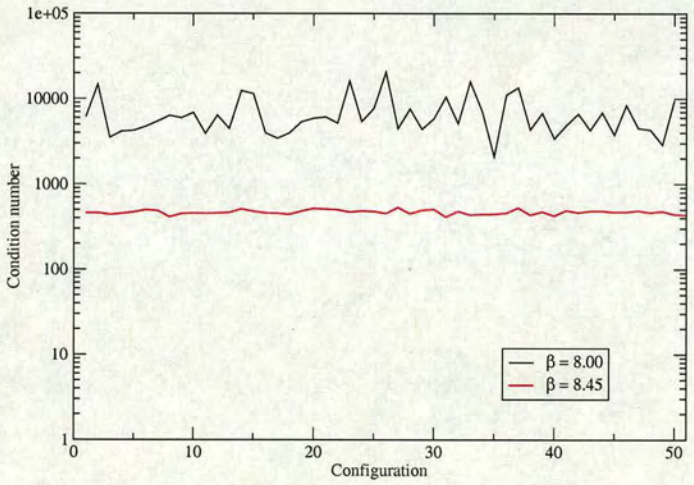

Figure 7.6: Condition number of $(\gamma_5 D_w)^2$ with eigenvalue projection, on Lüscher-Weisz with $\beta = 8.45$ and $\beta = 8.00$, $\rho = 1.4$.

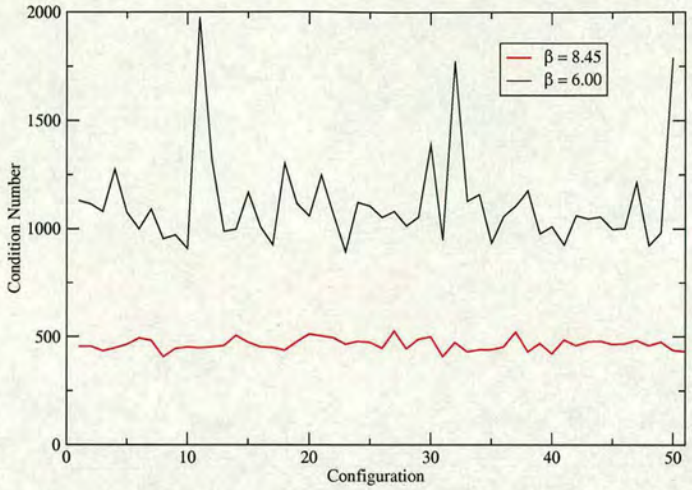

Figure 7.7: Condition number of $(\gamma_5 D_w)^2$ with eigenvalue projection, on Lüscher-Weisz with $\beta = 8.45$ and Wilson with $\beta = 8.00$, $\rho = 1.4$.

If we now make a similar comparison between the $\beta = 8.45$ ensemble, and the Wilson ensemble we see a similar (if less pronounced) effect. In Figure 7.7 we show the condition number of the projected operators. We see that on the Wilson ensemble we have a greater number of low lying eigenvalues (as evidenced by the greater variation from configuration to configuration), and a condition number which is 2 to 3 times higher. As the volumes in these two cases are the same, the extra low lying modes must be a result of the larger lattice artifacts present in the Wilson gauge action. Thus while the Lüscher-Weisz action has little advantage over the Wilson action in terms of the localization of the overlap operator, it can offer significant gains in terms of inversion times due to a better conditioned fermion matrix.

Lastly, we are now in a position to use the ρ dependence of the locality and the condition number in order to determine an optimal value of ρ for

the two Lüscher-Weisz ensembles used in this thesis. In Figures 7.8 and 7.9 we plot condition number against locality for both ensembles. Clearly we are looking for the best combination of large locality and small condition number. Hence the optimal value should lie in the top left of the plots. On both sets it's clear that $\rho = 1.4$ is the best compromise and hence we use this value in our overlap operator.

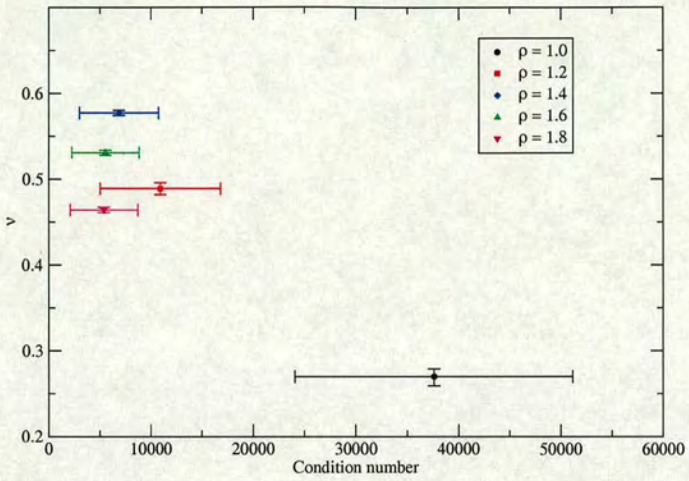

Figure 7.8: Condition number of projected $(\gamma_5 D_w)^2$ against the locality decay parameter ν on Lüscher-Weisz with $\beta = 8.00$.

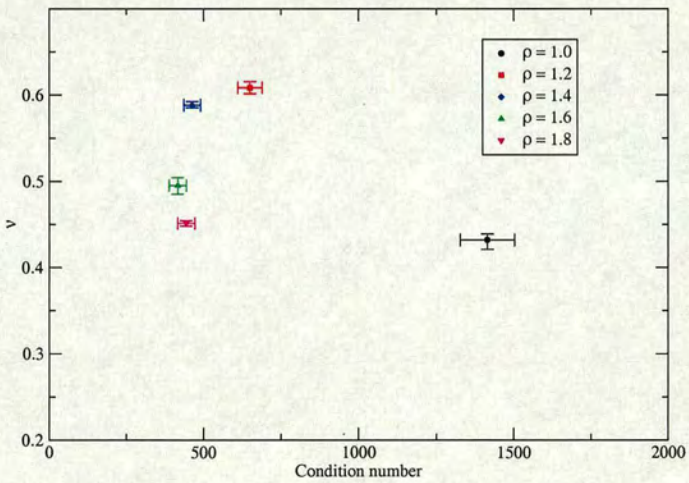

Figure 7.9: Condition number of projected $(\gamma_5 D_w)^2$ against the locality decay parameter ν on Lüscher-Weisz with $\beta = 8.45$.

Chapter 8

Results

In this section we present the main results of the lattice simulation. After measurements of the masses of some low lying states, we compute lattice renormalization constants. We then look at matrix elements to determine decay constants and low moments of nucleon structure functions.

The simulations are run at five quark masses and extrapolated to the chiral limit. A modest attempt is made to test the scaling of these results by performing the calculations at two lattice spacings. We use two ensembles of $16^3 \times 32$ Lüscher-Weisz gauge configurations. Measurements are made on $O(50)$ configurations for $\beta = 8.45$. For $\beta = 8.00$ we have $O(40)$ configurations for 2-pt functions and $O(30)$ configurations for 3-pt functions . The scale is set by using the Sommer parameter r_0 [67], which gives a lattice spacing of $a = 0.136$ fm for the $\beta = 8.00$ set, and $a = 0.095$ fm for $\beta = 8.45$ [68]. The five quark masses correspond to $a\mu \equiv \frac{am_q}{2\rho} = 0.01, 0.015, 0.02, 0.035, 0.05$ for $\beta = 8.45$. We use $a\mu = 0.015, 0.02, 0.03, 0.05, 0.07$ for $\beta = 8.00$. In both cases $\rho = 1.4$.

8.1 Mass spectrum

One of the main tasks of lattice QCD is to measure the hadron mass spectrum. Agreement with experimentally measured values would provide further evidence that QCD correctly describes the strong interactions. Recent results in this regard can be found in [69, 70]. While it would be preferable to have exact agreement with the experimental values, deviations from experiment give some indication of the errors introduced into the simulation from the various approximations that are made (i.e. quenching, finite volume, discrete lattice, and heavier than physical quark masses). The effect of all but the first of these approximations can be accounted for by making extrapolations to respectively the infinite volume, continuum, and chiral limits. However the problem of quenching remains as it will shift the spectrum of the theory. As we are suppressing virtual quark loops, the error will obviously increase as we go to lighter quark mass. Thus the error from quenching will show up in the chiral extrapolations.

The mass scaling of QCD Green's functions close to the chiral limit is described well by Chiral perturbation theory (χpt) [37, 38]. It describes the form of the mass scaling of the hadron spectrum with respect to the quark masses by making expansions in light meson loops around the chiral limit. These expansions contain both analytic and non-analytic terms, with the lowest order non-analytic terms proportional to M_π^3 and $M_\pi^4 \log(M_\pi)$. The equivalent Quenched chiral perturbation expansions [39, 40] contain additional, lower order non-analytic terms proportional to M_π and $M_\pi^2 \log(M_\pi)$. These terms then describe the divergence of the quenched spectrum from QCD as we approach the chiral limit. As we have an action with good chiral

properties, and are able to go to relatively light quark masses, we may begin to see the effects of these quenched chiral artifacts show up.

In what follows we show measurements of the mass of the pion, rho, and the nucleon. We also look for evidence of non-analytic terms in the chiral extrapolations by attempting to fit to functional forms predicted by Quenched χpt.

8.1.1 m_π

The pion mass is calculated from the $\langle P(t)P(0)\rangle$ pseudoscalar correlator. To improve the overlap with the pion we Jacobi smear (see Section 4.3.1) at source using $N_s = 50$ and $\kappa_s = 0.21$. We do not smear at sink as we find

Ensemble	am_q	am_π	$m_\pi[MeV]$
$\beta = 8.45$	0.028	0.213^{+4}_{-4}	442^{+8}_{-8}
	0.042	0.254^{+4}_{-3}	528^{+8}_{-6}
	0.056	0.291^{+4}_{-3}	604^{+8}_{-6}
	0.098	0.388^{+3}_{-2}	806^{+6}_{-4}
	0.140	0.471^{+2}_{-2}	978^{+4}_{-4}
$\beta = 8.00$	0.042	0.274^{+2}_{-2}	398^{+3}_{-3}
	0.056	0.315^{+2}_{-2}	457^{+3}_{-3}
	0.084	0.384^{+2}_{-2}	557^{+3}_{-3}
	0.140	0.498^{+2}_{-2}	723^{+3}_{-3}
	0.196	0.595^{+2}_{-2}	863^{+3}_{-3}

Table 8.1: Fitted pion masses.

better signals for point sinks. The effective mass is then found by fitting to an effective cosh as described in Section 4.1. The effective mass plots used to help determine the fit ranges are shown in Figures 8.1, 8.2. The measured masses are shown in Table 8.1, where in the final column we convert the masses to physical units using the lattice spacings given in the introduction to this section. The errors are estimated using the bootstrap method.

If we now form chiral extrapolations, from the axial Ward identity (6.10) we expect the pion mass to vanish in the chiral limit and at first order $m_\pi^2 \propto m_q$. If we make a linear extrapolation in the quark mass this seems to fit the data very well (Figures 8.3, 8.4). Both fits pass through zero within errors at $am_q = 0$, with $(am_\pi)^2 = -0.0017^{+23}_{-20}$, -0.0012^{+16}_{-14} for the 8.45 and 8.00 sets respectively.

Quenched chiral perturbation theory (Qχpt) predicts [71] the following expansion for m_π^2,

$$m_\pi^2 = Km_q(1 - \delta[\log(Km_q/\Lambda_\chi^2) + 1]) + O(m_q^2), \tag{8.1}$$

where the chiral scale factor $\Lambda_\chi = 4\pi f_\pi = 1169MeV$. If we fit our data using the fit function

$$m_\pi^2 = Am_q + Bm_q \log(m_q) + Cm_q^2, \tag{8.2}$$

then we can extract a value for the chiral log parameter δ. The results of the

Ensemble	A	B	C	δ
$\beta = 8.45$	0.67^{+23}_{-23}	-0.23^{+8}_{-7}	3.28^{+59}_{-61}	0.19^{+9}_{-9}
$\beta = 8.00$	1.25^{+13}_{-12}	-0.15^{+4}_{-4}	1.60^{+23}_{-27}	0.10^{+3}_{-3}

Table 8.2: Pion mass fits using extrapolation from Qχpt.

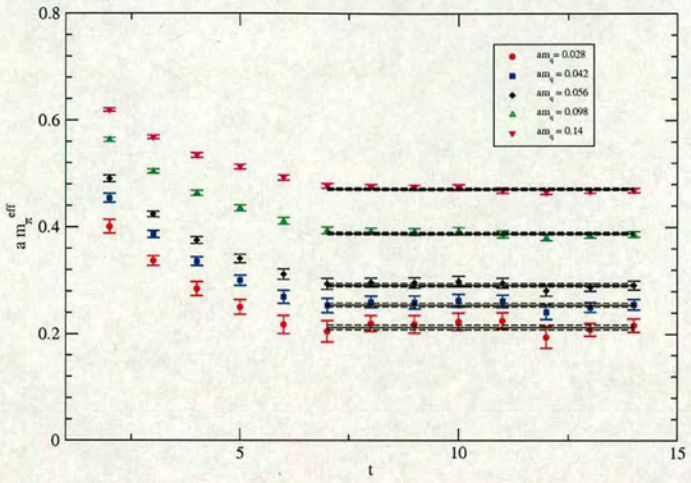

Figure 8.1: Pion effective mass plot for $\beta = 8.45$.

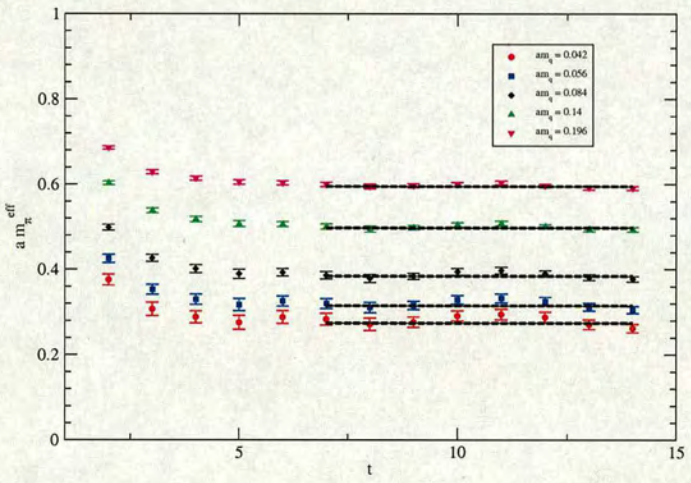

Figure 8.2: Pion effective mass plot for $\beta = 8.00$.

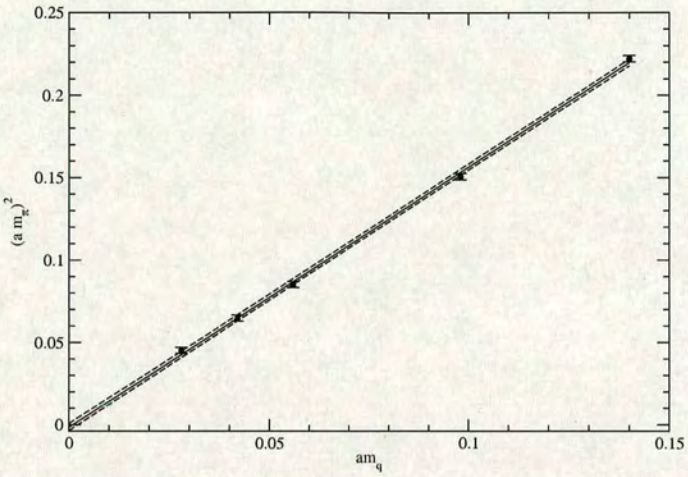

Figure 8.3: Linear chiral extrapolation of $(am_\pi)^2$ for $\beta = 8.45$.

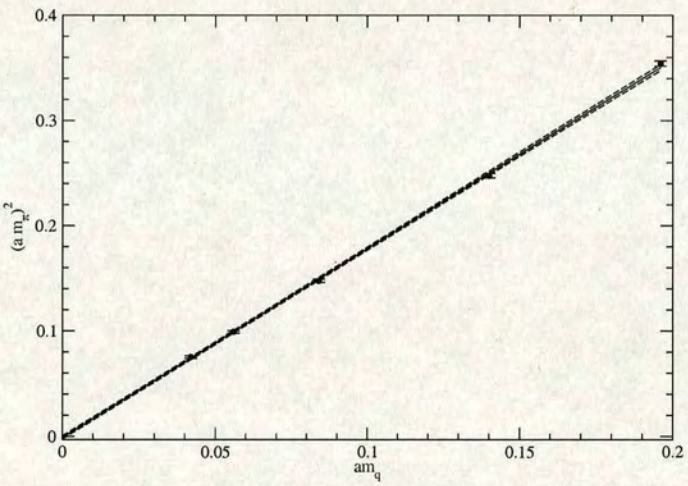

Figure 8.4: Linear chiral extrapolation of $(am_\pi)^2$ for $\beta = 8.00$.

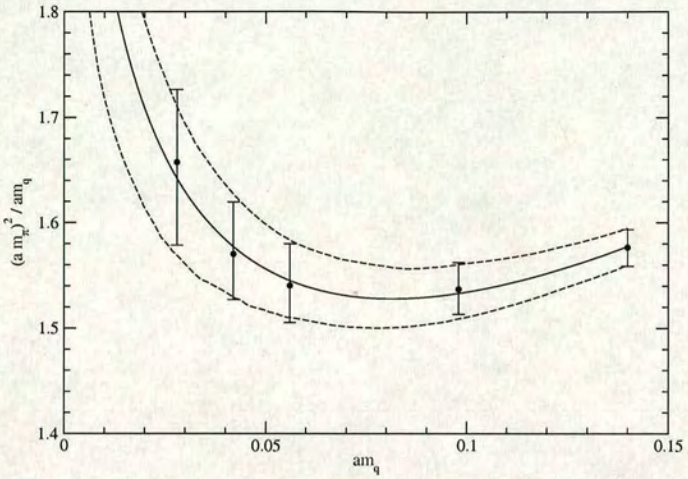

Figure 8.5: Ratio of $(am_\pi)^2/am_q$ for $\beta = 8.45$.

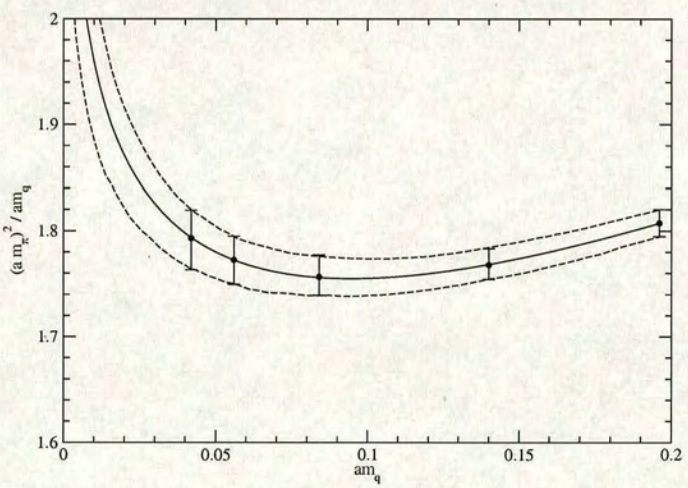

Figure 8.6: Ratio of $(am_\pi)^2/am_q$ for $\beta = 8.00$.

fits are shown in Table 8.2. While the error bars are quite large, especially in the 8.45 set, the central values seem reasonably consistent with previous Clover [72], Fixed-point [73], and Domain wall [74] measurements at similar masses and lattice volumes.

By dividing out the linear behaviour and plotting $\frac{(am_\pi)^2}{am_q}$, we can look for the onset of chiral logs. From Figures 8.5, 8.6, we see that the deviation from linear behaviour begins to happen around a pion mass of around 400-500 MeV. While it would be tempting to declare this the radius of applicability for quenched chiral perturbation theory, recent measurements have shown that while logs may appear at this scale, δ and hence Qχpt do not become stable until $m_\pi < 300MeV$ [75].

It should also be noted that in forming the chiral extrapolation to search for chiral logs, we are fitting 5 points with a 3 parameter fit function. As the dominant behaviour is linear, any slight variation from linearity would be picked up by virtually any small order polynomial fit function. In fact examining Figure 8.5, a constant fit (corresponding to no chiral logs) would fit through all the points, within error bars. The same is almost true for Figure 8.6. So while these plots are at least consistent with Quenched χpt, a more thorough analysis with more masses is need to properly constrain the fit and prove that these apparent deviations from linearity are due to chiral logs.

8.1.2 m_ρ

We measure the mass of the ρ from the vector meson correlator $\langle V^i(t)V^i(0)\rangle$. In order to increase our statistics we sum the correlators over $i = 1, 2, 3$. We

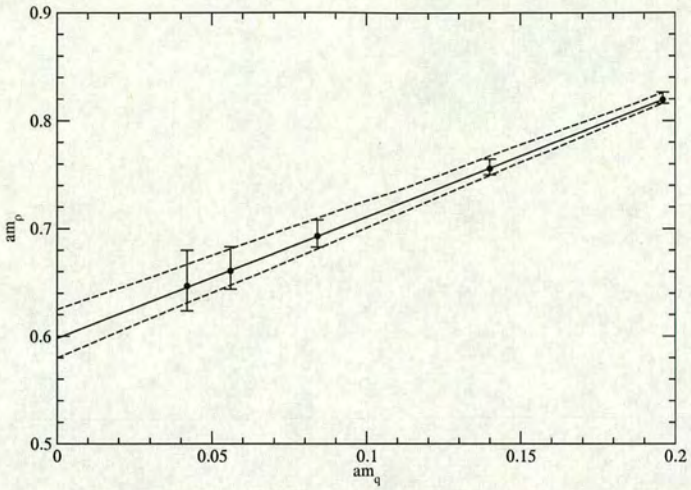

Figure 8.7: Linear chiral extrapolation of m_ρ for $\beta = 8.00$.

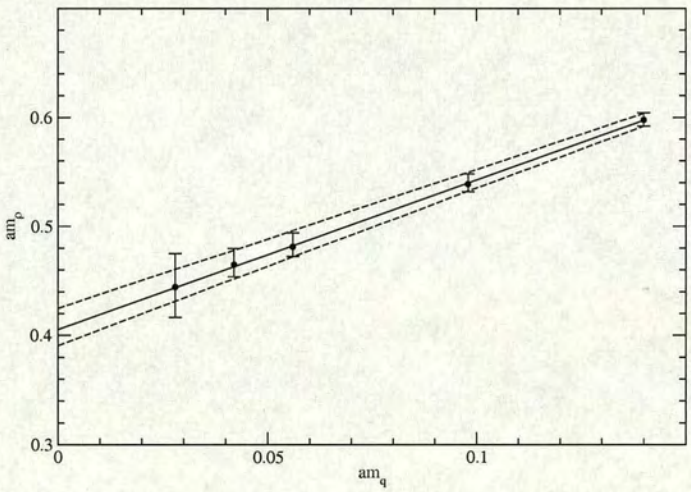

Figure 8.8: Linear chiral extrapolation of m_ρ for $\beta = 8.45$.

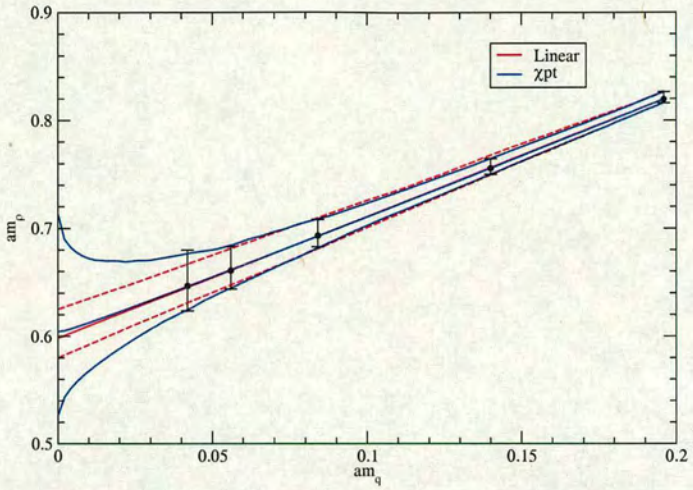

Figure 8.9: Chiral extrapolations of m_ρ for $\beta = 8.00$ using both linear and χpt fits.

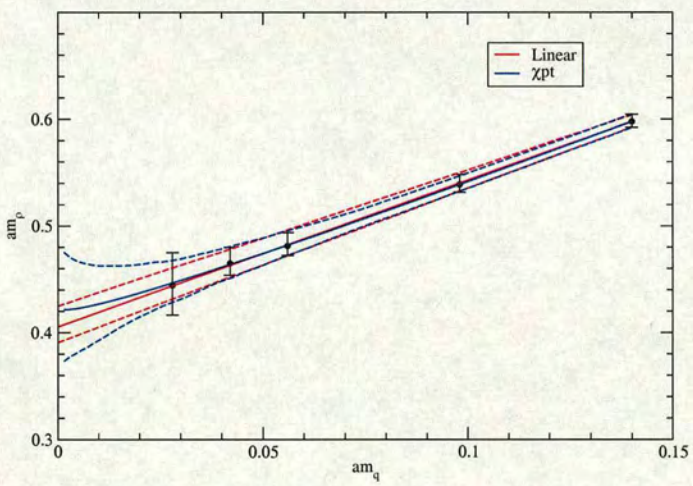

Figure 8.10: Chiral extrapolations of m_ρ for $\beta = 8.45$ using both linear and χpt fits.

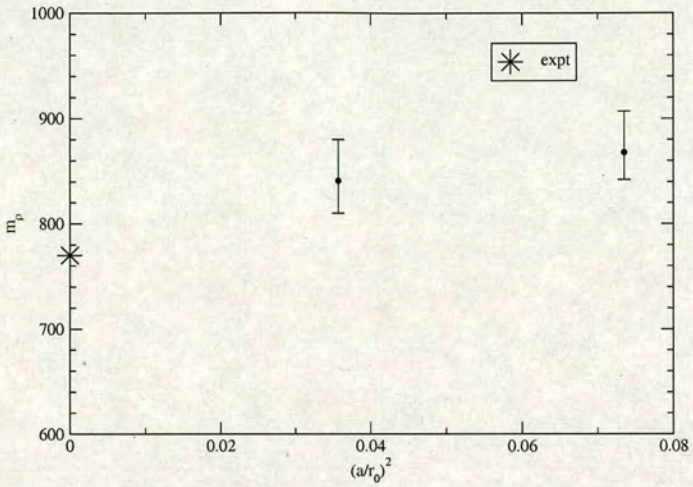

Figure 8.11: Continuum extrapolation of m_ρ.

Ensemble	am_q	am_ρ	$m_\rho[MeV]$
$\beta = 8.45$	0.028	0.458^{+19}_{-17}	951^{+40}_{-36}
	0.042	0.465^{+15}_{-11}	966^{+31}_{-22}
	0.056	0.481^{+13}_{-9}	999^{+27}_{-18}
	0.098	0.539^{+9}_{-7}	1101^{+18}_{-14}
	0.140	0.598^{+7}_{-6}	1242^{+14}_{-12}
$\beta = 8.00$	0.042	0.647^{+33}_{-23}	939^{+48}_{-33}
	0.056	0.661^{+22}_{-17}	959^{+32}_{-25}
	0.084	0.693^{+15}_{-10}	1006^{+22}_{-15}
	0.140	0.756^{+9}_{-6}	1097^{+13}_{-9}
	0.196	0.819^{+7}_{-3}	1188^{+10}_{-4}

Table 8.3: Fitted rho masses.

Ensemble	Fit	A	B	C	am_ρ	$m_\rho[MeV]$
$\beta = 8.45$	Linear	0.405^{+19}_{-15}	–	1.37^{+8}_{-11}	0.405^{+19}_{-15}	841^{+39}_{-31}
	χpt	0.424^{+68}_{-59}	-0.14^{+34}_{-38}	1.60^{+54}_{-50}	0.421^{+54}_{-48}	874^{+113}_{-101}
$\beta = 8.00$	Linear	0.598^{+27}_{-18}	–	1.13^{+9}_{-12}	0.598^{+27}_{-18}	868^{+39}_{-26}
	χpt	0.60^{+11}_{-8}	-0.04^{+36}_{-49}	1.18^{+59}_{-44}	0.60^{+11}_{-7}	871^{+160}_{-102}

Table 8.4: Rho mass chiral extrapolation fit parameters.

again find that the best signal is obtained from smeared sources and point sinks. Results of the fits to the correlators are shown in Table 8.3.

To form the chiral extrapolation we first attempt a linear fit[1] of the form

$$m_\rho = A + Cm_q. \tag{8.3}$$

The results are plotted in Figures 8.7, 8.8. Again in both cases a linear extrapolation seems to fit the data very well.

The suggested fit function to for the vector meson from Qχpt is given by [76]

$$m_\rho = A + B\sqrt{m_q} + Cm_q + \ldots \tag{8.4}$$

The fits using this function are shown against the linear fits in Figures 8.9, 8.10. The results of both fits are shown in Table 8.4. In both plots, the fits agree at all points within the mass range considered. The χpt fit gives much larger errors and the coefficient of the non-analytic term is zero within errors in all cases. This coefficient is expected to be around -4δ [76]. We therefore conclude that for the ρ in the mass range considered there are no effects of chiral logs present.

[1] As we see no deviation from linearity, extrapolations in m_q and m_π^2 are equivalent.

The scaling of m_ρ with respect to the lattice spacing is shown in Figure 8.11. With only two lattice spacings, a linear fit is not very useful. The plot does however show that as expected there is not a large amount of scaling. The values seems a little high although we do have rather large error bars.

8.1.3 m_N

We compute the nucleon mass using the non-relativistic nucleon (4.25). Smeared sources and point sinks again give the best signals, although even in this case large fluctuations begin to set in for both data sets at low quark mass. This increases the difficulty in making stable fits. The extracted masses are given in Table 8.5.

Ensemble	am_q	am_N	$m_N[MeV]$
$\beta = 8.45$	0.028	0.605^{+16}_{-14}	1257^{+33}_{-29}
	0.042	0.639^{+12}_{-12}	1327^{+25}_{-25}
	0.056	0.684^{+10}_{-10}	1421^{+21}_{-21}
	0.098	0.795^{+8}_{-10}	1651^{+17}_{-21}
	0.140	0.901^{+6}_{-6}	1871^{+12}_{-12}
$\beta = 8.00$	0.042	0.870^{+26}_{-22}	1262^{+38}_{-32}
	0.056	0.899^{+23}_{-18}	1304^{+33}_{-26}
	0.084	0.962^{+18}_{-14}	1396^{+26}_{-20}
	0.140	1.080^{+11}_{-10}	1567^{+16}_{-15}
	0.196	1.199^{+10}_{-7}	1740^{+15}_{-110}

Table 8.5: Fitted Nucleon masses.

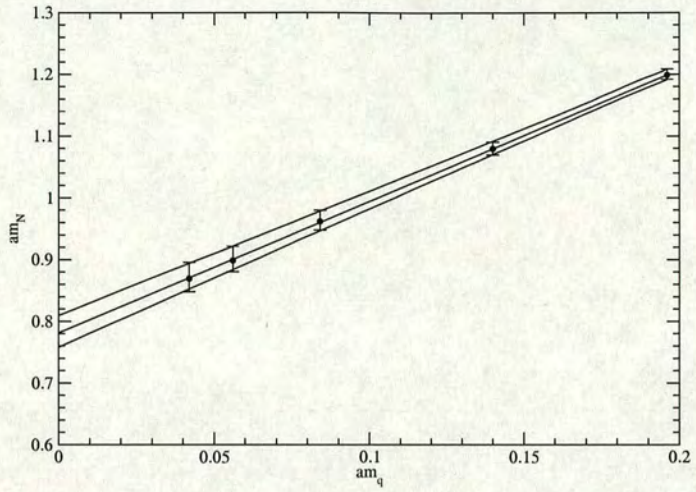

Figure 8.12: Linear chiral extrapolation of m_N for $\beta = 8.00$.

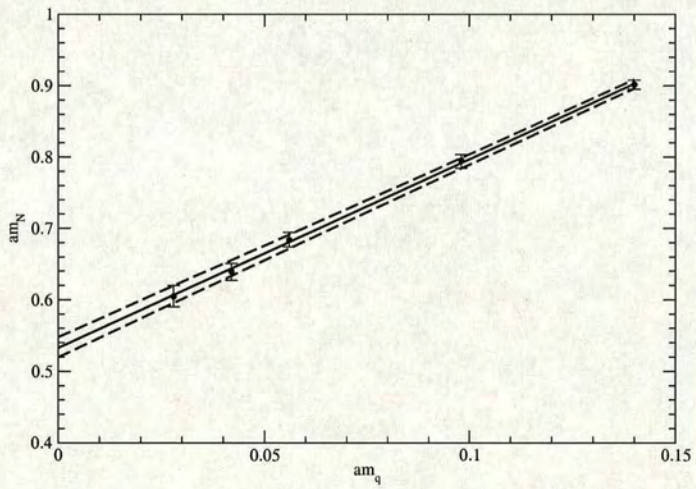

Figure 8.13: Linear chiral extrapolation of m_N for $\beta = 8.45$.

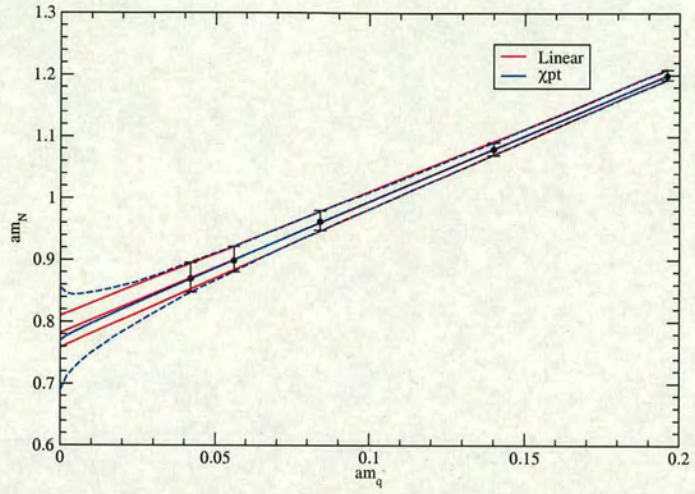

Figure 8.14: Chiral extrapolations of m_N for $\beta = 8.00$ using both linear and χpt fits.

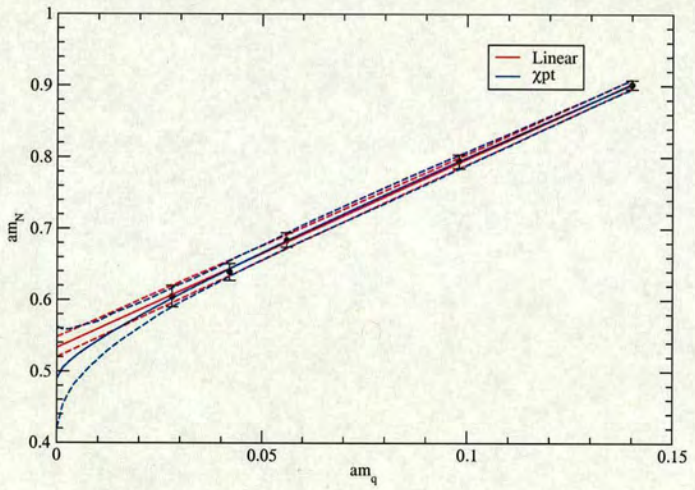

Figure 8.15: Chiral extrapolations of m_N for $\beta = 8.45$ using both linear and χpt fits.

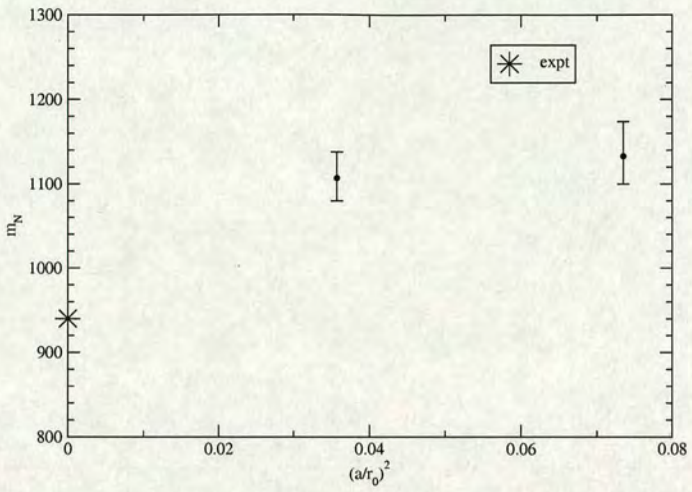

Figure 8.16: Continuum extrapolation of m_N.

Ensemble	Fit	A	B	C	am_N	$m_N[MeV]$
$\beta = 8.45$	Linear	0.533^{+15}_{-13}	–	2.64^{+8}_{-10}	0.533^{+15}_{-13}	1107^{+31}_{-27}
	χpt	0.490^{+72}_{-70}	0.32^{+49}_{-50}	2.08^{+92}_{-87}	0.490^{+56}_{-42}	1017^{+116}_{-87}
$\beta = 8.00$	Linear	0.781^{+28}_{-23}	–	2.13^{+11}_{-13}	0.781^{+28}_{-23}	1133^{+41}_{-33}
	χpt	0.770^{+85}_{-81}	0.07^{+45}_{-40}	2.03^{+54}_{-62}	0.770^{+85}_{-69}	1117^{+123}_{-100}

Table 8.6: Nucleon mass chiral extrapolation fit parameters.

We again attempt chiral extrapolations with both linear and quenched χpt fits of the same form as that for the rho. The linear fits are shown in Figures 8.12, 8.13. We superimpose these with the chiral fits in Figures 8.14, 8.14. The results for the fit parameters are shown in Table 8.6.

We see similar behaviour to that of the ρ. The data is very linear, and so the χpt fits follow the linear fits in the mass range studied with larger errors (as they have an extra degree of freedom to constrain). The coefficients of

the non-analytic term are again zero within errors, and in fact both are of the wrong sign. Thus we do not see any effects of quenched singularities.

The scaling with respect to the lattice spacing is shown in Figure 8.16. As was the case with the ρ we observe no significant scaling violations. Again the value seems to be too high, this time by around $\mathcal{O}(10\%)$. Note these discrepancies are primarily due to the quenched approximation which is not self consistent. While the full QCD spectrum should be independent of how the scale is set, the quenched mass spectrum shifts depending on which parameter is used to fix the scale[2]. These systematic errors are usually of the order seen here. If for example we used m_ρ to set the scale then we would get much closer agreement with experiment for m_N, but other quantities would shift.

8.2 Renormalization constants

In order to compare our results with continuum physics, any matrix elements we measure must be renormalized. The renormalization constants can be calculated either perturbatively or non-perturbatively. Here we give results of non-perturbative determinations of the axial and vector current renormalization constants, using the methods described in Section 6.2. The remaining matrix elements considered will be renormalized using perturbative values. These are not calculated here, but for completeness we show the results obtained. As these values are calculated at different scales, in order to make comparisons of matrix elements measured on different lattice ensembles we

[2]See for example [77]

must scale these numbers using the renormalization group equations. This is carried out and we give the final numbers used in this thesis.

8.2.1 Z_A

The renormalization constant Z_A of the local axial current A_μ can be determined non-perturbatively from the axial ward identity as described in Section 6.2.2.

Z_A can be extracted on the lattice from a ratio of two point correlation functions

$$Z_A(t) = \frac{2m_q\langle P(t)P(0)\rangle}{\langle \partial_4 A_4(t)P(0)\rangle}, \tag{8.5}$$

where P is the pseudoscalar. We again use Jacobi smeared sources and point sinks.

After very short times, $Z_A(t)$ becomes constant and provides a very clean signal. An example is shown in Figure 8.17. The fitted values for both ensembles are given in Table 8.8. Linear extrapolations to the chiral limit are shown in Figures 8.18,8.19. The values of Z_A in the chiral limit are given in Table 8.7.

Ensemble	Z_A
$\beta = 8.45$	1.412^{+3}_{-3}
$\beta = 8.00$	1.585^{+3}_{-3}

Table 8.7: Z_A extrapolated to the chiral limit.

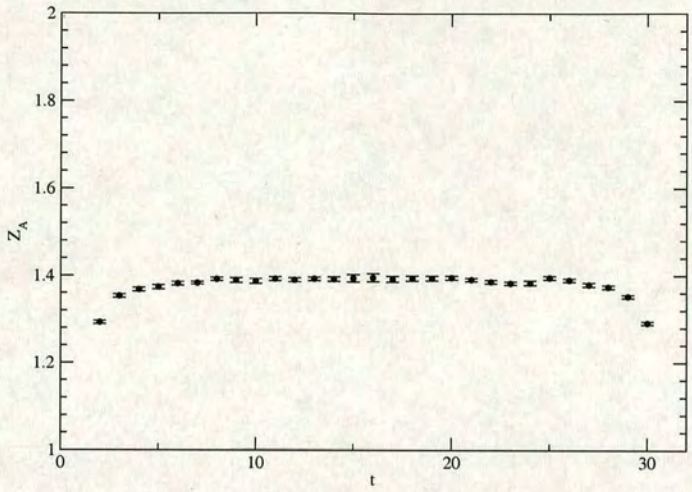

Figure 8.17: $Z_A(t)$ for $a\mu = 0.035$ and $\beta = 8.45$.

Ensemble	am_q	$Z_A(m_q)$
$\beta = 8.45$	0.028	1.404^{+3}_{-3}
	0.042	1.399^{+2}_{-2}
	0.056	1.397^{+2}_{-2}
	0.098	1.383^{+1}_{-2}
	0.140	1.371^{+2}_{-2}
$\beta = 8.00$	0.042	1.567^{+3}_{-2}
	0.056	1.562^{+3}_{-2}
	0.084	1.552^{+3}_{-2}
	0.140	1.530^{+3}_{-2}
	0.196	1.506^{+3}_{-2}

Table 8.8: Fitted values of Z_A.

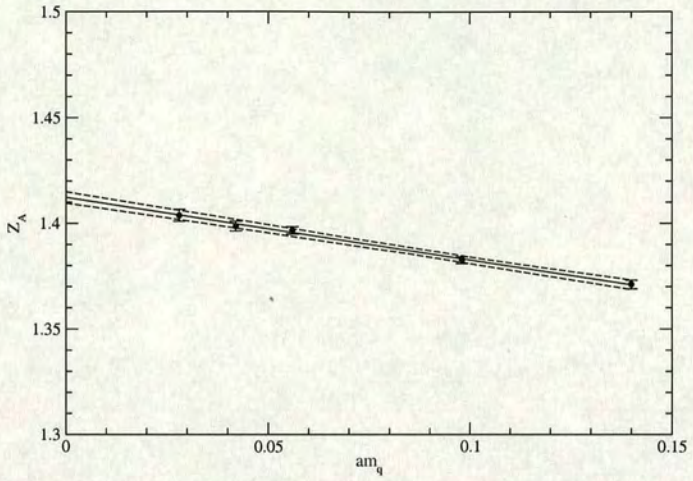

Figure 8.18: Chiral extrapolation of Z_A for $\beta = 8.45$.

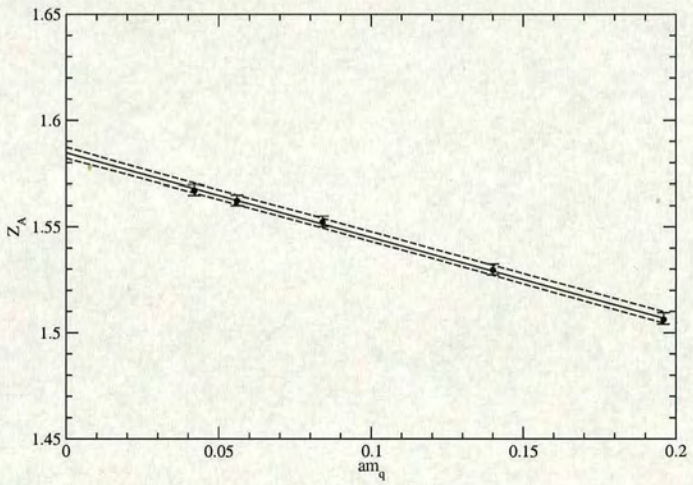

Figure 8.19: Chiral extrapolation of Z_A for $\beta = 8.00$.

8.2.2 Z_V

The renormalization constant Z_V of the local vector current V_μ is calculated from the ratio of 3-pt to 2-pt nucleon correlation functions. Following Section 6.2.1 we determine Z_V by

$$Z_V^{-1}(\tau) = \frac{\langle N(t) V_4^{NS}(\tau) N(0) \rangle}{\langle N(t) N(0) \rangle}, \tag{8.6}$$

where V_4^{NS} is the flavour non-singlet vector current (6.6). We Jacobi smear at both source and sink. For $0 < \tau < t$ we can measure the plateau. An example is shown in Figure 8.22. In both sets, fluctuations begin to set in for low quark masses. This does not present much of a problem for the $\beta = 8.45$ set, however due to the reduced statistics, the measurement of plateaus on the $\beta = 8.00$ becomes increasingly difficult for lower quark masses.

The fitted values are shown in Table 8.9. We perform linear extrapolations and compare the values with those of Z_A (see Figures 8.20, 8.21). The results of the chiral extrapolations for both Z_A and Z_V are shown in Table 8.10. While Z_A depends linearly on the quark mass, we expect that Z_V should be independent of the quark mass, and in both cases the chiral extrapolation of Z_V is reasonably flat. Chiral symmetry predicts that $Z_A = Z_V$ in the chiral limit. There is very good agreement in the $\beta = 8.45$ case. While the errors on the $\beta = 8.00$ set do overlap, there seems to some discrepancy between the two values, however this is almost certainly due to the difficulty in extracting stable fits for Z_V on this set.

Ensemble	am_q	$Z_V(m_q)$
$\beta = 8.45$	0.028	1.422^{+27}_{-26}
	0.042	1.401^{+19}_{-27}
	0.056	1.412^{+4}_{-4}
	0.098	1.412^{+2}_{-2}
	0.140	1.412^{+2}_{-2}
$\beta = 8.00$	0.042	1.553^{+78}_{-54}
	0.056	1.548^{+49}_{-58}
	0.084	1.548^{+17}_{-21}
	0.140	1.536^{+10}_{-14}
	0.196	1.538^{+8}_{-7}

Table 8.9: Fitted values of Z_V.

Ensemble	Z_V	Z_A
$\beta = 8.45$	1.412^{+7}_{-5}	1.422^{+7}_{-5}
$\beta = 8.00$	1.549^{+36}_{-25}	1.585^{+3}_{-3}

Table 8.10: Z_V, Z_A extrapolated to the chiral limit.

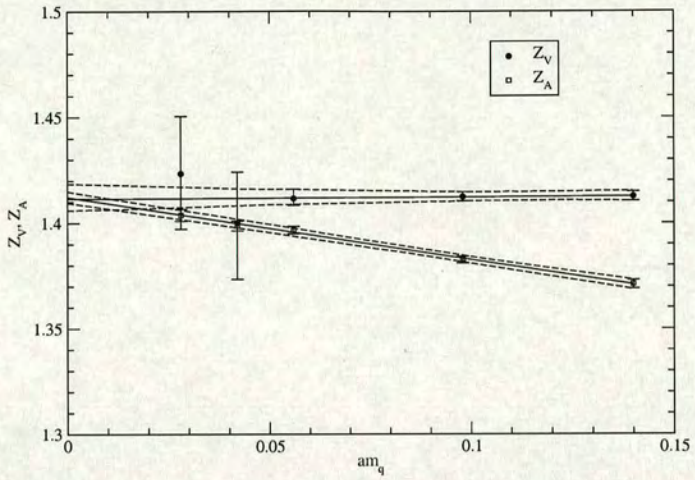

Figure 8.20: Chiral extrapolation of Z_A and Z_V for $\beta = 8.45$.

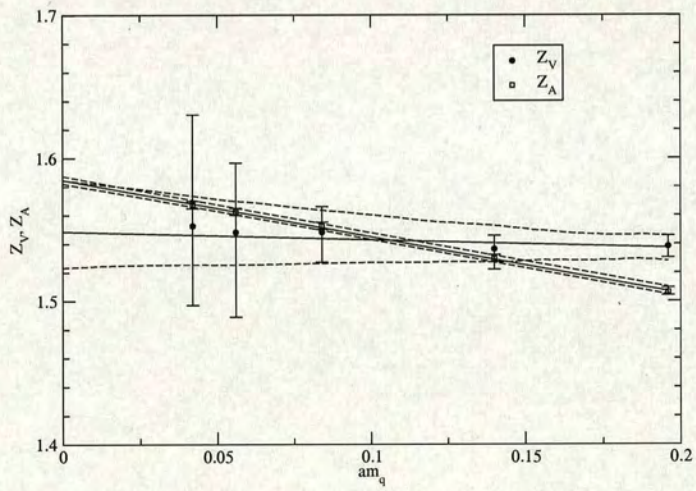

Figure 8.21: Chiral extrapolation of Z_A and Z_V for $\beta = 8.00$.

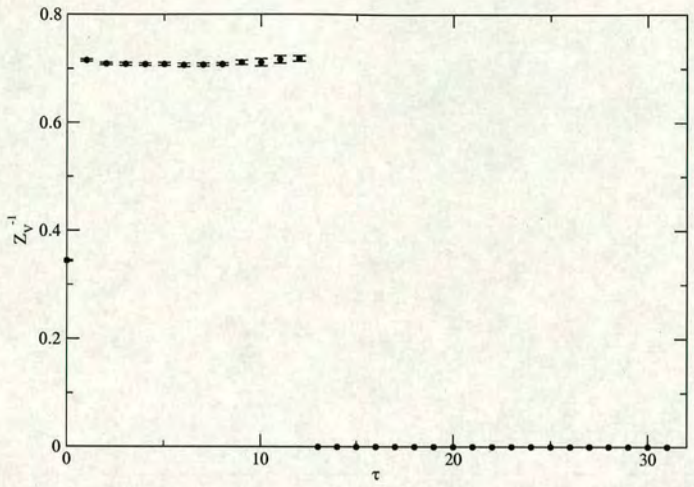

Figure 8.22: $Z_V^{-1}(\tau)$ for $a\mu = 0.035$ and $\beta = 8.45$.

8.2.3 Perturbative constants

While the axial and vector renormalization constants allow us to measure both the meson decay constants as well as the moment a_0, we still need renormalization constants for moments $v_{2,b}$, a_1, and h_1. The local tensor renormalization constant Z_T needed for h_1 is given in [62]. At present there is no calculation for Z_{a_1}, however this is equivalent to the renormalization constant of $Z_{v_{2,a}}$ by exactly the same reasoning that leads to $Z_A = Z_V$. Hence we use $Z_{v_{2,a}}$ to renormalize a_1. This factor along with $Z_{v_{2,b}}$ can be found in [63]. In all cases, the renormalization constants are calculated at the scale $\mu = 1/a$. In order to compare measurements made at two different scales we must transform these coefficients using (6.37). As Wilson coefficients and many experimental measurements are made at $\mu = 2\ GeV$, we choose this as our scale. Note this rescaling is not required for Z_A and Z_V as they are derived

Ensemble	$\mathcal{O}$	$Z_{\mathcal{O}}(1/a)$	$\Delta Z_{\mathcal{O}}^{-1}(1/a)$	$\Delta Z_{\mathcal{O}}^{-1}(2GeV)$	$Z_{\mathcal{O}}(2GeV)$
$\beta = 8.45$	T	1.439	0.918^{+1}_{-1}	0.920^{+1}_{-1}	1.442^{+2}_{-2}
	$v_{2,a}$	1.411	0.729^{+3}_{-3}	0.732^{+9}_{-9}	1.417^{+18}_{-18}
	$v_{2,b}$	1.401	0.729^{+3}_{-3}	0.732^{+9}_{-9}	1.407^{+18}_{-18}
$\beta = 8.00$	T	1.611	0.943^{+1}_{-1}	0.920^{+1}_{-1}	1.615^{+2}_{-2}
	$v_{2,a}$	1.412	0.772^{+3}_{-3}	0.732^{+9}_{-9}	1.344^{+18}_{-18}
	$v_{2,b}$	1.402	0.772^{+3}_{-3}	0.732^{+9}_{-9}	1.329^{+18}_{-18}

Table 8.11: Perturbative renormalization constants along with scaling parameters.

from conserved quantities which are independent of the renormalization scale. The factors $\Delta Z_{\mathcal{O}}^{-1}$ needed to scale the operators can be found in [49, 78]. As these factors are calculated in the continuum, the scaling for $v_{2,a}$ and $v_{2,b}$ is the same. The values of all relevant perturbative renormalization constants are summarized in Table 8.11.

8.3 Decay constants

8.3.1 f_π

The expression for calculating f_π is given in Section 4.4. As this quantity is derived from a matrix element of the local axial current it must be renormalized using Z_A. While we could fit the bare f_π and then multiply this by the Z_A found in the previous section, these expressions have common factors which cancel. We therefore can combine our expressions for Z_A (8.5) and

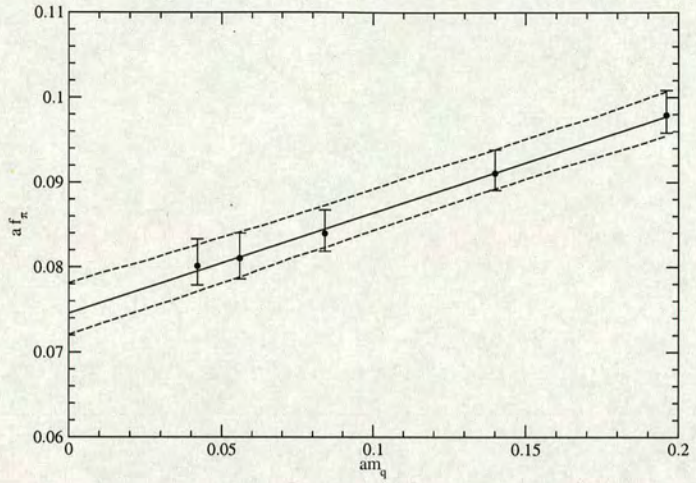

Figure 8.23: Chiral extrapolation of f_π for $\beta = 8.00$.

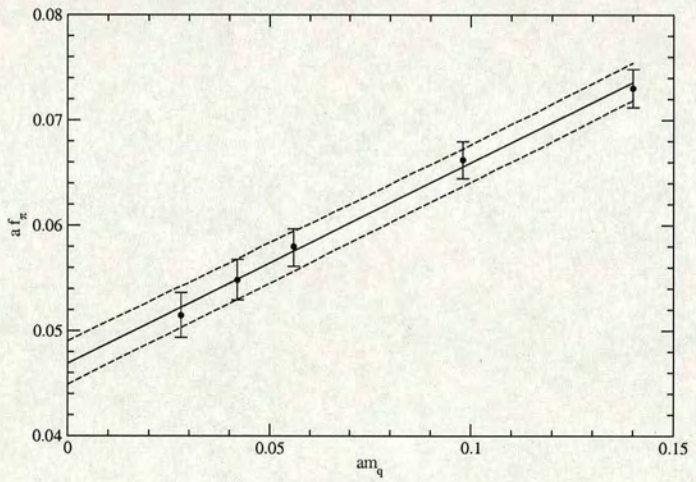

Figure 8.24: Chiral extrapolation of f_π for $\beta = 8.45$.

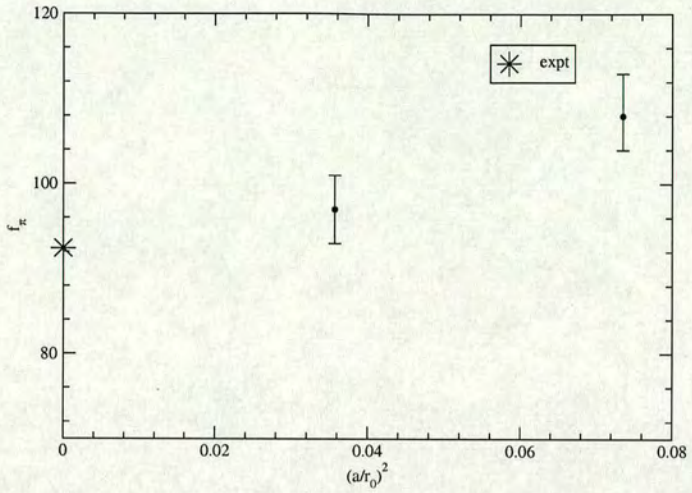

Figure 8.25: Continuum extrapolation of f_π.

Ensemble	am_q	af_π	$f_\pi[MeV]$
$\beta = 8.45$	0.028	0.0515^{+22}_{-21}	107^{+5}_{-4}
	0.042	0.0548^{+19}_{-19}	114^{+4}_{-4}
	0.056	0.0580^{+17}_{-19}	120^{+4}_{-4}
	0.098	0.0662^{+17}_{-18}	137^{+4}_{-4}
	0.140	0.0730^{+18}_{-18}	152^{+4}_{-4}
$\beta = 8.00$	0.042	0.0788^{+43}_{-30}	114^{+6}_{-4}
	0.056	0.0799^{+38}_{-29}	116^{+6}_{-4}
	0.084	0.0831^{+34}_{-30}	121^{+5}_{-4}
	0.140	0.0906^{+33}_{-32}	131^{+5}_{-5}
	0.196	0.0974^{+34}_{-31}	141^{+5}_{-4}

Table 8.12: Fitted values of renormalized f_π.

the bare f_π (4.29) and fit the renormalized decay constant in one fit. The renormalized f_π is then given by

$$f_\pi = \frac{2m_q}{m_\pi^{3/2}} \frac{A_{PP}^{LS}}{\sqrt{A_{PP}^{SS}}}. \tag{8.7}$$

The fitted values are given in Table 8.12. In quenched QCD, to one loop we do not expect to see any chiral logs in f_π [79], so we form linear chiral extrapolations. These are shown in Figures 8.23, 8.24. The values of f_π in the chiral limit are given in Table 8.12. The continuum scaling is shown in Figure 8.25. The scaling with the lattice spacing is again relatively small as the numbers differ by only a few MeV. The $\beta = 8.00$ number seems a little high, however the $\beta = 8.45$ number agrees with experiment within errors and the scaling seems to be heading towards the experimental value.

Ensemble	af_π	$f_\pi[MeV]$
$\beta = 8.45$	0.0469^{+21}_{-20}	97^{+4}_{-4}
$\beta = 8.00$	0.0746^{+36}_{-25}	108^{+5}_{-4}

Table 8.13: f_π extrapolated to the chiral limit.

8.3.2 f_ρ

While the ρ meson decays strongly to 2 pions, it also can decay leptonically. As the quenched ρ meson is stable and the strong decay does not occur, we can measure this leptonic decay on the lattice. The leptonic decay constant f_ρ is measured from vector correlators using

$$\frac{1}{f_\rho^{bare}} = \sqrt{\left(\frac{2}{3m_\rho^3}\right)} \frac{\sum_k A_{V_k V_k}^{LS}}{\sqrt{\sum_k A_{V_k V_k}^{SS}}}. \tag{8.8}$$

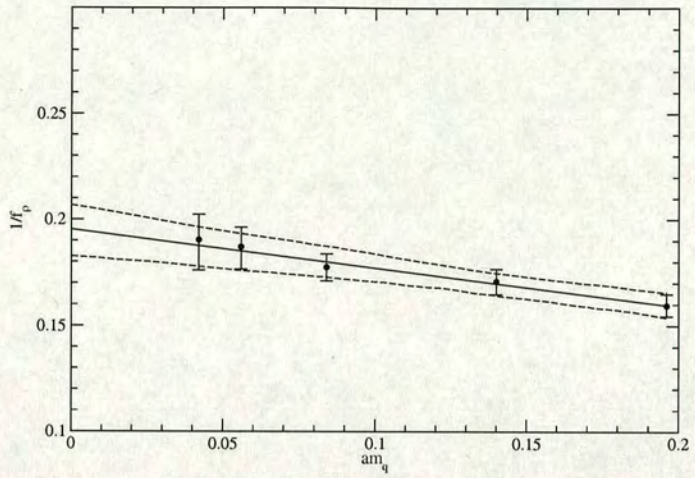

Figure 8.26: Chiral extrapolation of the bare value of $1/f_\rho$ for $\beta = 8.00$.

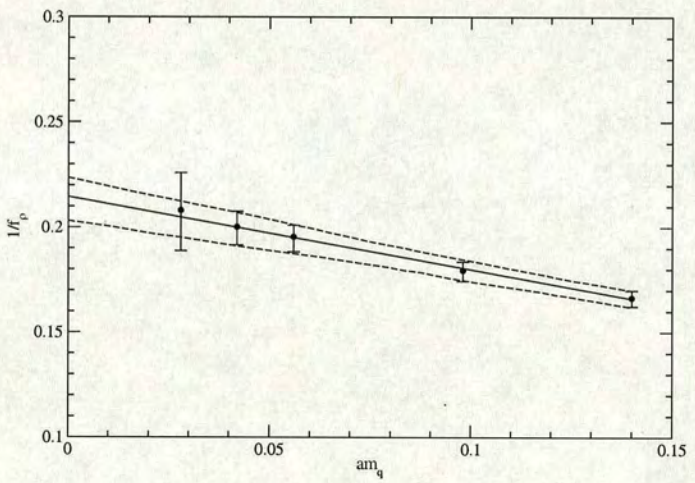

Figure 8.27: Chiral extrapolation of the bare value of $1/f_\rho$ for $\beta = 8.45$.

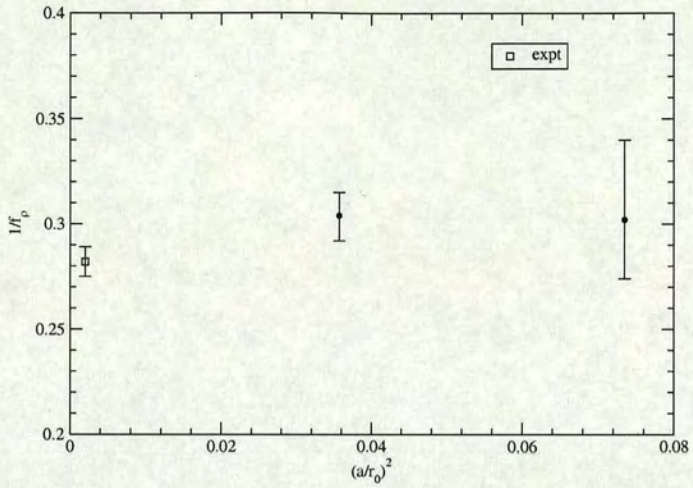

Figure 8.28: Continuum extrapolation of $1/f_\rho$.

Ensemble	am_q	af_ρ
$\beta = 8.45$	0.028	0.208^{+18}_{-19}
	0.042	0.200^{+7}_{-9}
	0.056	0.196^{+6}_{-7}
	0.098	0.179^{+4}_{-5}
	0.140	0.166^{+4}_{-4}
$\beta = 8.00$	0.042	0.190^{+12}_{-14}
	0.056	0.187^{+9}_{-11}
	0.084	0.178^{+6}_{-6}
	0.140	0.171^{+6}_{-6}
	0.196	0.160^{+5}_{-5}

Table 8.14: Fitted values of bare $1/f_\rho$.

f_ρ^{bare} must be renormalized using the Z_V calculated earlier. The fitted values of $1/f_\rho^{bare}$ are shown in Table 8.14, while the chiral extrapolations are shown in Figures 8.26, 8.27. The chiral extrapolated values along with the renormalized results are shown in Table 8.15. The renormalized results are compared with the experimental value [80, 81] in Figure 8.28. There seems to be good agreement with the experimental result and very little scaling, although there is a large error from Z_V in the $\beta = 8.00$ measurement. If the value of Z_A was used instead, this would raise this number up to around 0.310, which while larger would still indicate small scaling which is towards the experimental value.

Ensemble	$1/f_\rho^{bare}$	Z_V	$1/f_\rho^{ren}$
$\beta = 8.45$	0.215^{+9}_{-11}	1.412^{+7}_{-5}	0.304^{+11}_{-12}
$\beta = 8.00$	0.195^{+11}_{-13}	1.549^{+36}_{-25}	0.302^{+38}_{-28}

Table 8.15: $1/f_\rho$ extrapolated to the chiral limit.

8.4 Low moments of nucleon structure functions

In this section we give results for moments of nucleon structure functions. We first look at $v_{2,b}$ which is related to the first moment of the unpolarized structure function F_1. We measure the polarized matrix elements a_0 and a_1 which correspond to the zeroth and first moments of the polarized structure function g_1. We also give results for the tensor structure function h_1. The

physical interpretation of these quantities was discussed in Section 2.3.

8.4.1 $v_{2,b}$

We calculate the matrix element $v_{2,b}$ given in Table 5.1. This describes the momentum distribution of the constituent partons and is related to the first moment of F_1. As we cannot measure the disconnected contributions, we restrict ourselves to the non-singlet operator. We extract the value of $v_{2,b}$ by fitting to a plateau between the nucleon source and sink of the ratio of three point to two point correlation functions. As we go to progressively lighter quark masses, fluctuations begin to set in which disrupt the plateaus and make fitting difficult. This is especially problematic for the $\beta = 8.45$ set. We would expect coarser lattices to give noisier results, but the effect is compounded here due to the lower level of statistics on this set. As a result of these fluctuations we see large errors on the fits for the two lightest masses in each case. The fitted values of the bare matrix elements are give given in Table 8.16. The expected form of the chiral extrapolation from Qχpt [82] is given by

$$v_{2,b} = Am_\pi^2 + B(1 - Cm_\pi^2 \log \frac{m_\pi^2}{\Lambda_\chi^2}), \tag{8.9}$$

however as we have seen no real evidence of deviations due to chiral logs up to this point, and since we are unable to accurately extract the values at the lightest quark masses, we restrict ourselves to linear extrapolations in the quark mass. The fits are shown in Figures 8.29, 8.30. The data seems to be reasonably well described by a linear fit, and in both cases there seems to be very little dependence on the quark mass. As mentioned the two lightest masses have very large errors and so contribute very little to the

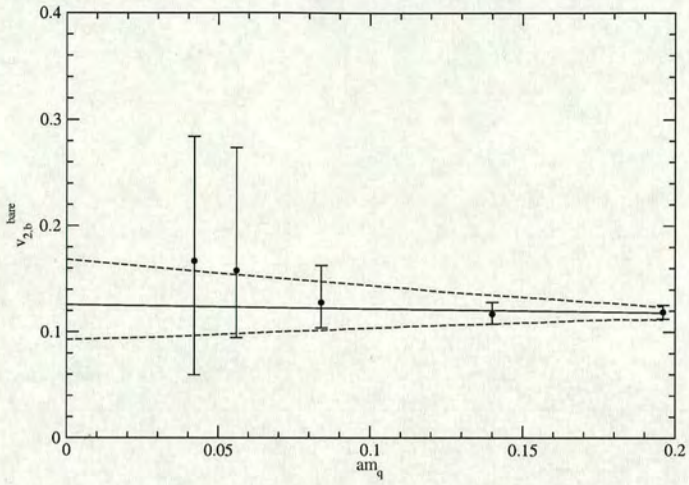

Figure 8.29: Chiral extrapolation of bare $v_{2,b}$ for $\beta = 8.00$.

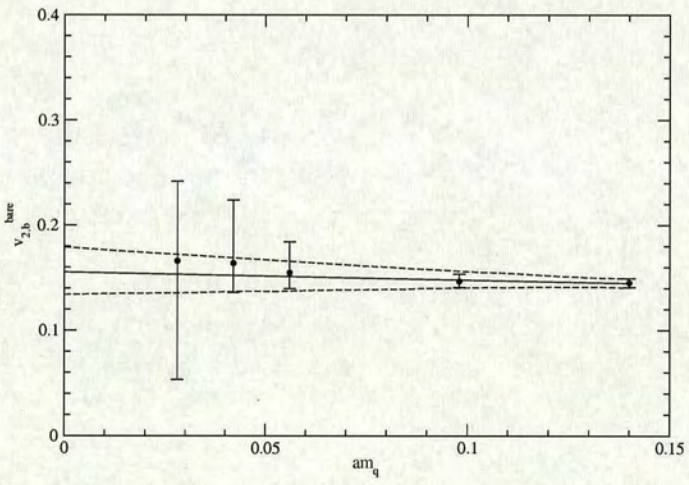

Figure 8.30: Chiral extrapolation of bare $v_{2,b}$ for $\beta = 8.45$.

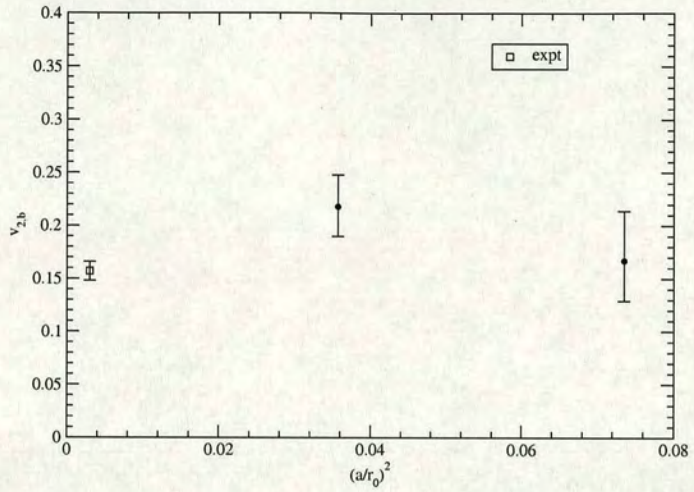

Figure 8.31: Continuum extrapolation of $v_{2,b}^{\overline{MS}}$ at 2 GeV.

Ensemble	am_q	$v_{2,b}^{bare}$
$\beta = 8.45$	0.028	0.166^{+76}_{-113}
	0.042	0.164^{+60}_{-28}
	0.056	0.155^{+29}_{-15}
	0.098	0.147^{+7}_{-6}
	0.140	0.145^{+4}_{-4}
$\beta = 8.00$	0.042	0.167^{+117}_{-107}
	0.056	0.158^{+116}_{-63}
	0.084	0.128^{+35}_{-24}
	0.140	0.117^{+11}_{-9}
	0.196	0.119^{+6}_{-6}

Table 8.16: Fitted values of bare $v_{2,b}$.

fit. The values extrapolated to the chiral limit along with the renormalized matrix elements in the $\overline{MS}$ scheme at $2\,GeV$ are shown in Table 8.17. The renormalized results are shown against the experimental value [83] in Figure 8.31.

The results from lattice simulations for v_2 have always been too large by over 50%. This discrepancy is found whether the data is quenched or dynamical [84]. Recent results using quenched domain wall fermions [85], and dynamical Wilson fermions [49] both exhibit this problem. The results here do not show nearly as large a discrepancy, however the improvement when compared to experiment may be attributable to the fact that we are using perturbative renormalization constants. If we compare the perturbative Z_A and Z_V values to the non-perturbative values calculated here, the perturbative values are lower. For Z_A, the $\beta = 8.45$ perturbative number is 1.303 compared to the non-perturbative 1.411, which is an increase of around 10%. For the coarser $\beta = 8.00$ set, the value is lower by around $15 - 20\%$. If we had similar scalings for v_2, then both values would sit well above the experimental value. The median values would still be lower than the values quoted in [85, 49], although admittedly with larger errors. Thus while these results are encouraging, until non-perturbative Zs are calculated then we cannot be certain that we have greater agreement with experiment.

Ensemble	$v_{2,b}^{bare}$	$Z_{v_{2,b}}^{\overline{MS}}(2\,GeV)$	$v_{2,b}^{\overline{MS}}(2\,GeV)$
$\beta = 8.45$	0.155^{+24}_{-21}	1.407^{+18}_{-18}	0.218^{+30}_{-28}
$\beta = 8.00$	0.126^{+43}_{-33}	1.329^{+18}_{-18}	0.167^{+47}_{-38}

Table 8.17: $v_{2,b}$ extrapolated to the chiral limit.

8.4.2 g_A

The matrix element a_0 corresponding to the lowest moment of the polarized structure function g_1 can be used to determine the axial charge of the nucleon g_A, which describes the β decay of the nucleon as discussed in Section 2.3.1. The measured operator is given in Table 5.1.

For the $\beta = 8.45$ set we get quite a nice signal. As expected, the $\beta = 8.00$ set is much noisier, and the signal here is particularly poor. The plateaus are much less stable and so the fits come with greater errors. The bare results are shown in Table 8.18. The chiral extrapolations of the bare numbers are shown in Figures 8.32, 8.33. As with $v_{2,b}$ we see very little mass dependence and linear behaviour. That said, in both cases there is a small amount of upward curvature. The origin of this is seen in the form of the plateaus, which seem to round out and bulge as we go lighter (see Figure 8.34). This leads to a slightly larger plateau fit.

As g_A is renormalized using Z_A, we can use the non-perturbative value and avoid the ambiguity we had with $v_{2,b}$. We give the renormalized values in Table 8.19. These results are plotted along with the experimental result [86] $g_A = 1.26.$ in Figure 8.35. In both cases we find very good agreement with experiment. Historically lattice simulations have underestimated this value by $10 - 20\%$, regardless of whether the measurements are made on quenched or dynamical data [87]. It should be noted that most of these simulations were carried out with actions which explicitly break chiral symmetry. Measurements using domain wall fermions which have approximate chiral symmetry find much closer agreement [88]. Thus as we are using a formulation which preserves chiral symmetry, and hence have an exact rela-

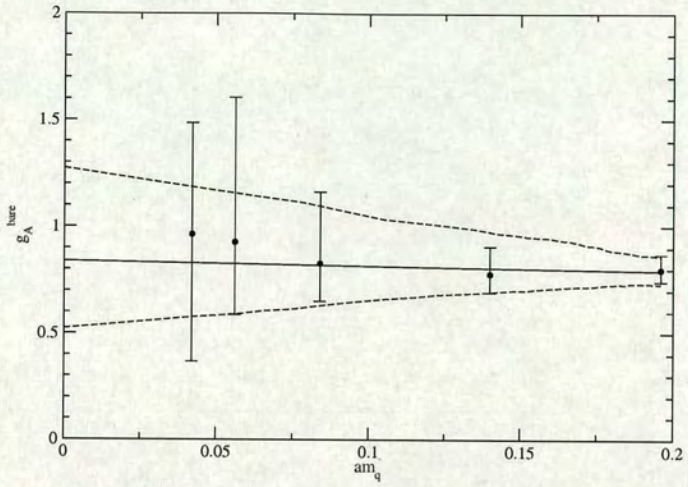

Figure 8.32: Chiral extrapolation of bare g_A at $\beta = 8.00$.

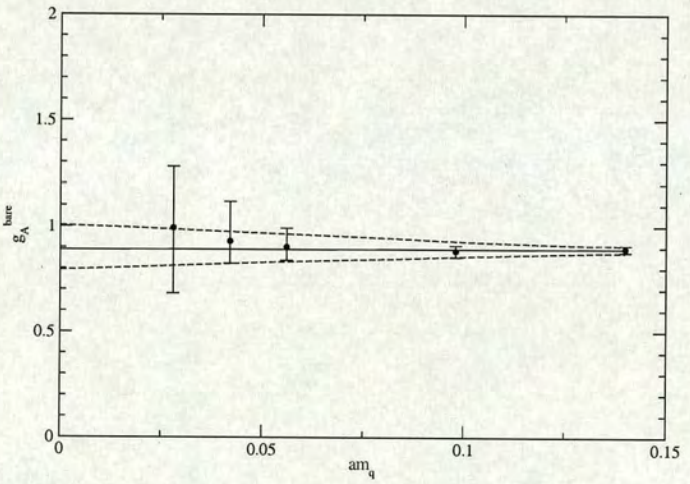

Figure 8.33: Chiral extrapolation of bare g_A for $\beta = 8.45$.

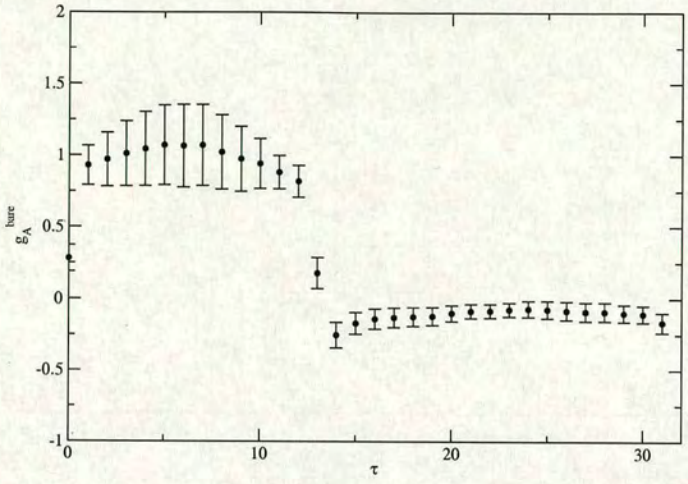

Figure 8.34: Bare g_A at $\beta = 8.45$ and $am_q = 0.042$.

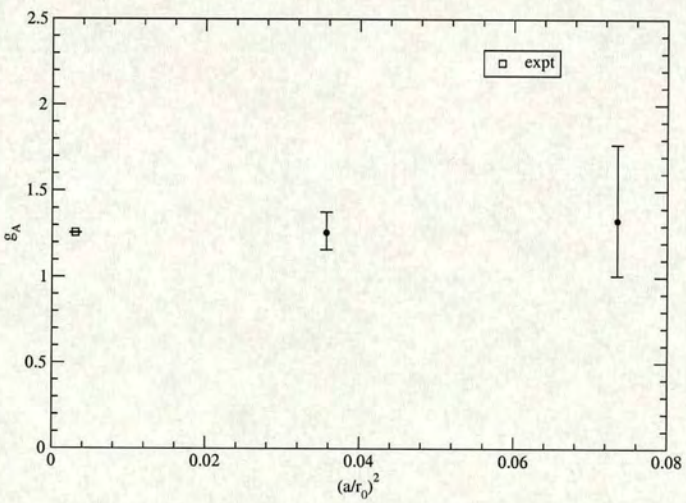

Figure 8.35: Continuum extrapolation of g_A.

Ensemble	am_q	g_A^{bare}
$\beta = 8.45$	0.028	0.99^{+29}_{-31}
	0.042	0.93^{+19}_{-11}
	0.056	0.90^{+9}_{-6}
	0.098	0.88^{+3}_{-3}
	0.140	0.90^{+2}_{-2}
$\beta = 8.00$	0.042	0.96^{+52}_{-60}
	0.056	0.93^{+68}_{-34}
	0.084	0.83^{+33}_{-18}
	0.140	0.77^{+13}_{-8}
	0.196	0.80^{+7}_{-6}

Table 8.18: Fitted values of bare g_A.

Ensemble	g_A^{bare}	Z_A	g_A^{ren}
$\beta = 8.45$	0.89^{+12}_{-10}	1.412^{+3}_{-3}	1.26^{+12}_{-10}
$\beta = 8.00$	0.84^{+44}_{-32}	1.585^{+3}_{-3}	1.33^{+44}_{-32}

Table 8.19: Renormalized g_A extrapolated to the chiral limit.

tion to extract Z_A, it is perhaps not surprising that this quantity should give good agreement.

8.4.3 a_1

The first moment of the polarized structure function g_1 describes the helicity distribution of the nucleon. We measure the zero momentum operator $a_{1,b}$ given in Table 5.1.

The signal here is the worst of the three point functions measured. The $\beta = 8.45$ plateaus were still relatively good, but the $\beta = 8.00$ set was very hard to fit due to a nasty kink in the plateau which grew as the quark mass got lighter. This reduced the possible fit range and so made the errors even larger than they would have been through normal fluctuations. The fitted values of the bare matrix element are given in Table 8.21. The chiral extrapolations are shown in Figures 8.36, 8.37. In both cases we see as previously that there is very little mass dependence.

Due to chiral symmetry we can renormalize the bare matrix element using $Z_{v_{2,a}}$. The renormalized results are given in Table 8.20. The results are plotted against the experimental value of 0.196^{+4}_{-4} [84]. The results are very similar to those of $v_{2,b}$, with the $\beta = 8.45$ number sitting slightly above the physical value, while the $\beta = 8.00$ result sits much lower. Again the Z's must be treated with caution, especially in the coarser set, however a naive ratio of $v_{2,b}$ and $a_{1,b}$ (which should be independent of the Zs) seems to give good agreement with the experimental value (Figure 8.39).

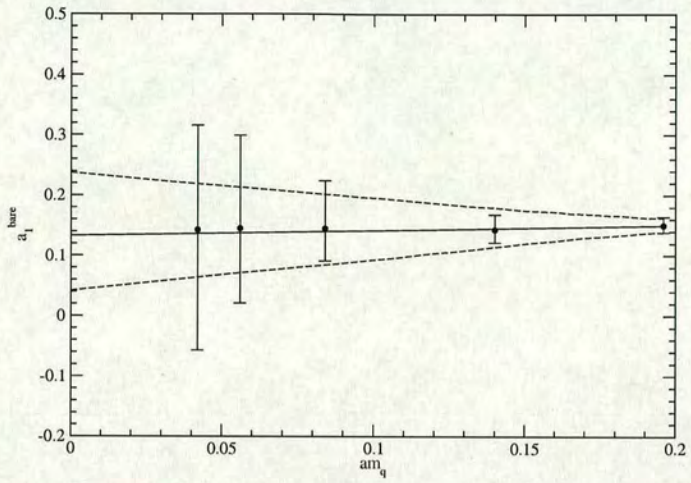

Figure 8.36: Chiral extrapolation of bare $a_{1,b}$ at $\beta = 8.00$.

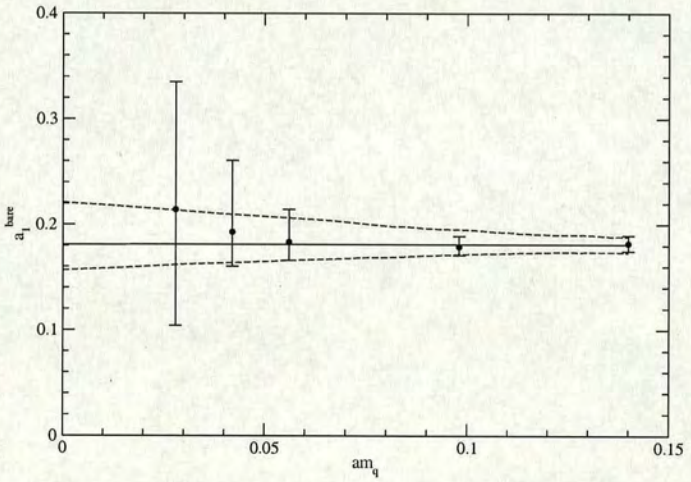

Figure 8.37: Chiral extrapolation of bare $a_{1,b}$ for $\beta = 8.45$.

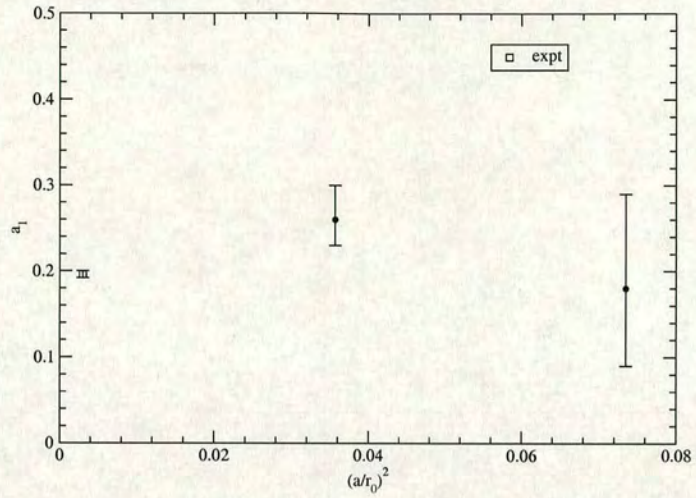

Figure 8.38: Continuum extrapolation of $a_1^{\overline{MS}}(2\,GeV)$.

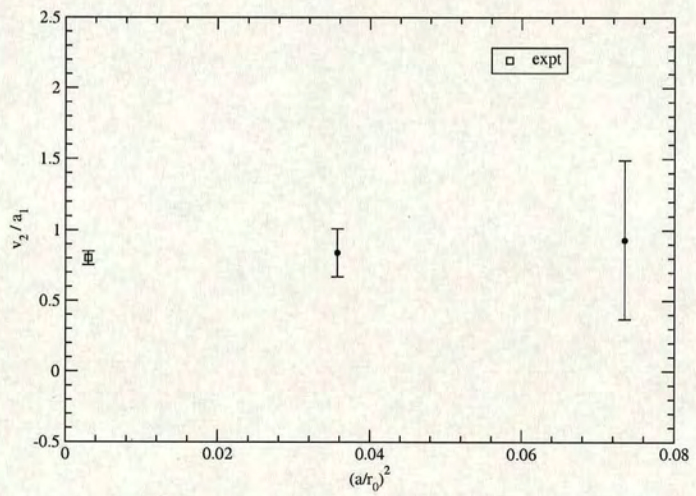

Figure 8.39: Naive ratio of v_2/a_1 in the chiral limit.

Ensemble	a_1^{bare}	$Z_{v_{2,a}}^{\overline{MS}}(2\,GeV)$	$a_1^{\overline{MS}}(2\,GeV)$
$\beta = 8.45$	0.181^{+40}_{-24}	1.417^{+18}_{-18}	0.26^{+4}_{-3}
$\beta = 8.00$	0.133^{+105}_{-91}	1.344^{+18}_{-18}	0.18^{+11}_{-9}

Table 8.20: Renormalized a_1 extrapolated to the chiral limit.

Ensemble	am_q	$a_{1,b}^{bare}$
$\beta = 8.45$	0.028	0.214^{+121}_{-110}
	0.042	0.193^{+68}_{-33}
	0.056	0.184^{+31}_{-17}
	0.098	0.179^{+10}_{-8}
	0.140	0.182^{+8}_{-7}
$\beta = 8.00$	0.042	0.143^{+173}_{-200}
	0.056	0.145^{+154}_{-124}
	0.084	0.145^{+79}_{-54}
	0.140	0.143^{+25}_{-21}
	0.196	0.150^{+14}_{-12}

Table 8.21: Fitted values of bare $a_{1,b}$.

8.4.4 h_1

Here we determine the lowest moment of the transverse structure function h_1 measurable in Drell-Yan processes. This moment defines a tensor charge of the nucleon analogous to the axial charge g_A. The signal is reasonably good for the $\beta = 8.45$ set, but the $\beta = 8.00$ results again show kinks in the plateau. We give the fitted values in Table 8.23. The chiral extrapolations are shown in Figures 8.40, 8.41. As with other structure functions we see very little mass dependence and nothing to suggest deviation from linear behaviour. The matrix element is renormalized using the perturbative Z_T. In order to non-perturbatively improve the values we follow the method of [89] and scale the value by the ratio of non-perturbative and perturbative axial renormalization constants Z_A^{NP}/Z_A^{PT}. This should help correct for the underestimation in the perturbative expansion. Note that this method is not applicable to the previous measured quantities. To non-perturbatively improve v_2 and a_1 in a similar fashion we would need a non-perturbative value of an operator with a derivative term. The improved Z_T is shown in Table 8.11. The renormalized values are given in Table 8.22 and shown in Figure 8.42. An experimental value for this quantity is not yet known, however the values calculated here are consistent with other determinations [90, 85].

Ensemble	h_1^{bare}	$Z_T^{\overline{MS}}(2\,GeV)$	$h_1^{\overline{MS}}(2\,GeV)$
$\beta = 8.45$	0.96^{+12}_{-10}	1.442^{+2}_{-2}	1.38^{+17}_{-13}
$\beta = 8.00$	0.79^{+48}_{-38}	1.615^{+2}_{-2}	1.28^{+77}_{-61}

Table 8.22: Renormalized h_1 extrapolated to the chiral limit.

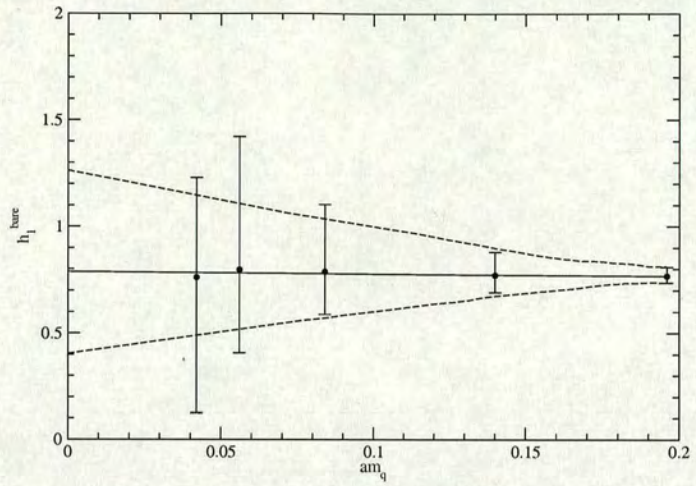

Figure 8.40: Chiral extrapolation of bare $h_{1,b}$ at $\beta = 8.00$.

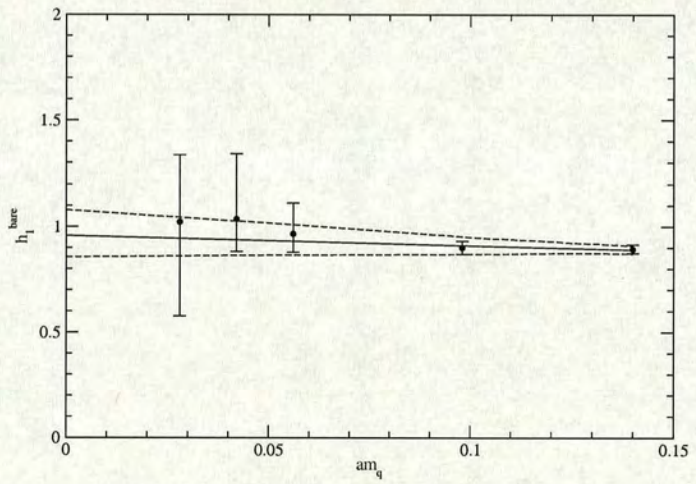

Figure 8.41: Chiral extrapolation of bare $a_{1,b}$ for $\beta = 8.45$.

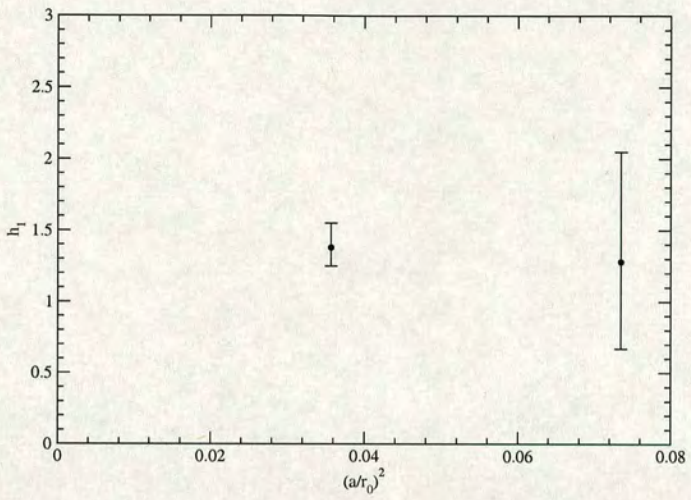

Figure 8.42: Continuum extrapolation of h_1.

Ensemble	am_q	$h_{1,b}^{bare}$
$\beta = 8.45$	0.028	1.02^{+31}_{-44}
	0.042	1.04^{+31}_{-15}
	0.056	0.97^{+15}_{-9}
	0.098	0.90^{+3}_{-3}
	0.140	0.89^{+2}_{-2}
$\beta = 8.00$	0.042	0.76^{+47}_{-64}
	0.056	0.80^{+62}_{-39}
	0.084	0.79^{+32}_{-20}
	0.140	0.77^{+11}_{-8}
	0.196	0.77^{+4}_{-3}

Table 8.23: Fitted values of bare $h_{1,b}$.

Chapter 9

Summary

In this thesis we presented the results of a lattice calculation using overlap fermions. This fermion formulation preserves an on-shell chiral symmetry and so is well suited for simulating quark masses close to the chiral limit. The simulation was carried out in the quenched approximation using the Lüscher-Weisz gauge action.

After some introductory theory and lattice methodology we first investigated the locality of the overlap Dirac operator on improved gauge fields. We found that the non-locality of the operator fell off exponentially, and was fairly insensitive to the underlying gauge action. We did however find that the operator has a much larger condition number on unimproved Wilson gauge fields than on Lüscher-Weisz, and hence the use of improved gauge actions can provide significant savings in inversion time. Also we found that while any physical quantities we measure should not depend on the auxiliary mass parameter ρ, both the locality and condition number of the Dirac operator are dependent on this parameter. Thus we can vary ρ in order to find

an optimal value.

The main results section included a selection of measurements of light hadron phenomenology including some low lying hadron masses, non-perturbative renormalization constants, meson decay constants, and low moments of nucleon structure functions. The measurements were made on 5 masses in order to extrapolate to the chiral limit. In order to investigate the scaling of the results with the lattice size, we repeated the calculation on a second, coarser lattice, although on a smaller number of configurations.

We first measured the masses of the nucleon and the pseudoscalar and vector mesons. One of the advantages of the overlap formalism is it allows the simulation of light quark masses, and here our lightest quarks correspond to pions of around 400MeV. At this level one might have hoped to have seen some indications that we were entering the chiral regime by seeing the effects of chiral logs in the extrapolations. In the pion extrapolation, a small amount of non-linearity could be detected, and a value for the chiral log parameter δ was extracted. The signal was not very strong however, and the non-linearity was very close to zero. A linear extrapolation was found to go through zero as predicted by the axial Ward identity. Thus extrapolations in $am_\pi{}^2$ and am_q were equivalent.

The nucleon and rho mass were extracted and both were found to lie about 10% above their physical values, but within the range of uncertainty caused by the quenched approximation. The mass extrapolations were found to be linear and fit functions from Qχpt were unstable, with no apparent curvature in the mass range considered. There was also very little scaling violation between the two data sets with both values for each quantity agreeing within

errors.

The axial and vector current renormalization constants were calculated and found to agree as expected from chiral symmetry. These values were used to provide results for the pseudoscalar and vector decay constants. For the $\beta = 8.45$ set we find good agreement with measured values although the $\beta = 8.00$ number seems a little high.

The nucleon matrix element v_2, which is related to the momentum distribution of constituent partons was extracted. It was found to lie above the physical value, but the discrepancy was not as large as in previous measurements. However the Z used was perturbative and hence may be underestimated. As we would expect perturbation theory to be worse at stronger coupling, this effect would be increased for the coarser lattice and is the most likely explanation for the lower value of the $\beta = 8.00$ measurement.

The axial charge of the nucleon was measured and gave very good agreement with experiment. This is a measurement that is generally lower than physical values, however as it is extracted from an axial current, chiral symmetry breaking would seem the most likely reason for previous underestimates. The tensor charge was also measured and found to agree with previous determinations.

The matrix element a_1 which determines the helicity distribution of the nucleon's constituent partons was measured. The results showed qualitatively the same behaviour as for the vector operator matrix element v_2, to which a_1 is related to through a chiral transformation. Its value sits slightly above the physical value, with similar differences in the measurements at the two lattice spacing, most likely due to the renormalization constants. The

ratio of both measurements which should be independent of the renormalization showed reasonably good agreement with experiment.

In all cases, the improved operators used to measure matrix elements gave as expected very little mass dependence. None of the chiral extrapolations gave any indications of chiral logs, and all were well described by linear fits. The coarser lattice results were much noisier than expected. Although there was a smaller number of configurations, this would only contribute an approximately $20 - 30\%$ increase in error bars. However due to increased fluctuations and rougher plateaus, the errors became much larger. Due to the more poorly conditioned system, the inversions also took much longer than on the finer lattice ensemble at equivalent quark masses. Despite the larger than expected errors on the coarser lattice results, we did not see any significant scaling violations due to the lattice spacing.

With regards to further progress, no tests of any volume dependence have been shown here. While it is unlikely that these effects would be large, it should still be checked by running on a larger volume. Also a third lattice spacing would allow a continuum limit to be taken. An increase in statistics would also help reduce the error bars. Work is progressing on all of these issues and results should be published soon [91, 92].

A further concern is the reliability of perturbative renormalization for overlap fermions. The renormalization constants in the overlap formulation are very large compared to other formulations. The reason for this is not really understood. However as the values are far away from 1, it is unclear how well perturbation theory will work. Non-perturbative renormalization would clearly be preferable, and progress is being made in this direction, but

it seems that reliable values are harder to extract than in other formulations.

Finally, dynamical simulations are clearly preferred, and with the new QCDOC 10-Teraflop machine [93] now operational, dynamical configurations using chirally symmetric actions are now being generated.

Chapter 10

Appendix

10.1 Gamma matrix conventions

In Minkowski ($\mathcal{M}$) space we have the metric $g_{\mu\nu}$ which has the signature $(1,-1,-1,-1)$. The Minkowski space γ matrices satisfy

$$\{\gamma_\mu^{(\mathcal{M})}, \gamma_\nu^{(\mathcal{M})}\} = 2g_{\mu\nu}. \tag{10.1}$$

In Euclidean (E) space, we have the flat metric $\delta_{\mu\nu}$ with signature $(1,1,1,1)$. Thus the Euclidean γ matrices satisfy

$$\{\gamma_\mu^{(E)}, \gamma_\nu^{(E)}\} = 2\delta_{\mu\nu}. \tag{10.2}$$

The two sets of matrices can then be related by

$$\gamma_i^{(E)} \equiv -i\gamma_i^{(\mathcal{M})}, \qquad \gamma_4^{(E)} \equiv \gamma_0^{(\mathcal{M})}. \tag{10.3}$$

Here we use a chiral basis

$$\gamma_i^{(E)} = (-1)^{i+1} i \begin{pmatrix} 0 & \sigma_i \\ -\sigma_i & 0 \end{pmatrix}, \qquad \gamma_4^{(E)} = \begin{pmatrix} 0 & I \\ I & 0 \end{pmatrix}, \tag{10.4}$$

$$\tag{10.5}$$

with the σ_i given by

$$\sigma_1 = \begin{pmatrix} 0 & 1 \\ 1 & 0 \end{pmatrix}, \quad \sigma_2 = \begin{pmatrix} 0 & -i \\ i & 0 \end{pmatrix}, \quad \sigma_3 = \begin{pmatrix} 1 & 0 \\ 0 & -1 \end{pmatrix}. \tag{10.6}$$

$\gamma_5^{(E)}$ is defined as

$$\gamma_5^{(E)} \equiv \gamma_1^{(E)}\gamma_2^{(E)}\gamma_3^{(E)}\gamma_4^{(E)} = \begin{pmatrix} I & 0 \\ 0 & -I \end{pmatrix} \tag{10.7}$$

The discrete charge conjugation matrix C is given by

$$C \equiv \gamma_4^{(E)}\gamma_2^{(E)}. \tag{10.8}$$

Bibliography

[1] H. David Politzer. Reliable perturbative results for strong interactions? *Phys. Rev. Lett.*, 30:1346–1349, 1973.

[2] D. J. Gross and Frank Wilczek. Ultraviolet behavior of non-abelian gauge theories. *Phys. Rev. Lett.*, 30:1343–1346, 1973.

[3] Paul H. Ginsparg and Kenneth G. Wilson. A remnant of chiral symmetry on the lattice. *Phys. Rev.*, D25:2649, 1982.

[4] Herbert Neuberger. Exactly massless quarks on the lattice. *Phys. Lett.*, B417:141–144, 1998.

[5] Shi-Lin Zhu. Theoretical development on pentaquarks. 2004.

[6] R. L. Jaffe. Exotica. 2004.

[7] B. R. Martin and G. Shaw. Particle physics. *Wiley*, 1999.

[8] M. E. Peskin and D. V. Schroeder. An introduction to quantum field theory. *Addison-Wesley*, 1995.

[9] Aneesh V. Manohar. An introduction to spin dependent deep inelastic scattering. 1992.

[10] D. J. Gross C. G. Callan. *Phys. Rev. Lett*, 22, 1969.

[11] R. L. Jaffe and Xiang-Dong Ji. Chiral odd parton distributions and drell-yan processes. *Nucl. Phys.*, B375:527–560, 1992.

[12] J. D. Bjorken and Emmanuel A. Paschos. Inelastic electron proton and gamma proton scattering, and the structure of the nucleon. *Phys. Rev.*, 185:1975–1982, 1969.

[13] Kenneth G. Wilson. Nonlagrangian models of current algebra. *Phys. Rev.*, 179:1499–1512, 1969.

[14] Holger Bech Nielsen and M. Ninomiya. No go theorem for regularizing chiral fermions. *Phys. Lett.*, B105:219, 1981.

[15] K. G. Wilson. *New Phenomena In Subnuclear Physics*, Part A*:13–32, New York 1977.

[16] I. Montvay and G. Munster. Quantum fields on a lattice. *Cambridge University Press*, 1994.

[17] Martin Luscher. Exact chiral symmetry on the lattice and the ginsparg-wilson relation. *Phys. Lett.*, B428:342–345, 1998.

[18] Robert G. Edwards, Urs M. Heller, and Rajamani Narayanan. A study of practical implementations of the overlap-dirac operator in four dimensions. *Nucl. Phys.*, B540:457–471, 1999.

[19] M. R. Hestenes and E. Stiefel. *J. Res. Nat. Bur. STandards*, 49.

[20] Beat Jegerlehner. Krylov space solvers for shifted linear systems. 1996.

[21] A. D. Kennedy. Approximation theory for matrices. *Nucl. Phys. Proc. Suppl.*, 128C:107–116, 2004.

[22] E. Y. Remez. General computational methods of chebyshev approximation. (US Atomic Energy Commision, 1962).

[23] E. I. Zolotarev. Zap. imp. akad. nauk st. petersburg. 30:5, 1877.

[24] A. D. Kennedy. Fast evaluation of zolotarev coefficients. 2004.

[25] Andreas Frommer, Bertold Nockel, Stephan Gusken, Thomas Lippert, and Klaus Schilling. Many masses on one stroke: Economic computation of quark propagators. *Int. J. Mod. Phys.*, C6:627–638, 1995.

[26] H. J. Rothe. Lattice gauge theories, an introduction. *World Scientific Publishing Co. Pte. Ltd.*, 1992.

[27] A. D. Kennedy. Parallel computing 25. pages 1311–1339, 1999.

[28] Michael Creutz. Overrelaxation and monte carlo simulation. *Phys. Rev.*, D36:515, 1987.

[29] Frank R. Brown and Thomas J. Woch. Overrelaxed heat bath and metropolis algorithms for accelerating pure gauge monte carlo calculations. *Phys. Rev. Lett.*, 58:2394, 1987.

[30] S. Duane, A. D. Kennedy, B. J. Pendleton, and D. Roweth. Hybrid monte carlo. *Phys. Lett.*, B195:216–222, 1987.

[31] D. Barkai, K. J. M. Moriarty, and C. Rebbi. Hadron masses in quenched quantum chromodynamics. *Phys. Lett.*, B156:385, 1985.

[32] Steve W. Otto and John D. Stack. The su(3) heavy quark potential with high statistics. *Phys. Rev. Lett.*, 52:2328, 1984.

[33] P. de Forcrand, K. H. Mutter, K. Schilling, and R. Sommer. Towards the limit of the quenched approximation in hadron mass calculations. WU-B-86-12.

[34] M. Luscher and P. Weisz. On-shell improved lattice gauge theories. *Commun. Math. Phys.*, 97:59, 1985.

[35] G. Peter Lepage and Paul B. Mackenzie. On the viability of lattice perturbation theory. *Phys. Rev.*, D48:2250–2264, 1993.

[36] Mark G. Alford, W. Dimm, G. P. Lepage, G. Hockney, and P. B. Mackenzie. Lattice qcd on small computers. *Phys. Lett.*, B361:87–94, 1995.

[37] J. Gasser and H. Leutwyler. Chiral perturbation theory to one loop. *Ann. Phys.*, 158:142, 1984.

[38] J. Gasser and H. Leutwyler. Chiral perturbation theory: Expansions in the mass of the strange quark. *Nucl. Phys.*, B250:465, 1985.

[39] Claude W. Bernard and Maarten F. L. Golterman. Chiral perturbation theory for the quenched approximation of qcd. *Phys. Rev.*, D46:853–857, 1992.

[40] Stephen R. Sharpe. Quenched chiral logarithms. *Phys. Rev.*, D46:3146–3168, 1992.

[41] C. Bernard. Order of the chiral and continuum limits in staggered chiral perturbation theory. 2004.

[42] Stephan Durr and Christian Hoelbling. Scaling tests with dynamical overlap and rooted staggered fermions. 2004.

[43] B. L. Ioffe. Calculation of baryon masses in quantum chromodynamics. *Nucl. Phys.*, B188:317–341, 1981.

[44] F. Fucito et al. Hadron spectroscopy in lattice qcd. *Nucl. Phys.*, B210:407, 1982.

[45] Stephan Durr. Gauge action improvement and smearing. 2004.

[46] C. R. Allton et al. Gauge invariant smearing and matrix correlators using wilson fermions at beta = 6.2. *Phys. Rev.*, D47:5128–5137, 1993.

[47] D. S. Henty and R. D. Kenway. Hopping parameter expansion for heavy - light systems. *Phys. Lett.*, B289:109–114, 1992.

[48] C. Best et al. Pion and rho structure functions from lattice qcd. *Phys. Rev.*, D56:2743–2754, 1997.

[49] M. Gockeler, R. Horsley, D. Pleiter, P. E. L. Rakow, and G. Schierholz. A lattice determination of moments of unpolarised nucleon structure functions using improved wilson fermions. 2004.

[50] B. R. Holstein J. F. Donoghue, E. Goldwich. Dynamics of the standard model.

[51] G. Martinelli and Christopher T. Sachrajda. A lattice study of nucleon structure. *Nucl. Phys.*, B316:355, 1989.

[52] Stefano Capitani. Lattice perturbation theory. *Phys. Rept.*, 382:113–302, 2003.

[53] M. Gockeler et al. Lattice operators for moments of the structure functions and their transformation under the hypercubic group. *Phys. Rev.*, D54:5705–5714, 1996.

[54] Yoshio Kikukawa, Rajamani Narayanan, and Herbert Neuberger. Finite size corrections in two dimensional gauge theories and a quantitative chiral test of the overlap. *Phys. Lett.*, B399:105–112, 1997.

[55] Ferenc Niedermayer. Exact chiral symmetry, topological charge and related topics. *Nucl. Phys. Proc. Suppl.*, 73:105–119, 1999.

[56] B. Sheikholeslami and R. Wohlert. Improved continuum limit lattice action for qcd with wilson fermions. *Nucl. Phys.*, B259:572, 1985.

[57] Martin Luscher, Stefan Sint, Rainer Sommer, and Peter Weisz. Chiral symmetry and o(a) improvement in lattice qcd. *Nucl. Phys.*, B478:365–400, 1996.

[58] Oliver Bar, Gautam Rupak, and Noam Shoresh. Chiral perturbation theory at o(a**2) for lattice qcd. *Phys. Rev.*, D70:034508, 2004.

[59] S. Capitani, M. Gockeler, R. Horsley, P. E. L. Rakow, and G. Schierholz. Operator improvement for ginsparg-wilson fermions. *Phys. Lett.*, B468:150–160, 1999.

[60] Yoshio Kikukawa and Atsushi Yamada. Axial vector current of exact chiral symmetry on the lattice. *Nucl. Phys.*, B547:413–423, 1999.

[61] C. Alexandrou, E. Follana, H. Panagopoulos, and E. Vicari. One-loop renormalization of fermionic currents with the overlap-dirac operator. *Nucl. Phys.*, B580:394–406, 2000.

[62] R. Horsley, H. Perlt, P. E. L. Rakow, G. Schierholz, and A. Schiller. One-loop renormalisation of quark bilinears for overlap fermions with improved gauge actions. *Nucl. Phys.*, B693:3–35, 2004.

[63] R. Horsley, H. Perlt, P. E. L. Rakow, G. Schierholz, and A. Schiller. Renormalisation of one-link quark operators for overlap fermions with luescher-weisz gauge action. 2005.

[64] M. Gockeler et al. Perturbative renormalization of lattice bilinear quark operators. *Nucl. Phys.*, B472:309–333, 1996.

[65] Pilar Hernandez, Karl Jansen, and Martin Luscher. Locality properties of neuberger's lattice dirac operator. *Nucl. Phys.*, B552:363–378, 1999.

[66] G. H. Golub and C. F. Van Loan. Matrix computations. *The John Hopkins University Press*, 1996.

[67] R. Sommer. A new way to set the energy scale in lattice gauge theories and its applications to the static force and alpha-s in su(2) yang-mills theory. *Nucl. Phys.*, B411:839–854, 1994.

[68] Christof Gattringer, Roland Hoffmann, and Stefan Schaefer. Setting the scale for the luescher-weisz action. *Phys. Rev.*, D65:094503, 2002.

[69] Y. Namekawa et al. Light hadron spectroscopy in two-flavor qcd with small sea quark masses. *Phys. Rev.*, D70:074503, 2004.

[70] C. Aubin et al. Light hadrons with improved staggered quarks: Approaching the continuum limit. *Phys. Rev.*, D70:094505, 2004.

[71] Jochen Heitger, Rainer Sommer, and Hartmut Wittig. Effective chiral lagrangians and lattice qcd. *Nucl. Phys.*, B588:377–399, 2000.

[72] M. Gockeler et al. Hadron masses and decay constants in quenched qcd. *Nucl. Phys. Proc. Suppl.*, 83:203–205, 2000.

[73] Christof Gattringer et al. Quenched qcd with fixed-point and chirally improved fermions. *Nucl. Phys. Proc. Suppl.*, 119:796–812, 2003.

[74] Y. Aoki et al. Domain wall fermions with improved gauge actions. *Phys. Rev.*, D69:074504, 2004.

[75] Y. Chen et al. Chiral logarithms in quenched qcd. *Phys. Rev.*, D70:034502, 2004.

[76] Michael Booth, George Chiladze, and Adam F. Falk. Quenched chiral perturbation theory for vector mesons. *Phys. Rev.*, D55:3092–3100, 1997.

[77] S. Aoki et al. Light hadron spectrum and quark masses from quenched lattice qcd. *Phys. Rev.*, D67:034503, 2003.

[78] J. A. Gracey. Three loop ms-bar tensor current anomalous dimension in qcd. *Phys. Lett.*, B488:175–181, 2000.

[79] W. Bietenholz et al. Going chiral: Overlap versus twisted mass fermions. *JHEP*, 12:044, 2004.

[80] Mikhail A. Shifman, A. I. Vainshtein, and Valentin I. Zakharov. Qcd and resonance physics: Applications. *Nucl. Phys.*, B147:448–518, 1979.

[81] O. Dumbrajs et al. Compilation of coupling constants and low-energy parameters. 1982 edition. *Nucl. Phys.*, B216:277–335, 1983.

[82] Jiunn-Wei Chen and Martin J. Savage. Matrix elements of twist-2 operators in quenched chiral perturbation theory. *Nucl. Phys.*, A707:452–468, 2002.

[83] Alan D. Martin, R. G. Roberts, W. J. Stirling, and R. S. Thorne. Mrst2001: Partons and alpha(s) from precise deep inelastic scattering and tevatron jet data. *Eur. Phys. J.*, C23:73–87, 2002.

[84] D. Dolgov et al. Moments of nucleon light cone quark distributions calculated in full lattice qcd. *Phys. Rev.*, D66:034506, 2002.

[85] Kostas Orginos, Thomas Blum, and Shigemi Ohta. Nucleon structure functions with domain wall fermions. 2005.

[86] M. Gluck, E. Reya, M. Stratmann, and W. Vogelsang. Next-to-leading order radiative parton model analysis of polarized deep inelastic lepton - nucleon scattering. *Phys. Rev.*, D53:4775–4786, 1996.

[87] W. Detmold, W. Melnitchouk, and Anthony W. Thomas. Connecting structure functions on the lattice with phenomenology. *Int. J. Mod. Phys.*, A18:1343–1350, 2003.

[88] Shoichi Sasaki, Kostas Orginos, Shigemi Ohta, and Tom Blum. Nucleon axial charge from quenched lattice qcd with domain wall fermions. *Phys. Rev.*, D68:054509, 2003.

[89] Andreas S. Kronfeld. Heavy quarks and lattice qcd. *Nucl. Phys. Proc. Suppl.*, 129:46–59, 2004.

[90] Stefano Capitani. Perturbative and non-perturbative lattice calculations for the study of parton distributions. *Nucl. Phys. Proc. Suppl.*, 116:115–120, 2003.

[91] D. Galletly et al. Hadron spectroscopy and light quark masses from overlap fermions. *In preparation.*

[92] D. Galletly et al. *In preparation.*

[93] N.H. Christ M. Clark S.D. Cohen C. Cristian Z. Dong A. Gara B. Joo C. Jung C. Kim L. Levkova X. Liao G. Liu R.D. Mawhinney S. Ohta K. Petrov T. Wettig A. Yamaguchi P.A. Boyle, D. Chen. An overview of the qcdsp and qcdoc computers. *IBM Research Journal*, 2004.